THESIS

CLOUDSAT TROPICAL CYCLONE DATABASE

Submitted by

Natalie D. Tourville

Department of Atmospheric Science

In partial fulfillment of the requirements

For the Degree of Master of Science

Colorado State University

Fort Collins, Colorado

Fall 2010

Master's Committee:

Department Head: Richard Johnson

Advisor: Graeme Stephens

Mark DeMaria
Eric Maloney
Richard Eykholt

ABSTRACT

CLOUDSAT TROPICAL CYCLONE DATABASE

CloudSat (CS), the first 94 GHz spaceborne cloud profiling radar (CPR), launched in 2006 to study the vertical distribution of clouds. Not only are CS observations revealing inner vertical cloud details of water and ice globally but CS overpasses of tropical cyclones (TC's) are providing a new and exciting opportunity to study the vertical structure of these storm systems. CS TC observations are providing first time vertical views of TC's and demonstrate a unique way to observe TC structure remotely from space.

Since December 2009, CS has intersected every globally named TC (within 1000 km of storm center) for a total of 5,278 unique overpasses of tropical systems (disturbance, tropical depression, tropical storm and hurricane/typhoon/cyclone (HTC)). In conjunction with the Naval Research Laboratory (NRL), each CS TC overpass is processed into a data file containing observational data from the afternoon constellation of satellites (A-TRAIN), Navy's Operational Global Atmospheric Prediction System Model (NOGAPS), European Center for Medium range Weather Forecasting (ECMWF) model and best track storm data.

This study will describe the components and statistics of the CS TC database, present case studies of CS TC overpasses with complementary A-TRAIN observations and compare average reflectivity stratifications of TC's across different atmospheric regimes (wind shear, SST, latitude, maximum wind speed and basin). Average reflectivity stratifications reveal that characteristics in each basin vary from year to year and are dependent upon eye overpasses of HTC strength storms and ENSO phase. West Pacific (WPAC) basin storms are generally larger in size (horizontally and vertically) and have greater values of reflectivity at a predefined height than all other basins. Storm structure at higher latitudes expands horizontally. Higher vertical wind shear (≥ 9.5 m/s) reduces cloud top height (CTH) and the intensity of precipitation cores, especially in HTC strength storms. Average zero and ten dBZ height thresholds confirm WPAC storms loft precipitation sized particles higher into the atmosphere than in other basins. Two CS eye overpasses (32 hours apart) of a weakening Typhoon Nida in 2009 reveal the collapse of precipitation cores, warm core anomaly and upper tropospheric ice water content (IWC) under steady moderate shear conditions.

Acknowledgements

Many thanks to colleagues, friends and classmates over the years who have encouraged me to keep going and not give up. First and foremost, I would like to thank my family for love and encouragement along the way, especially my son Paul and dog Dakota.

I would also like to thanks countless others at the office for helping debug code, learn IDL and assist in completing class work. Matt Rogers, John Haynes, Tommy Taylor and everyone past and present who has been a part of the Stephens Research Group and personnel on the department staff.

Thanks to my advisor and committee members; Graeme Stephens, Mark DeMaria, Eric Maloney and Ricard Eykholt for helpful discussions and thorough examination of the contents of this thesis. Thanks to the Department of Atmospheric for admitting me to the master's program and allowing me to continue to work full time while pursuing this degree part time.

TABLE OF CONTENTS

LIST OF FIGURES

LIST OF TABLES

Chapter 1

Introduction

1.1 Tropical Cyclone Monitoring

Tropical cyclone (TC) monitoring via satellites has a long history dating back to the mid-1960's with the introduction of satellite technology. Since that time, almost no TC's have gone undetected ([Parkinson et al., 2006]). Remote sensing of TC's from high altitude began by coincidence in 1954 when an instrumented sounding rocket photographed the Earth with an undocumented tropical storm in the Gulf of Mexico. Earlier observations of TC's were largely based from ship reports and ground observations before the satellite age. Aircraft research flights began in 1956 by the National Hurricane Research Laboratory (NHRL) and provided, at that time, the most comprehensive view of the inner details of TC's ([Anthes, 1982]). Studies by [Shea and Gray, 1973], [Frank, 1977a], [Frank, 1977b], [Frank, 1977c] and [Gray, 1979] compounded years of radiosonde and aircraft reconnaissance to provide a more complete view of the structure of TC's.

The first two decades of satellite technology (1950's and 60's) witnessed a flurry of satellite missions launched into space; e.g. Explorer I and II, TIROS I and ATS 1. The National Aeronautics and Space Administration (NASA) launched the first weather satellite, TIROS I on April 1, 1960. TIROS I collected television (TV) and infrared (IR) photos to aid in detection of weather systems. Subsequent satellite missions (TIROS 1-10, N, M, ATS 1-3, VISSR, SMS, NIMBUS, GOES 1-13, etc.) during the 70's, 80's and 90's, revealed numerous unknown features

of the Earth. Scientists were able to observe developing weather systems, surface temperature variations, sea surface temperatures (SST's), ocean currents and the distribution of water vapor and carbon dioxide in the atmosphere for the first time. It was through these early missions that the continuous monitoring of TC systems by weather satellites began. Using these observations, important features about the lifecycle, structure and track of TCs have been recognized.

The Dvorak technique ([Dvorak, 1975], [Dvorak, 1984]) for estimating the strength of TC's was developed by studying satellite imagery. This method uses cloud patterns from IR and visible satellite imagery to estimate the intensity of tropical systems and is still used by forecasters. Satellite missions during the mid 1990's through the 21st century have focused on instruments containing high-resolution imagery, IR and microwave remote sensing, multispectral scanning, active and passive sensors and constellations of satellites. Observations from the afternoon satellite constellation (A-TRAIN), Tropical Rainfall Measuring Mission (TRMM), Special Sensor Microwave Imager (SSM/I), Advanced Microwave Sounding Unit (AMSU) and the Quik Scatterometer (QuikSCAT) have all contributed to more efficient algorithms and TC prediction products. The CloudSat (CS) mission and A-TRAIN observations are providing, for the first time from satellite, detailed cloud layering, liquid and ice water content (IWC) profiles, bright band signatures, shape and size of convective cores and the presence of precipitation in TC's.

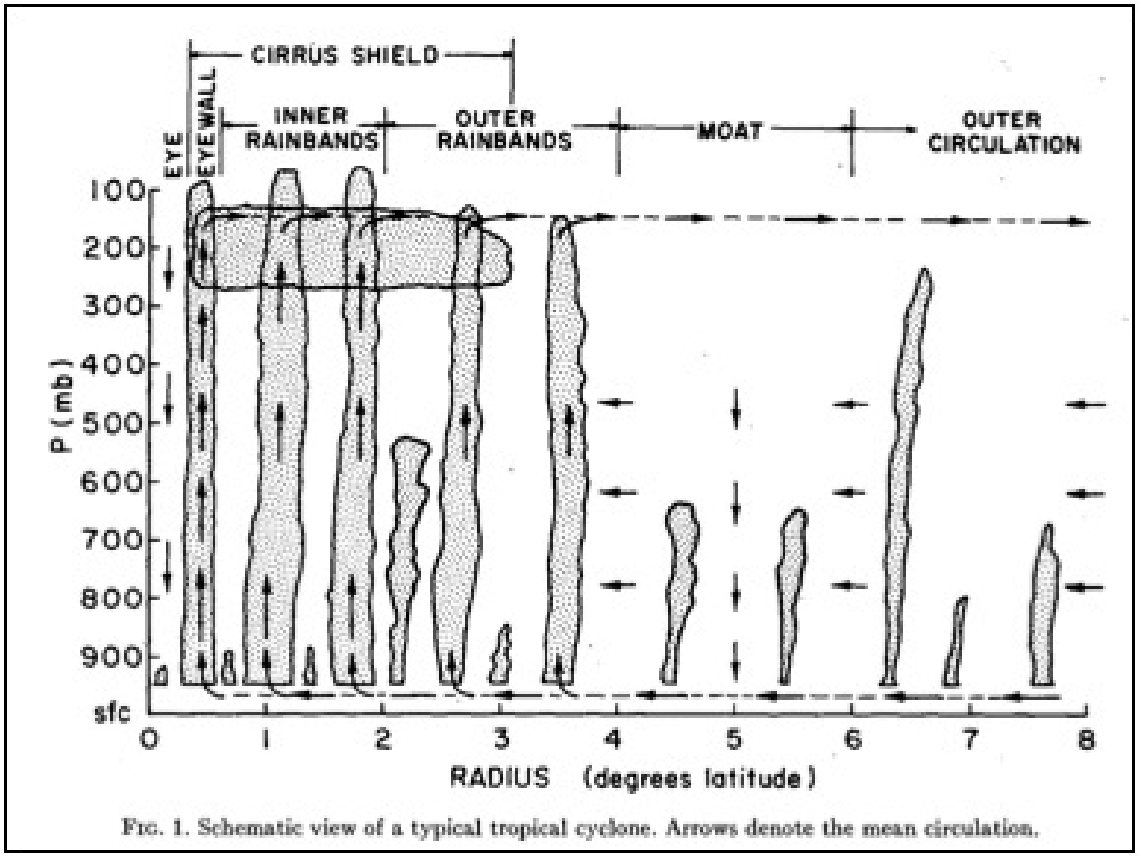

FIG. 1. Schematic view of a typical tropical cyclone. Arrows denote the mean circulation.

FIGURE 1.1: Schematic view of a typical tropical cyclone ([Frank, 1977b])

1.2 Tropical Cyclone Characteristics

A mature HTC (hurricane/typhoon/cyclone) (hurricane in the Atlantic (ATL) and East Pacific (EPAC) basins, typhoon in the West Pacific (WPAC) and cyclone in the Southern Hemisphere (SHEM) and Indian Oceans (IO)) can approach wind speeds of 100 m/s within the eyewall region and contain wind fields extending over 1000 km from the storm center ([Frank, 1977b]). A TC is defined as a warm core vertical circulation, with cyclonic winds in the lower levels and anticyclonic winds in the upper troposphere (Figures 1.1 and 1.2). TC's generally form over warm ocean waters (at least 26.5° C (80 °F)) near a pre-existing near-surface disturbance with sufficient vorticity and convergence ([Gray, 1968], [Gray, 1979]). The atmospheric environment must cool rapidly enough with height such that it is unstable to moist convection, contain relatively moist layers in the mid-troposphere and contain low values of vertical wind shear (magnitude of wind

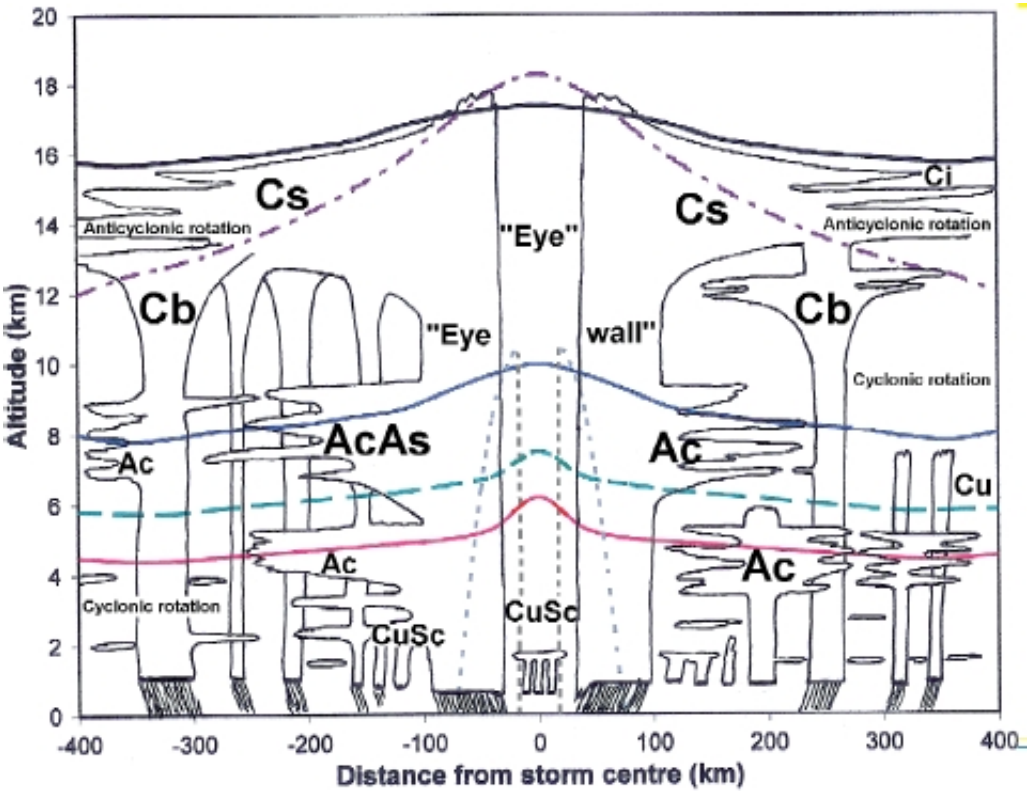

FIGURE 1.2: Cross-section of a mature tropical cyclone. Freezing level (red line), 500hPa (green dashed line), -20°C isotherm (blue line), tropopause height (black line), the division of cyclonic/anticyclonic flow (light purple dot-dash line) and winds greater than 17 m/s (light gray dashed line). Cloud types: Cb (cumulonimbus), Cu (cumulus), Ci (cirrus), Sc (stratocumulus), Ac (Altocumulus), As (Altostratus) and Cs (cirrostratus). (Source: [Galvin, 2008], Figure 2.)

change with height) between the surface and upper troposphere. The release of latent heat (water vapor condensing into liquid water) drives the overall system of TC development. TC's are idealized as a Carnot engine, converting heat energy from the ocean into mechanical energy ([Emanuel, 1986]).

A typical mature TC contains a core of intense winds and precipitation extending 5-50 km outward from the outer radius of the eye ([Anthes, 1982]). The eye contains warm, descending air and calm winds with little or no convection, surrounded by an eyewall cloud 10-20 km wide containing strong cyclonic flow in the lower troposphere, intense convection and heavy precipitation. Outside of the eyewall, winds diminish with radial distance from the storm center and convection is confined to curving squall lines (spiral or feeder rain bands). Outward of the inner and outer rain bands, clear or moat areas with limited convection may exist. A dense cirrus

shield covers the inner radius of the storm system for a distance equivalent to 0-4° of latitude. Figure 1.1 depicts a schematic vertical schematic view of a TC as presented by [Frank, 1977b]. Figure 1.2 presents a detailed inner view of the cloud layering and flow patterns of a general mature TC system ([Galvin, 2008]).

TC's typically experience four different stages of development spanning on average nine days but can be as short as two or last more than twenty days. Stages can occur more than once during a lifecycle. The four stages of development are formation (genesis), intensification (deepening), full maturity and finally the decay stage.

A TC begins as a cumulus cluster in a low level cyclonic disturbance (formation stage). The cluster starts to develop a surface circulation and transforms from a cold core system (strongest winds towards the tropopause) to a warm core (strongest winds towards the surface). During the intensification (deepening) stage, the storms central pressure decreases and maximum wind speed increases. The cluster starts to develop organized deep convection and an eye may start to form. Upper tropospheric outflow develops and the tangential winds are in near dynamic and thermodynamical equilibrium. As the storm reaches the maturity stage, the TC reaches maximum intensity, storm central pressure is at a minimum and winds speeds are at a maximum. The storm is typically symmetric about the center. The final stage, decay, occurs when the central pressure starts to increase, maximum wind speeds decrease and the storm becomes axisymmetric. This occurs as a result of different factors, cold SST's, landfall or extratropical transition (ET). Examples in Chapter 3 will explore these life cycles with example imagery from CS and complementary satellite observations.

1.3 Microwave Satellite Sensors

Remote Sensing is a technique for sampling electromagnetic radiation from the Earth and using this data to interpret features about the Earth's surface, oceans and atmosphere. Earth observing satellites (EOS) carry sensors capable of recording wavelengths of visible, IR and microwave radiation across the electromagnetic spectrum.

There are two types of remote sending techniques to collect data about the Earth, active and passive remote sensing. Passive satellite sensors measure naturally occurring radiation emitted or reflected from the earth. They use small amounts of power (compared to active sensors) resulting in longer lifetimes for these sensors, an important benefit for space satellite missions where refueling or recharging satellites is typically not an option. NASA's AMSR-E and Moderate Resolution Imaging Spectroradiometer (MODIS) instruments aboard the satellite Aqua are examples of passive sensors. Active satellite sensors, on the other hand, send and receive pulses of energy to and from the Earth's surface. By projecting a known wavelength and frequency radiation beam to the Earth, measurements can be made on how long it takes the beam to reflect back and the amount of scattering the beam incurs. Larger amounts of scattering occur when the beam targets larger sized water or ice particles. The scattered return power signal received by the radar is converted into a quantity known as reflectivity by using knowledge about the characteristics of the radar and properties of water (or ice). The magnitude of the reflectivity is related to the size and concentration of droplets encountered by the radar beam. The CS cloud profiling radar (CPR) is so sensitive to the presence of water droplets and ice that the radar can detect very small particles which form clouds. The Tropical Rainfall Measuring Mission (TRMM) precipitation radar (PR) and the CS CPR are examples of active satellites.

Observations of clouds at microwave frequencies (GHz) provide a useful approach for measuring the scattering and emission properties of precipitation (ice and water) particles. Microwave frequency radiation channels allow sensors to penetrate clouds and see through to the surface.

Microwave radiation is also sensitive to a variety of atmospheric parameters (temperature, moisture, cloud water/ice and precipitation). The first microwave satellite sensor was launched into space in 1987. The Defense Meteorological Satellite Program Special Sensor Microwave Imager (DMSP SSM/I) consists of seven separate radiometers measuring microwave emission from the earth. Subsequent satellite missions have introduced additional microwave frequencies, finer resolutions and larger swath areas.

Satellite observations and imagery have steadily improved over the years with more advanced equipment available for TC monitoring and has vastly improved the quality of TC monitoring ([Rappaport et al., 2009]). Early TC satellite observations relied upon IR and visible imagery from geostationary satellites to estimate storm position and intensity ([Dvorak, 1984]). Subsequent satellite missions improved observations by adding passive microwave sensors (DMSP SSM/I) with the ability to penetrate cirrus clouds and reveal low level TC structures, estimating wind, pressure and precipitation ([Rodgers and Adler, 1981], [Kidder et al., 1978] and [Velden and Smith, 1983]). Additional microwave sensors with more frequency channels (TRMM Microwave Imager (TMI), AMSR-E, AMSU, MODIS, SSM/I) over the 1990's and 2000's have yielded more accurate forecasts and provided a new suite of products and services (Kidder et al. 2001, Lee et al. 2002). One of the best sites for viewing near real-time TC imagery is from the Naval Research Laboratory's (NRL) website ([Hawkins et al., 2001]).

Passive microwave imagery uses various frequencies to observe upwelling radiation. For example, radiances from the 85-91 GHz microwave channel are used to to quantify cloud liquid and ice concentrations. At this frequency, deep convection appears cold while clouds and moist air masses have warm brightness temperatures over the ocean. The imagery can also detect internal storm structure features and ice conditions in the storms upper levels. At the 37 GHz frequency, clouds containing water and/or ice emit warm brightness temperatures (against the cooler ocean surface) and reveal low-level cloud features missed at the 85-91 GHz frequency. Upwelling radiation at 37 GHz is largely unaffected by ice particles and is mostly sensitive only to liquid droplet variations.

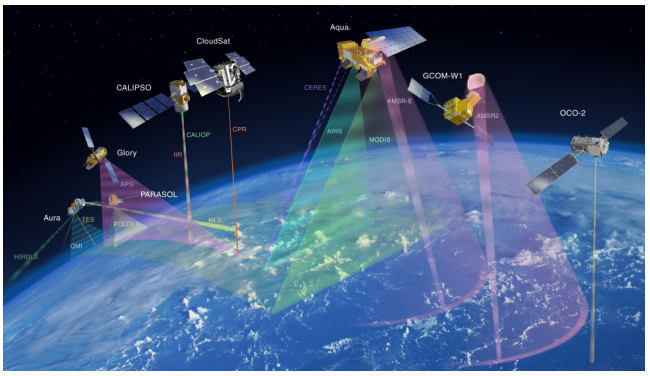

FIGURE 1.3: A-Train satellite constellation

Other examples of microwave instruments include the AMSU-A and AMSU-B instruments aboard the National Oceanic and Atmospheric Administration (NOAA) operational polar orbiting satellites. AMSU-A provides temperature soundings and is also used to derive cloud liquid water and rain rates at 48 km horizontal resolution. AMSU-B provides moisture soundings at 16 km horizontal resolution. The AMSU instruments are used frequently in TC analysis applications for deriving wind and rain rates ([Kidder et al., 2000]). Microwave observations of SST's using the TRMM TMI satellite sensor have also improved measurements by its ability to penetrate clouds and observe the ocean surface whereas previous IR observations had limited coverage due to cloud shielding ([Dommenget and Stammer, 2004], [Reynolds et al., 2004]). The NASA QuikSCAT measured ocean surface vector wind retrievals using an active Ku-band (13.4 GHz) microwave sensor ([Hoffman and Leidner, 2005]) aiding in TC wind retrievals but measurements can become contaminated by heavy precipitation. WindSat ([Gaiser et al., 2004]) contains a microwave radiometer scanning at five channels (6.8, 10.7, 18.7, 23.8, 37.0 GHz) and provides observations of 10 m wind speed, SST, total precipitable water, integrated cloud liquid water and rain rates over ocean areas. These are just a few examples of how advancements in microwave satellite technology are providing powerful tools for observing TC's.

1.4 A-Train Satellites

The constellation of the A-TRAIN in Figure 1.3 consists of 5 satellites: Aura, Parasol, Calipso, CS and Aqua. These satellites provide active and passive atmospheric measurements at IR and microwave wavelengths. Data from Aqua and CS are used to construct the CS TC database. Aqua, launched May 4, 2002, is the first satellite in the A-TRAIN constellation and flies approximately 1 minute ahead of CS in the A-TRAIN formation. Aqua contains six different instruments, data from two of which are used in the CS TC database. The Orbiting Carbon Observatory (OCO) Mission failed to launch on February 24, 2009 and a future mission is planned for no later than February 2013.

The first instrument from Aqua, AMSR-E, contains a 12-channel, six frequency passive microwave radiometer. AMSR-E is designed to monitor a broad range of hydrologic variables ([Kawanishi et al., 2003]) related to the Earth's water cycle. Spatial resolution varies from 5.4 km to 56 km depending upon the frequency. Over the ocean, AMSR-E microwave frequencies measure rain rates, SST's and ocean roughness (converted into near-surface wind speeds).

The second instrument from Aqua, MODIS, is designed to measure biological and physical processes globally with approximately 40 data products produced daily. MODIS provides imagery in 36 bands (16 thermal emissive bands and 20 reflected solar bands) between 0.4 and 14.5 μm at resolutions of 250 m to 1000 m ([Qu et al., 2006]). MODIS measures a variety of large-scale global atmospheric dynamics and features: cloud top pressure (CTP), cloud top temperature (CTT), optical thickness, cloud phase, water vapor profiles and changes in cloud cover.

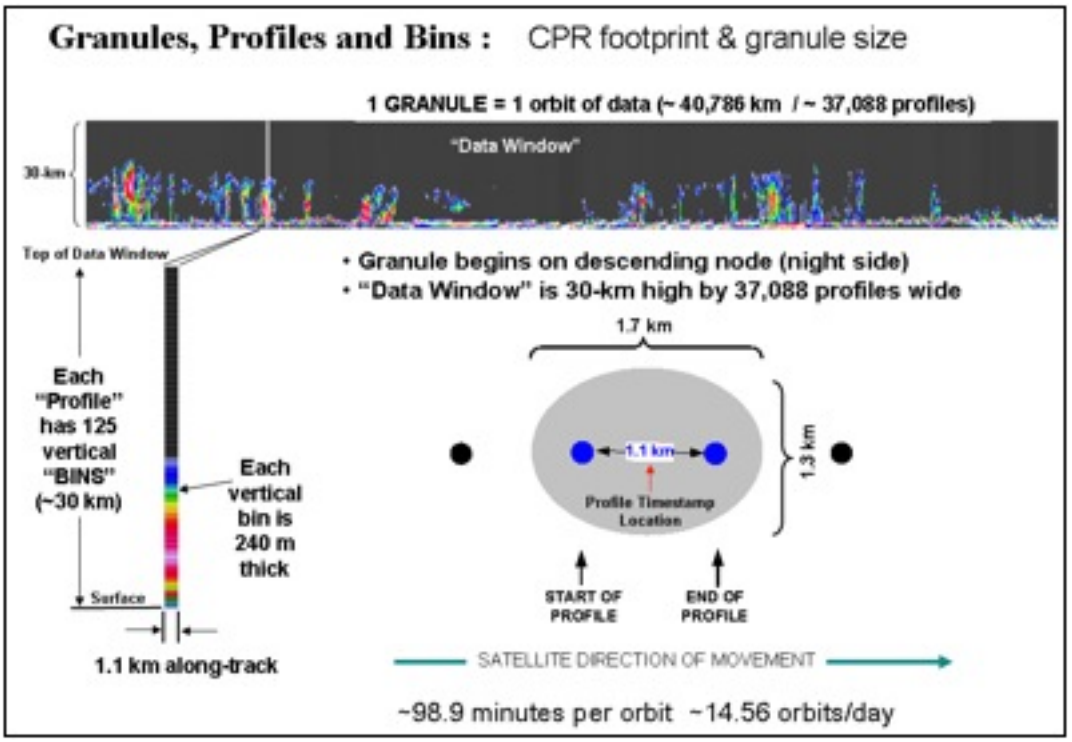

FIGURE 1.4: CloudSat data footprint and granule and size

A key advantage to the A-TRAIN constellation are the near simultaneous views of the same footprint (in different resolutions and path size) within minutes of each other making AMSR-E and MODIS measurements easily extracted alongside each CS overpass. Multiple instruments at various frequencies within minutes of each other all viewing the same area provide an exceptional qualitative view of atmospheric conditions and an opportunity to compare measurement by these instruments.

1.5 CloudSat

CS is one of a series of sensors dedicated to improving the understanding of clouds and precipitation from space and the feedback of clouds in the climate system ([Stephens et al., 2002]). The CS mission was selected by the NASA Earth System Science Pathfinder (ESSP) program to study how radiant energy is distributed throughout the atmosphere and to observe cloud condensate and precipitation. CS is the first satellite to carry a W-band (94 GHz), 3 mm nadir

pointing CPR. CS orbits at 705 km as part of the A-TRAIN constellation of satellites (see Figure 1.3) and has the ability to observe vertical cross sections of clouds and precipitation providing a wealth of information about their internal structures in detail and spatial coverage never before seen. CS launched on April 28, 2006 and started data collection on June 2, 2006. The satellite flies in a sun synchronous polar orbit that repeats its ground track every 16 days. The CS CPR operates at a frequency of 94 GHz and has a minimum detectable reflectivity of -29 dBZ ([Stephens et al., 2008]) (Figure 1.4).

The CS CPR is highly sensitive to the presence of hydrometeors in the atmosphere. Such high frequency radars are not only sensitive to the observation of clouds but can also detect the presence of both solid and liquid precipitation. The return signal of the radar is a function of cloud particle number concentration, size, temperature and phase (ice/water). With proper constraints and assumptions, basic microphysical properties from radar reflectivity measurements can be inferred ([Marchand et al., 2008]). To compute the range-resolved radar cross section per unit volume, η, at a specified range r is:

$$\eta = \frac{P_{rec}(4\pi)^3 r^2 L_a}{P_t \lambda^2 G_{rec} G^2 \Omega \Delta} \tag{1.1}$$

where P_{rec} is the output power of the receiver, r is the range to the atmospheric target, L_a is the two-way atmospheric loss, P_t is the transmitted power, λ is the wavelength, G_{rec} is the receiver gain, G is the antenna gain, Ω is the integral of the normalized two-way antenna pattern and Δ is the integral of the received waveform shape. The value, η, is then converted into radar reflectivity, Z_e where $|K_w|$ is 0.75 (for water in the W band @ 10° C).

$$Z_e = \eta \frac{\lambda^4 10^{18}}{\pi^5 |K_w|^2} \tag{1.2}$$

One vertical profile of η is sampled every 0.16 seconds corresponding to the motion underneath the satellite of 1.09 km ($\pm$ 10 m depending on latitude). The CPR samples 125 bins per profile every 240 m resulting in a 30 km atmospheric vertical height.

The calculated reflectivity, Z_e, increases with increasing frequency but becomes prohibitive at higher frequencies due to attenuation of the radar signal. The 94 GHz frequency in which the CS radar operates, the effects of attenuation may be significant in area of deep convection and heavy rain typically found in TC's. Studies by [Haynes et al., 2009], [Haynes and Stephens, 2007] and [Stephens and Wood, 2007] utilize the principle that attenuation can be used as a source of information rather than noise. Using path-integrated attenuation (PIA) and reflectivity, the vertical gradient of reflectivity at any height is thus related to the magnitude of the attenuation at that height. From this, CS rain rates can be derived ([Matrosov et al., 2008]).

The CS radar is the most sensitive cloud radar launched to date with advantages over previous TC microwave observations. At the expense of horizontal resolution, the vertical resolution of CS provides new details regarding cloud layers, distribution of vertical water vapor and areas of precipitation. With a low ($\sim$29 dBZ) minimum reflectivity, CS is able to detect thin cirrus clouds and ice particles in the upper troposphere.

Validations efforts of the CS CPR have been performed (CCVEX-CALIPSO-CloudSat Validation Experiment) since launch ([Protat et al., 2009]). Analysis shows the reflectivity agrees to within 1 dBZ except in the areas of heavy precipitation where multiple scattering becomes an issue. Care must be used when comparing CS observations with other instruments. CS observations can be affected by attenuation of supercooled liquid water, large ice particles and multiple scattering by the CPR. Supercooled water is typically found in deep convection systems (e.g. TC systems) and forms when vigorous updrafts push liquid water droplets above the melting layer. [Protat et al., 2009] suggest CS ice profiles are valid for use down to around the nine km in vertical height level (or four km above the melting layer) due to the attenuation of supercooled liquid droplets below this level. Multiple scattering occurs when liquid droplets larger than 3 mm are detected by the radar typically found below the melting layer.

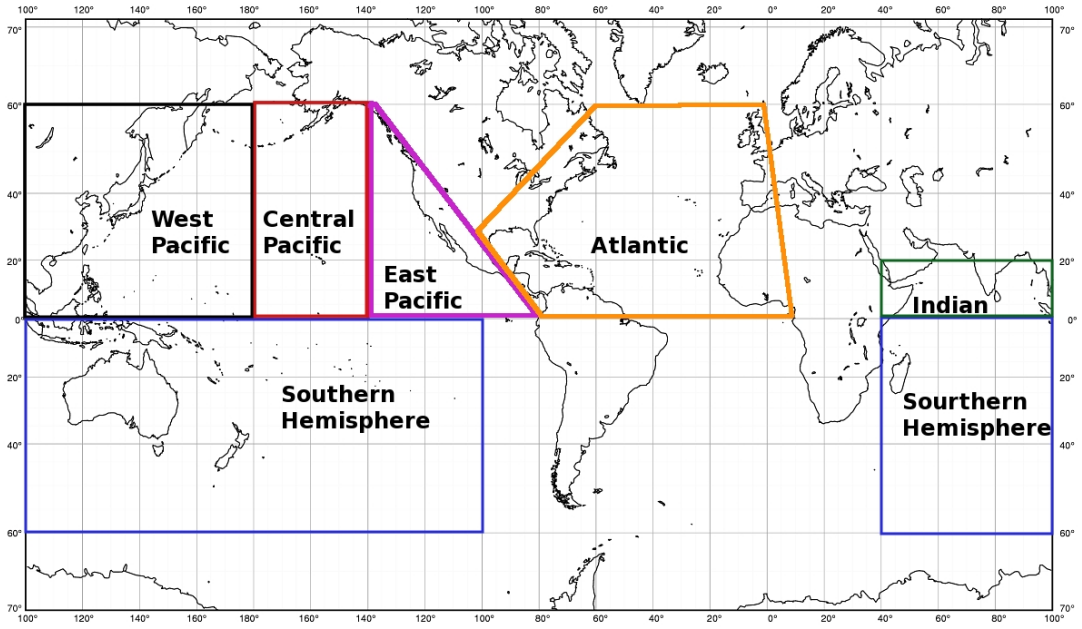

FIGURE 1.5: NRL basin designations

1.6 Naval Research Laboratory

The Satellite Meteorological Applications Section at the Naval Research Laboratory (NRL) is responsible for ingesting and distributing data from over 33 satellite sensors on a daily basis for monitoring worldwide weather events ([Mitrescu et al., 2008], [Hawkins et al., 2001]). The NRL automated processing system provides a comprehensive and diverse source of satellite and model data not only for the Navy but also for the users of the research and development community. The NRL TC web page (http://www.nrlmry.navy.mil/tc_pages/tc_home.html) contains satellite products in and around TCs using multi-sensor microwave, visible, IR and water vapor imagery. The site provides an online suite of data available for real time and archive studies of global TCs. Shortly after CS was launched in 2006, NRL reached a special agreement with the Cooperative Institute for Research in the Atmosphere (CIRA) CS Data Processing Center (DPC) to download the CS level 1 data product, 1B-CPR-FL within a few minutes after the raw (level 0) data is received at the CIRA DPC. The availability of this data provides quick look images of CS overpasses generated typically within four to six hours of the event.

The Automated Tropical Cyclone Forecast (ATCF), developed for the Joint Typhoon Warning Center (JTWC), is a software package used to plot and generate TC forecasts and information [Miller et al., 1990]. The software assigns distinct alpanumeric codes for each TC as it develops and is unique to each TC in each of the six different basins (ATL, WPAC, EPAC, IO, CPAC and SHEM). The ATCF basin areas are shown in Figure 1.5. NRL has adopted the same basin designation for following and distributing TC information and this same basin scheme is used throughout this paper. Of note in the basin areas is the large area encompassing the SHEM and the small area of the IO basin region.

1.7 Research Goals

The goals of this research presented herein focuses on the description and creation of the CS TC database, compositing reflectivity profiles across different atmospheric regimes (SST, shear, basin, year and strength) and comparing CS observations with other passive and active satellite sensors (AMSR-E, MODIS). The significance of the zero and ten dBZ reflectivity thresholds will be examined across different basins, SST and latitude regimes. Average height values of the zero and ten dBZ thresholds (useful for tracing precipitation sized particles) will also be explored and discussed. The thesis concludes with a summary of the CS TC database findings drawn from its analysis and proposed future work. The analysis describes features of CS TC overpasses from June 2, 2006 through December 6, 2009 unless otherwise stated.

Chapter 2

Data Processing and Format

2.1 CloudSat Data Processing Center

The CS DPC is responsible for ingesting level 0 CS data and preparing the corresponding Level 1 and 2 data products. The CS data variables used to create portions of the TC database contain data from the CS DPC level 2 products 2B-GEOPROF, MOD06-5KM, 2B-PRECIP-COLUMN, 2B-CWC-RO and 2B-CLDCLASS. The CS DPC (http://cloudat.cira.colostate.edu) documentation fully details the algorithms, variable definitions and product descriptions. The following provides a brief description of the products and associated variables used in the CS TC database.

The 2B-GEOPROF product identifies levels in the vertical column sampled by the CPR containing radar echo information from hydrometeors and in turn provides an estimate of the radar reflectivity. From the 2B-GEOPROF data product, height, cloud mask and radar reflectivity (dBZ) are extracted for each TC overpass. Cloud mask contains information identifying where hydrometeors occur in the profile over the instrument noise floor which in turn helps identify cloud layers and tops in the profile. Radar reflectivity is the return echo power as a function of cloud height (at 125 levels).

The MOD06-5KM CS product contains a subset of ancillary MODIS radiances and cloud mask data that overlaps and surrounds each CS CPR footprint. Variables extracted from the MOD06-5KM data product include 11 μm BT, CTT, pressure and height.

2C-PRECIP-COLUMN CS product determines the presence of surface precipitation and quantifies the intensity based on CPR observations. Precipitation properties, cloud layer heights, freezing level, frozen precipitation height and corresponding AMSR-E and ECMWF observations are extracted from this data source.

2B-CWC-RO CS product contains estimates of cloud liquid, IWC and other associated properties for each radar profile. From this data product, radar only retrieved values of IWC and ice water path (IWP) are extracted.

2B-CLDCLASS CS product determines cloud type in eight different groups, stratus (ST), stratocumulus (SC), cumulus (CU), nimbostratus (NS), altocumulus (AC), altostratus (AS), deep convective clouds, or high clouds. High cloud types include cirrus (CI), cirrocumulus, and cirrostratus, and the CU cloud class represents cumulus congestus and fair weather cumulus.

2.2 Naval Research Laboratory Data Processing

Processing the data to form the CS TC database is a two-fold process. Portions of the dataset are assimilated by NRL and rest of the dataset is then processed and distributed at Colorado State University (CSU).

In the case of a weather event such as a TC, NRL defines a sector around the disturbance which tracks the system and retrieves satellite imagery for these sectors as polar-orbiting satellite systems or geostationary satellites come into contact with the sector area. CS orbits the earth approximately 16 times per day and as CS intersects a predefined sector, the overpass is superimposed atop satellite imagery (geostationary or polar-orbiting based) and the corresponding 1B-CPR-FL radar reflectivity's are plotted (see Chapter 3 for example NRL and CS imagery)

and overlaid with Navy Operational Global Atmospheric Prediction System (NOGAPS) data (version 4.0). NOGAPS is a global, spectral forecast model with a resolution of 0.5° (∼54 km). NOGAPS data provides useful thermodynamical fields to determine temperature, melting layer and precipitation structures ([Mitrescu et al., 2008]). The data contains an estimate of height, temperature and dewpoint at 17 pressure levels as well as SST's, surface winds and temperature. In environments surrounding the inner core of a tropical system, NOGAPS temperature, dewpoint and height levels will not always be 100% accurate since the global model only contains 0.5° grid resolution and dependent upon model physics. The imagery produced by NRL of the CS overlay and matching satellite imagery provides a unique 3-D vertical cross section view of the storm atop a 2-D satellite image.

Along with the graphical imagery produced by NRL using the 1B-CPR-FL data, NRL also creates a corresponding hierarchical data format (HDF) data file containing the CS profile intersection time through the sector, storm information (preliminary storm center latitude, longitude, maximum winds and pressure), model data (NOGAPS) and A-TRAIN sensor data from the satellite Aqua (AMSR-E data) (See Table 2.2 for a complete description). The HDF file format is stamped according to the CS filename convention and the designated TC name/number (provided by the National Hurricane Center (NHC) or JTWC). The naming scheme of each file is given in Table 2.1 and basin designations are described in Figure 1.5. The file is then ftp transferred over to CSU typically within ten days of the initial CS overpass.

Once each data file is received from NRL, the profile time of the CS overpass is matched with the corresponding CS data products (2B-GEOPROF, MOD06-5KM, 2C-PRECIP-COLUMN, 2B-CWC-RO and 2B-CLDCLASS) and the variables are extracted from each file. Table 2.2 describes each data parameter included in each storm overpass. At a minimum, each TC storm file will contain 2B-GEOPROF data. When the file is initially created, storm specific data (latitude, longitude, pressure and winds) will only contain preliminary storm information from NRL. SST and shear values are added once the official best track data is released (at the end of the TC season).

2.3 Best Track

In February of each year, best track storm data (Mark DeMaria, personal communication) is added and updated into the final data product. Best track storm center latitude, longitude, maximum wind speed, minimum pressure are updated (if available) for each TC overpass as a replacement to the initial storm information provided by NRL. Best track data consists of positions and intensities for each reported global TC every six hours. Linear interpolation is used to estimate storm position and intensity outside of these time periods. Updates to the content of the CS TC files are made available on the CS TC website.

2.4 Wind Shear and Sea Surface Temperature

Vertical wind shear, the difference of wind speed from 200-850 mb, are used from the Statistical Hurricane Intensity Prediction Scheme (SHIPS) ([DeMaria and Kaplan, 1999]). The SHIPS model is statistical-dynamical intensity prediction model developed using standard multiple regression techniques. SST's are added to each TC overpass from the Reynold's SST global analysis ([Reynolds and Smith, 1995]).

TABLE 2.1: Tropical cyclone file naming structure

YYYYDDDHHMMSS_NNNNN_CS_TC-BASIN-NUM NAME_GRANULE.hdf	
YYYY	year
DDD	julian day
HH	hour
MM	minute
SS	second (UTC)
NNNNN	granule number
CS	CloudSat
TC	Tropical cyclone data product
BASIN	ocean basin
NUM	storm Number
NAME	storm Name
GRANULE	data subset designation

2.5 Final Data Production

The final data product contains storm specific variables of the overpass, CS radar reflectivity's at 125 height levels, numerical weather prediction (NWP) model data (NOGAPS) and corresponding A-TRAIN satellite data (MODIS and AMSR-E). The product contains the naming convention shown in Table 2.1, following the format set forth by the CS DPC. The end user can easily distinguish the name, basin, date and time at which the overpass occurred. A list of all variables and descriptions for each overpass is shown in Table 2.2.

TABLE 2.2: CloudSat Tropical Cyclone database variables

Variable Name	Units	Description
Storm Specific Variables		
Storm Center Longitude	degrees	longitude at storm center
Storm Center Latitude	degrees	latitude at storm center
Storm MSLP	mb	minimum storm pressure
Storm Max Wind	m/s	maximum storm winds
Storm Shear	knots	200 850 mb shear (SHIPS)
Storm SST	C	storm center SST temperature
CS 2B-GEOPROF		
Profile Time	UTC (hr)	CloudSat overpass times
Latitude	degrees	latitude
Longitude	degrees	longitude
LandSeaFlag	–	specifies land or sea overpass
Height	m	vertical height bins
Cloud Mask	–	cloud detection
Surface Height Bin	–	bin at which the surface starts
Gaseous Attenuation	dBZ	Gaseous attenuation

Continued on Next Page...

Table 2.2 – Continued

Variable Name	Units	Description
Reflectivity	dBZ	CPR reflectivity
CS MODIS		
Cloud Top Temperature	K	Cloud top temperature
Cloud Top Pressure	hPa	Cloud top pressure
Cloud Top Height	m	Cloud top height
Brightness Temperature	K	11 μm temperature
NOGAPS		
Pressure Levels	mb	17 levels
Temperature	K	Temp @ 17 pressure levels
Height Levels	km	Height @ 17 pressure levels
Dewpoint	K	Dewpoint @ 17 pressure levels
Usfc	m/s	Surface wind speed
Vsfc	m/s	Surface wind speed
Tairsfc	K	Temperature of surface
SST	K	NOGAPS SST's
AMSR-E		
89 H Brightness Temperature	K	Temperature @ 89 H
SST	K	AMSR-E sea surface temps
Wind	m/s	surface wind speed
Water Vapor	kg/m2	Water vapor
LWP	kg/m2	liquid water precipitation
Rain rates	mm/h	Surface rain rates
CS 2C-PRECIP-COLUMN		
Precipitation Rate	mm/h	Precipitation Rate
Precipitation Flag	–	How likely precipitation is occurring
Phase Flag	–	Estimate of the phase of precipitation
Cloud Top Lowest Layer	km	Height of lowest cloud layer
Cloud Top Highest Layer	km	Height of highest cloud layer
Frozen Precipitation Height	km	Height of frozen precipitation
Melted Fraction	–	Mass fraction of liquid in precipitation
Freezing Level	km	Height of freezing level (ECMWF)
SST	C	ECMWF SST
Surface wind	m/s	ECMWF surface wind speed
CWV AMSR-E	mm	Derived column water vapor
LWP AMSR-E	mm	Derived cloud liquid water
SST AMSR-E	C	AMSR-E SST (nearest pixel)
Precipitation AMSR-E	mm/h	AMSR-E precipitation rate
AMSR-E dist	km	Distance to nearest AMSR-E pixel
CS 2B-CWC		
Ice Water Content	mg/m3	Radar only ice water content
Ice Water Path	g/m2	Radar only ice water path
Ice Effective Radius	μm	Radar-only Ice Effective Radius
Ice Number Concentration	1/L	Radar-only Ice Number Concentration
Ice Distribution Width Parameter	–	Radar-only Ice Distribution Width Parameter
CS 2B-CLDCLASS		
Cloud Scenario	–	Cloud Type

2.6 Website

Once the final data products are completed, the data is made available for public use and download (http://cloudsat.cira.colostate.edu). The data can be downloaded in yearly compressed tar files or individual storm overpasses. Each data file is filed according to year, basin, storm number and name similar to NRL TC product storage. Along with each HDF file, the corresponding NRL produced imagery (visible, IR and AMSR-E) are copied over from the NRL website. The NRL imagery complements and provides a visual representation of the CS overpass, providing the end user an easy way to distinguish where CS intersected in relation to the storm.

Chapter 3

A Tropical Cyclone Database and Selected Case Studies

3.1 Statistics

The TC CS database contains three and a half years of data (June 2, 2006 through December 6, 2009). Table 3.1 summarizes storm characteristics (number of overpasses per basin, season averages of SST and shear, type of overpass (TD, TS, HTC) and the number of overpasses relative to the storm center). Seasons are designated yearly except for the SHEM which overlaps onto two years and is defined from July to June. For example, the 2006 season extends from July 2005 through June 2006. Figure 3.2 graphically represents the data distribution. Table 3.2 summarizes the average and standard deviation of the TC CS data points for shear, SST, wind, minimum radial distance, latitude and basin for each season.

The radial distribution of all the data points is shown in Figure 3.1. Since launch, CS has collected over 7.2 million TC overpass points. Over 144,000 of these points have collected data within the first 50 km of the storm center and approximately 142 have intersected eye walls of TC's assuming an average eye diameter of 30 km. To estimate the probability CS will overpass the eye of a TC of 30 km width, the total number of overpasses to date is compared to the

TABLE 3.1: Detailed CloudSat tropical cyclone overpass data by year and basin. A disturbance is defined as maximum winds less than 10.3 m/s. TD denotes tropical depression, TS denotes tropical storm and HTC denotes hurricane/typhoon/cyclone.

Basin	Year	Disturbance	TD	TS	HTC	30	50	100	200	500	ALL
ATL	2006	0	60	53	35	5	13	21	34	72	149
ATL	2007	0	148	69	21	5	8	22	40	109	238
ATL	2008	0	174	131	58	14	18	38	72	169	363
ATL	2009	0	96	41	19	4	5	8	21	80	156
WPAC	2006	135	98	93	89	11	17	38	73	193	415
WPAC	2007	113	118	81	82	12	23	43	82	188	394
WPAC	2008	107	107	101	58	15	22	29	75	187	373
WPAC	2009	139	119	110	78	17	20	40	94	219	446
EPAC	2006	1	176	59	48	16	20	32	59	145	284
EPAC	2007	1	152	45	11	5	12	16	26	108	209
EPAC	2008	5	177	75	30	7	14	27	53	119	287
EPAC	2009	2	145	64	25	7	14	22	42	121	236
SHEM	2006	23	48	24	17	1	3	7	14	21	112
SHEM	2007	87	124	133	57	11	20	43	89	196	401
SHEM	2008	100	163	135	67	12	20	47	79	212	465
SHEM	2009	84	141	75	30	9	10	33	67	170	330
IO	2006	7	4	12	0	1	1	1	5	11	23
IO	2007	21	37	24	11	2	4	7	13	47	93
IO	2008	46	33	25	6	2	3	11	22	54	110
IO	2009	26	9	25	0	2	2	7	7	25	60

number of eye overpasses that have occurred. When CS intersects a TC, then this counts as one 'hit' of a granule. CS has made 5,278 storm overpasses resulting in 1283 days of CS data (through December 6, 2009). With 14.5 orbits per day, 31 sections per orbit and 1,253 days of data results in a total of 576,709 granules of data. A granule is defined as a 1200 km long section of an overpass. Of the 5,278 overpasses, 142 CS overpasses intersected storms within 30 km of storm center. Using these numbers, the probability of CS intersecting a TC center is 0.025% or roughly every 1 in 4000 CS TC intersections. Table 3.3 lists the top 40 CS overpasses of HTC strength. The WPAC regions dominates in inner storm area overpasses, 20 out of the top 37 overpasses occurred in that basin with no overpasses in the IO.

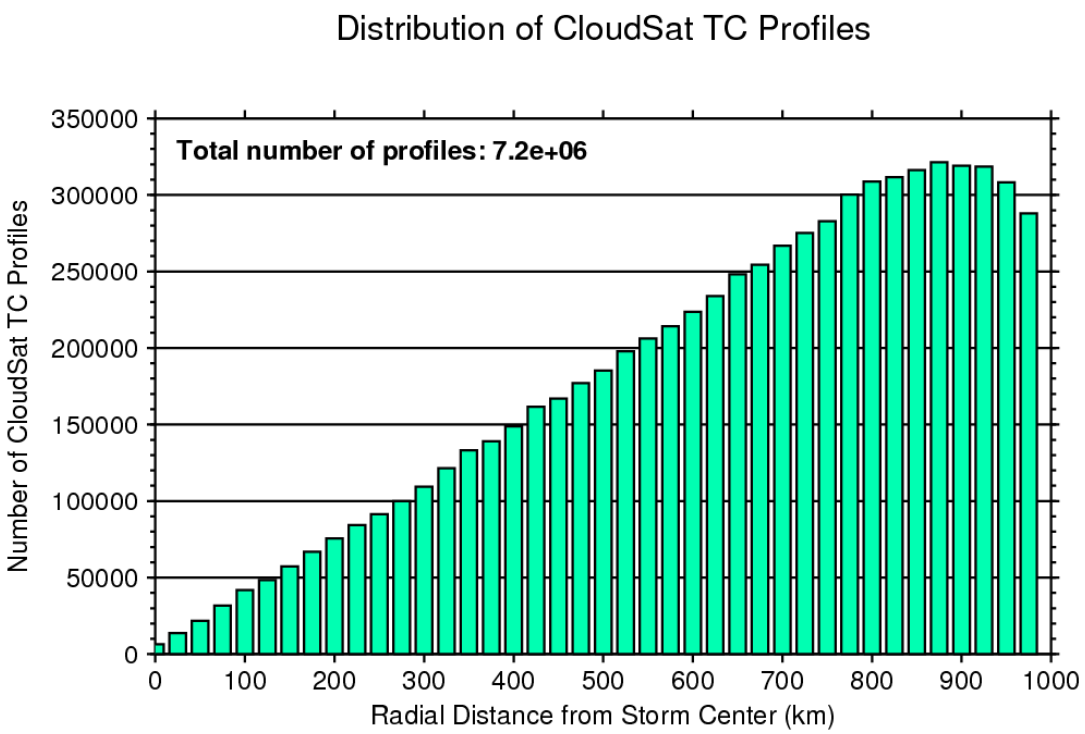

FIGURE 3.1: Number of CloudSat Tropical Cyclone points by radial distance as of December 6, 2009.

3.2 Example Overpasses

The following examples explore CS observations of TCs during the four typical stages of development: formation (genesis), intensification (deepening), maturity and decay. Each case provides graphical analysis of CS data with complementary sensor measurements. Table 3.4 details storm categories of TC's based on wind criteria for the ATL, EPAC, CPAC and WPAC basins.

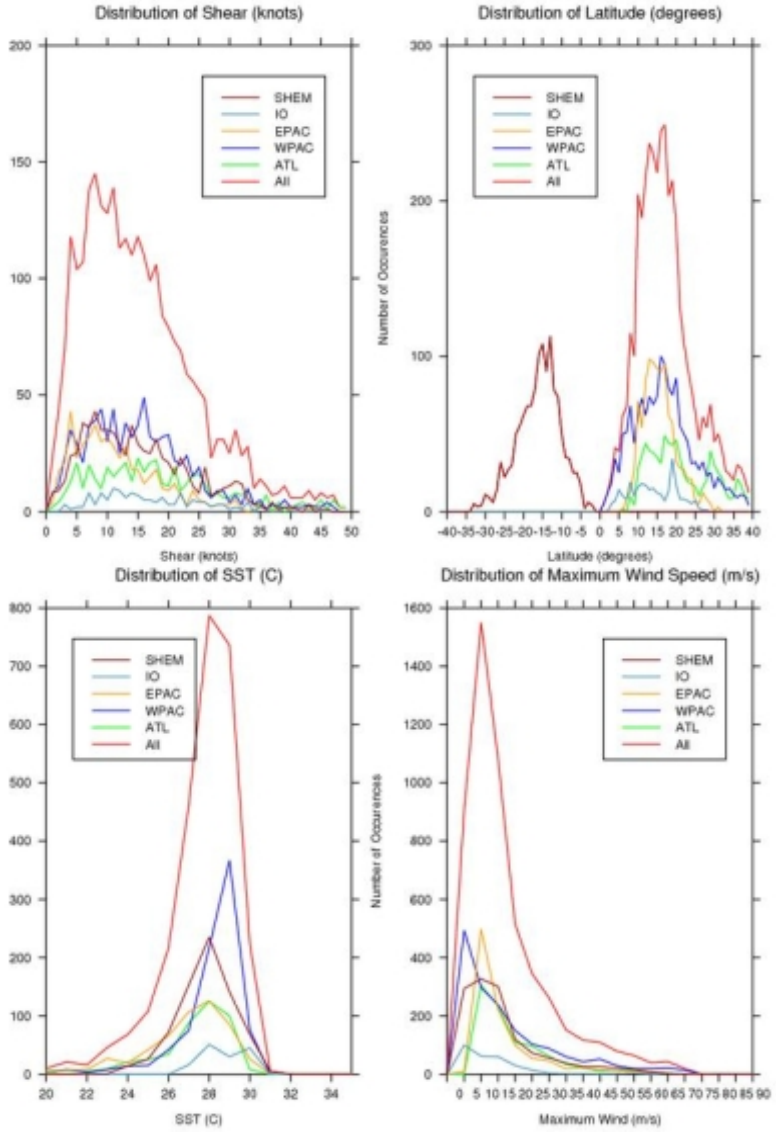

FIGURE 3.2: Distribution of CloudSat overpasses with respect to SST, shear, maximum winds and latitude for all basins

3.2.1 Formation (Genesis)

The formation stage of a TC starts with an convective cumulus cloud cluster over the ocean. An overpass of TD Bilis in the WPAC on July 8, 2006 provides an excellent example of a developing TC. The system formed northeast (NE) of the WPAC Yap islands on July 7, 2006 ([Padgett, 2006b]) and slowly intensified during the next few days, Figure 3.3 shows the time series of SST, wind shear and maximum wind speed for the lifetime of the system. The MODIS

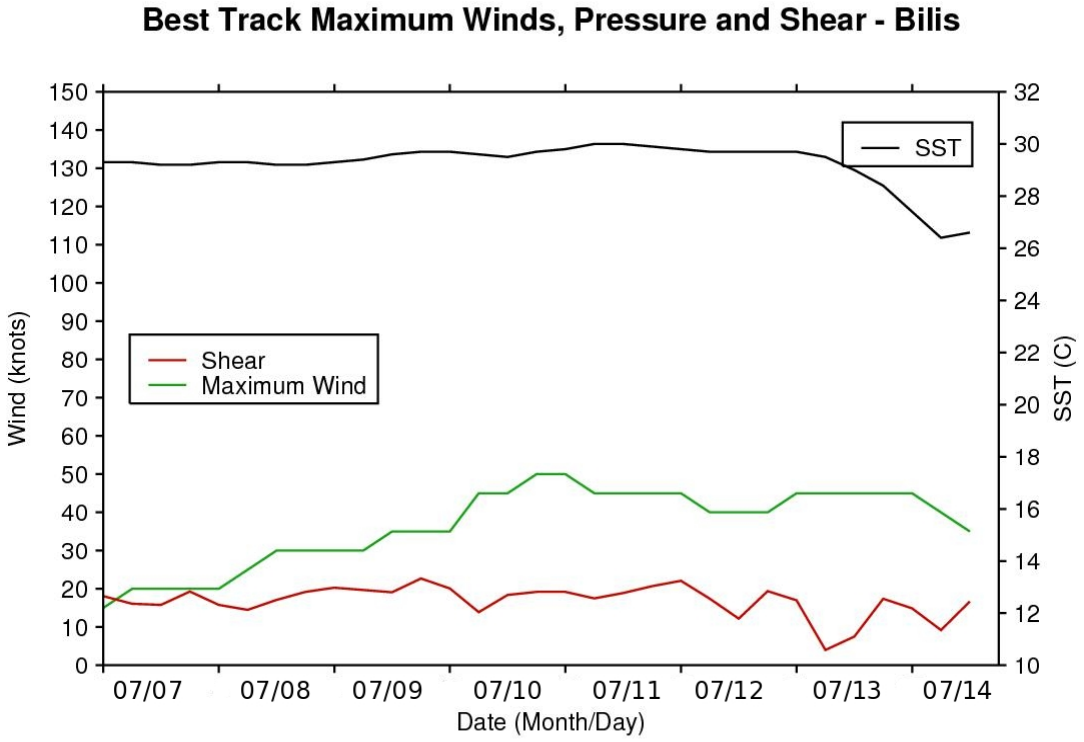

FIGURE 3.3: Best track maximum wind speed, shear (SHIPS) and SST (Reynolds) for TD Bilis.

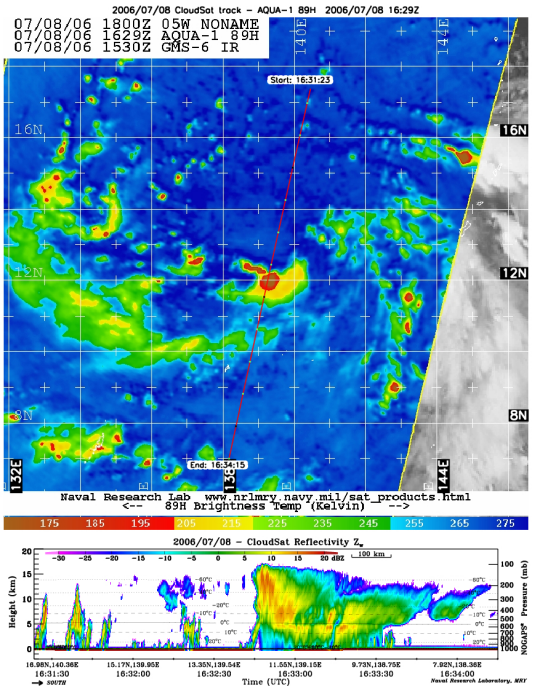

FIGURE 3.4: AMSR-E overpass of Bilis on July 8, 2006. Image courtesy of NRL.

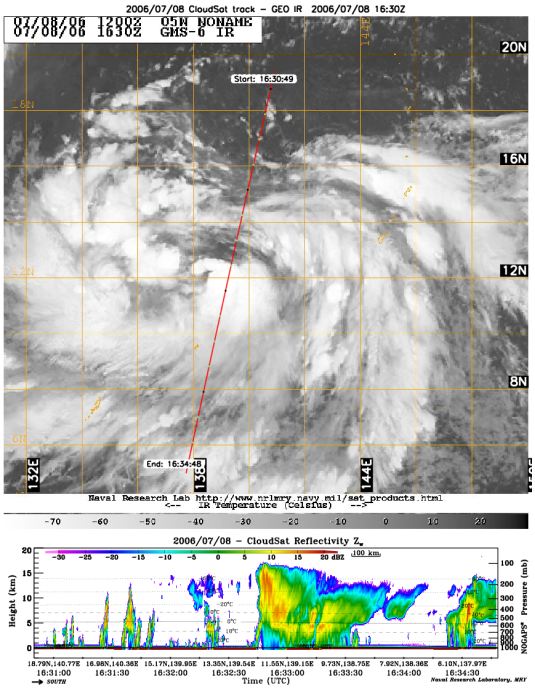

FIGURE 3.5: MODIS overpass of Bilis on July 8, 2006. Image courtesy of NRL.

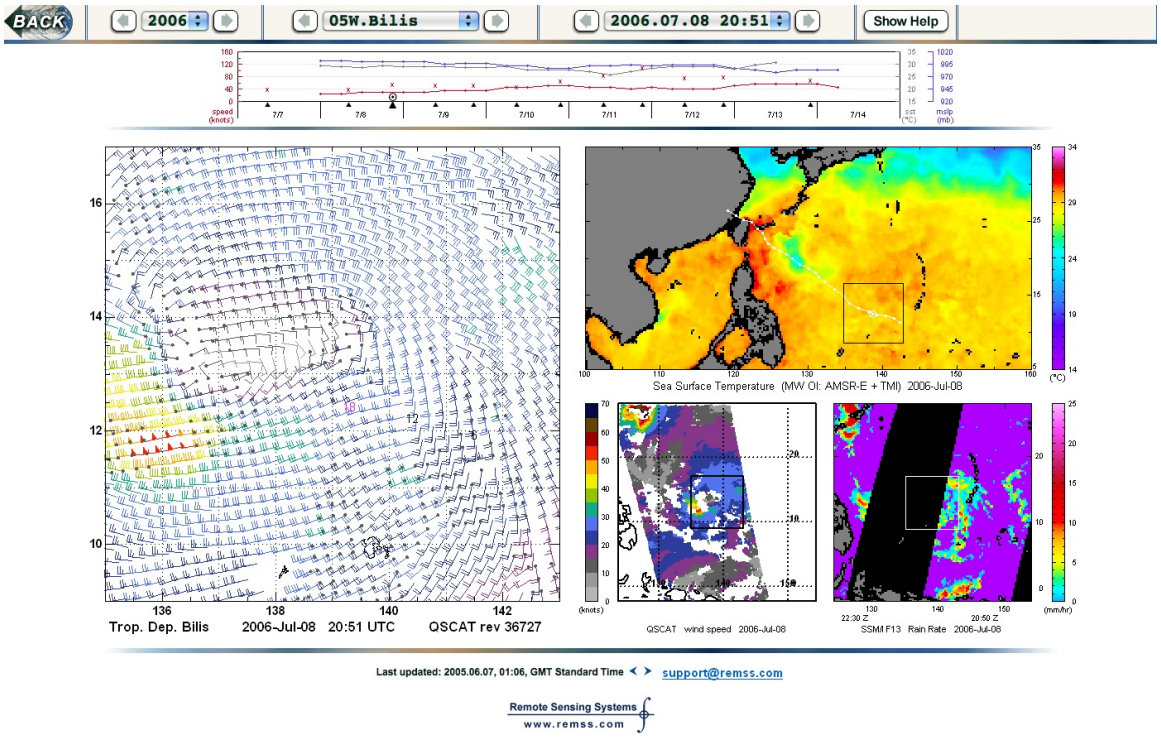

FIGURE 3.6: TC environment for TD Bilis on July 8, 2006 - QSCAT wind, AMSR-E/TMI SST and SSM/I F13 rain rate. SSM/I, TMI, AMSR-E and QuikSCAT data are produced by Remote Sensing Systems and sponsored by the NASA Science MEaSUREs DISCOVER project, AMSR-E Science Team and NASA Ocean Vector Winds Science Team.

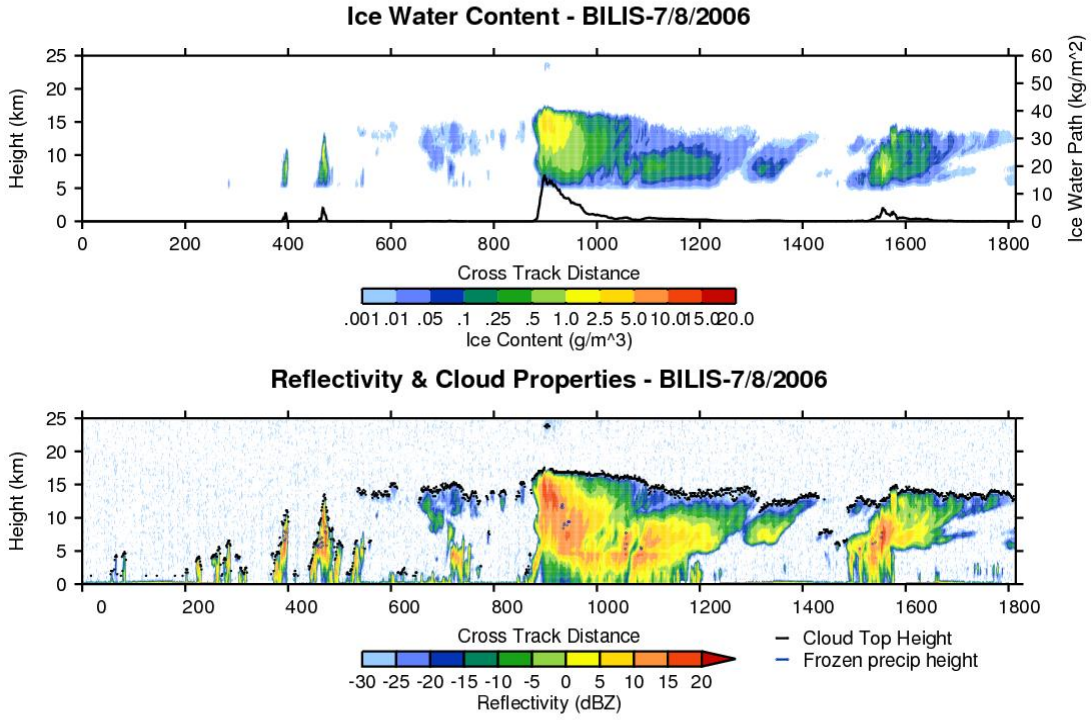

FIGURE 3.7: CloudSat reflectivity and ice content, MODIS cloud top height and frozen precipitation height for TD Bilis on July 8, 2006.

and AMSR-E image taken on July 8, 2006 (Figures 3.4 and 3.5) shows the cumulus cluster beginning to organize as a counter-clockwise surface circulation develops. Strongest winds are confined to the southwest (SW) quadrant moving in an east-southeast (ESE) direction (Figure 3.6). Conditions were considered favorable for TC development; warm SST ($>$ 29.0 °C) and low wind shear ($<$ 20 knots) (Figure 3.3). The CS CPR overpasses the center of the strongest convection developing on the southern side of the system. High reflectivity values around 15 dBZ extend over 15 km and very heavy rainfall ($>$ 25 mm/hr) is evident from the attenuation (loss of signal) below the melting layer (Figures 3.7 and 3.8). AMSR-E 89 GHz temperatures in the area of deepest convection measure 150 K (Figure 3.9). Ice is starting to accumulate in the upper portions of the system under the more vigorous updrafts (Figure 3.7). CTH's are close to 17 km and gradually slope outwards. Strong surface winds occur SW of the deep convection, evidence of the strong inflow into the TC center (Figure 3.6). SST measurements confirm warm ocean water temperatures over 29°C (Figure 3.6). CS cloud classification reveals deep convective

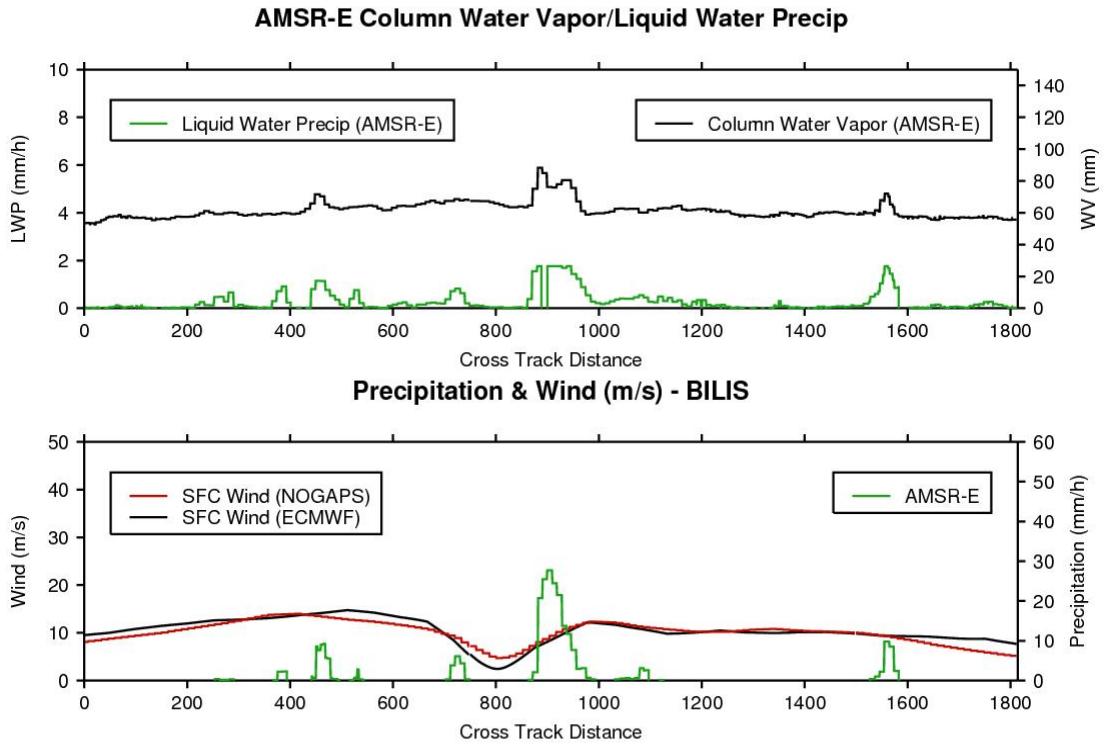

FIGURE 3.8: AMSR-E precipitation, NOGAPS and ECMWF surface winds, AMSR-E column water vapor and liquid water precipitation for TD Bilis on July 8, 2006.

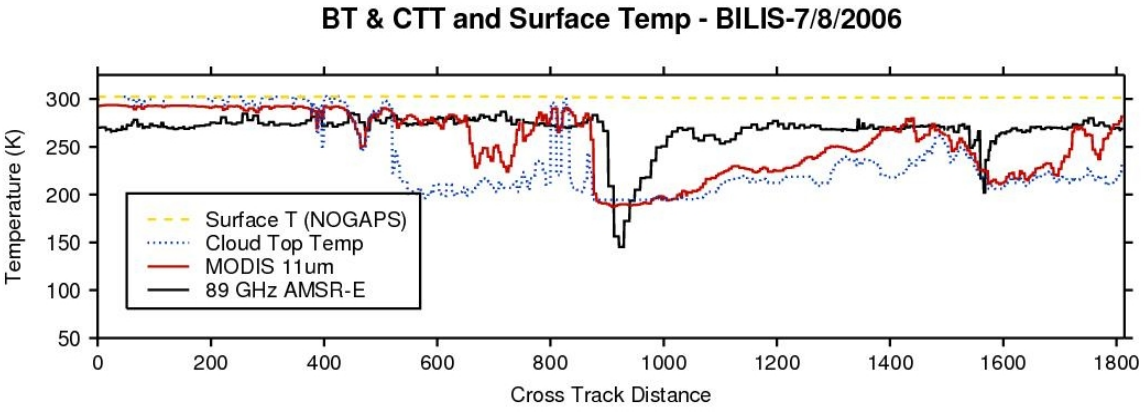

FIGURE 3.9: AMSR-E 89 GHz and MODIS 11μm brightness temperature, cloud top temperature and surface temperature for TD Bilis on July 8, 2006.

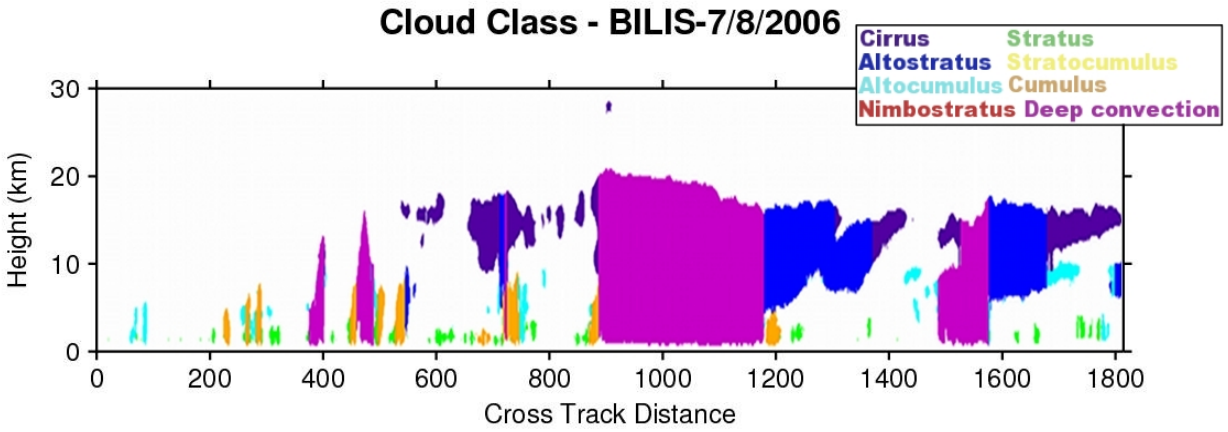

FIGURE 3.10: CloudSat cloud classification for Tropical Depression Bilis on July 8, 2006.

cloud types in area of highest reflectivity. CI and AS are detected above 7 km with stratus and cumulus clouds in the lowest five km (Figure 3.10). TD Bilis went on intensify to a severe TS but weakened as the storm started to entrain dry air at the upper levels as it approached the coast of northern Taiwan ([Padgett, 2006b]).

3.2.2 Intensification (Deepening)

The next stage of TC development, intensification (deepening) of a system is illustrated by the overpass of TC Arthur on January 24, 2007 in the SHEM. Arthur formed on January 21, 2007 as a weak depression 435 km west-northwest (WNW) of the island of Somoa in the South Pacific ([Padgett, 2007]), Figure 3.11 shows the time series of SST, shear and maximum wind speed for the lifetime of the system. Initially, the storm encountered wind shear and unfavorable upper tropospheric conditions as the system moved slowly northwest (NW) from January 21st to the 24th. Early on the 24th, the system started to encounter an upper level anticyclonic feature which enabled the system to rapidly intensify. Maximum wind speed increased by 40 knots and pressure dropped 26 mb in 18 hours (Figure 3.11). IR imagery (Figure 3.12) reveals the large white cloud mass and cyclonic structure starting to form on Janaury 24, 2007 at 12 UTC. It is difficult to identify the storm center as the system is completely covered by high clouds. The AMSR-E overpass of the same area (Figure 3.13) reveals the low BT (red areas) in the

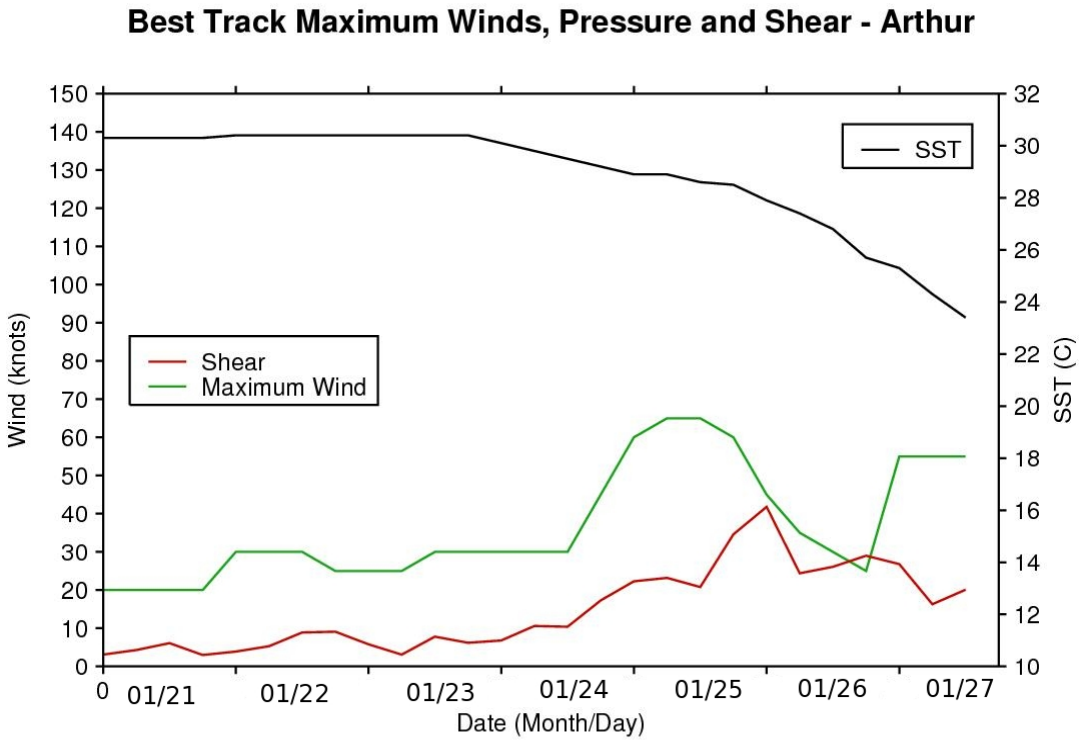

FIGURE 3.11: Best track maximum wind speed, shear (SHIPS) and SST (Reynolds) for TS Arthur.

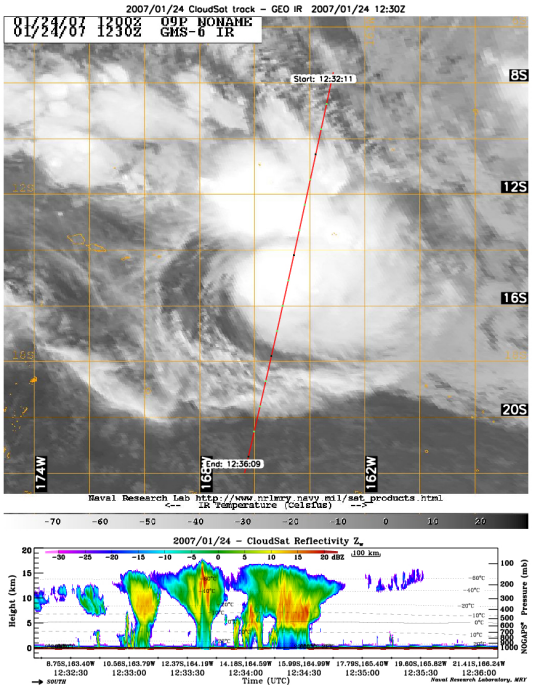

FIGURE 3.12: MODIS imagery with CS overlay for TS Arthur - January 24, 2007. Image courtesy of NRL.

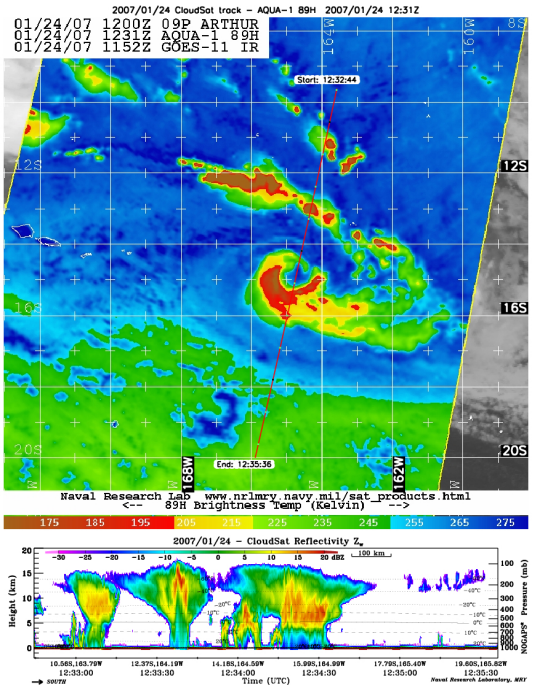

FIGURE 3.13: AMSR-E imagery with CS overlay for TS Arthur - January 24, 2007. Image courtesy of NRL.

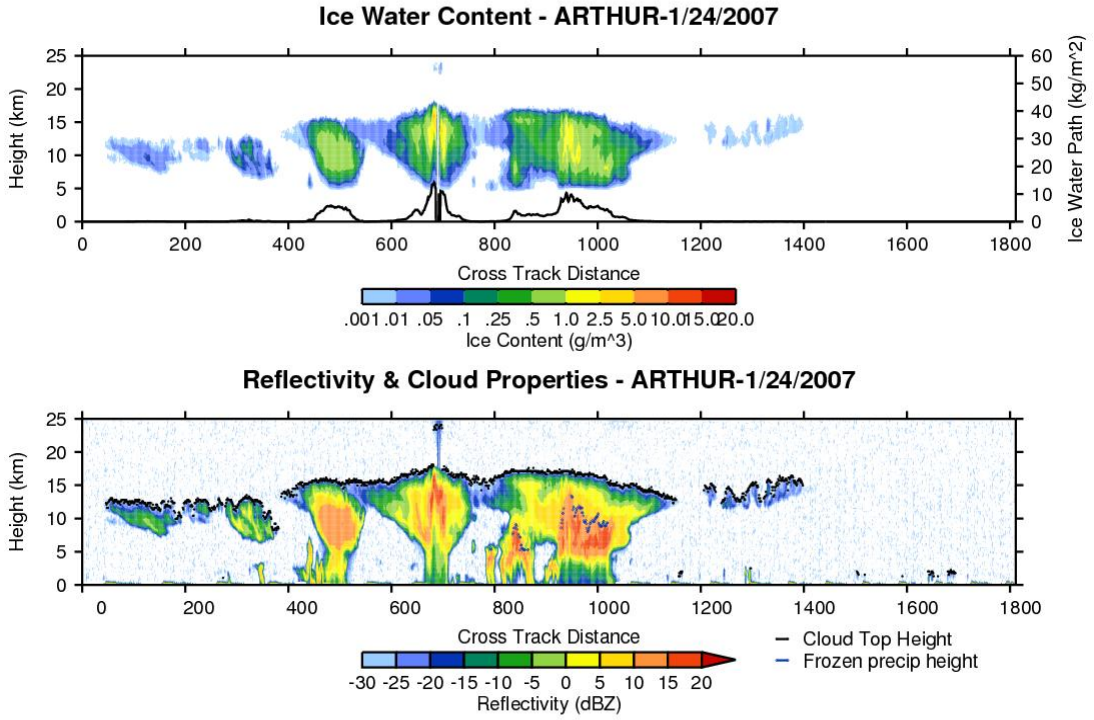

FIGURE 3.14: CloudSat reflectivity and ice content, MODIS cloud top height and frozen precipitation height for TS Arthur on January 24, 2007.

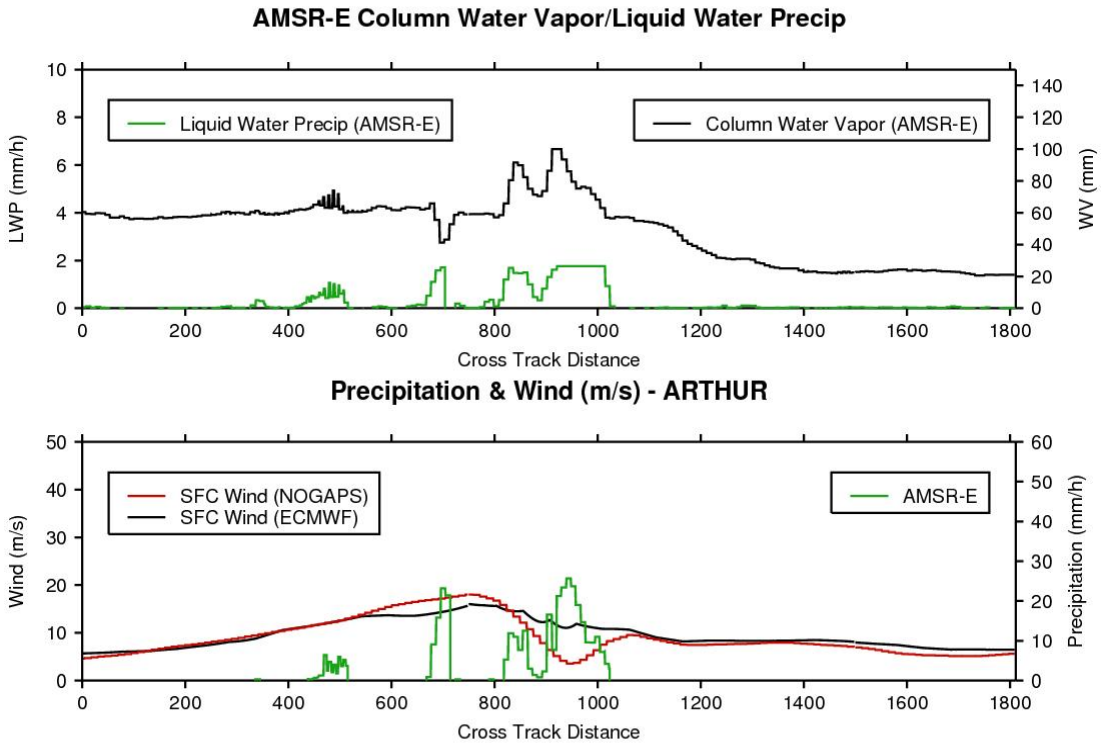

FIGURE 3.15: AMSR-E precipitation, NOGAPS and ECMWF surface winds, AMSR-E column water vapor and liquid water precipitation for TS Arthur on January 24, 2007.

deepest convection. The upwelling radiation (measured as BT) is being depleted by water and ice particles. An eyewall is starting to build on the southern side of the system with an eye forming in the middle. Strong updrafts push the deep convection ($\geq$ 15 dBZ) up over 15 km in height. The extreme CTH ($\sim$ 24 km) in Figure 3.14 captures an intense cumulus tower, most likely an overshooting cloud top attenuating the CPR signal.

The storms IWC (Figure 3.14) is confined to areas of deep convection ($\geq$ 15dBZ) above eight km in height. The corresponding AMSR-E BT (80°C) confirms the cold, overshooting cloud tops (Figure 3.15). IWP column values are less 15 $\mathrm{g\,m^{-2}}$ in this area. AMSR-E measures rainfall rates over 25 mm/h in the heavier convective cores, the AMSR-E column water vapor decreases in the intense convective core due to contamination by heavy rainfall (Figure 3.15). The SSM/I F13 (Figure 3.16) observes rain rates up to 15 mm/hr in the corresponding areas, much lower than AMSR-E observations and more likely an underestimate. Strong cyclonic

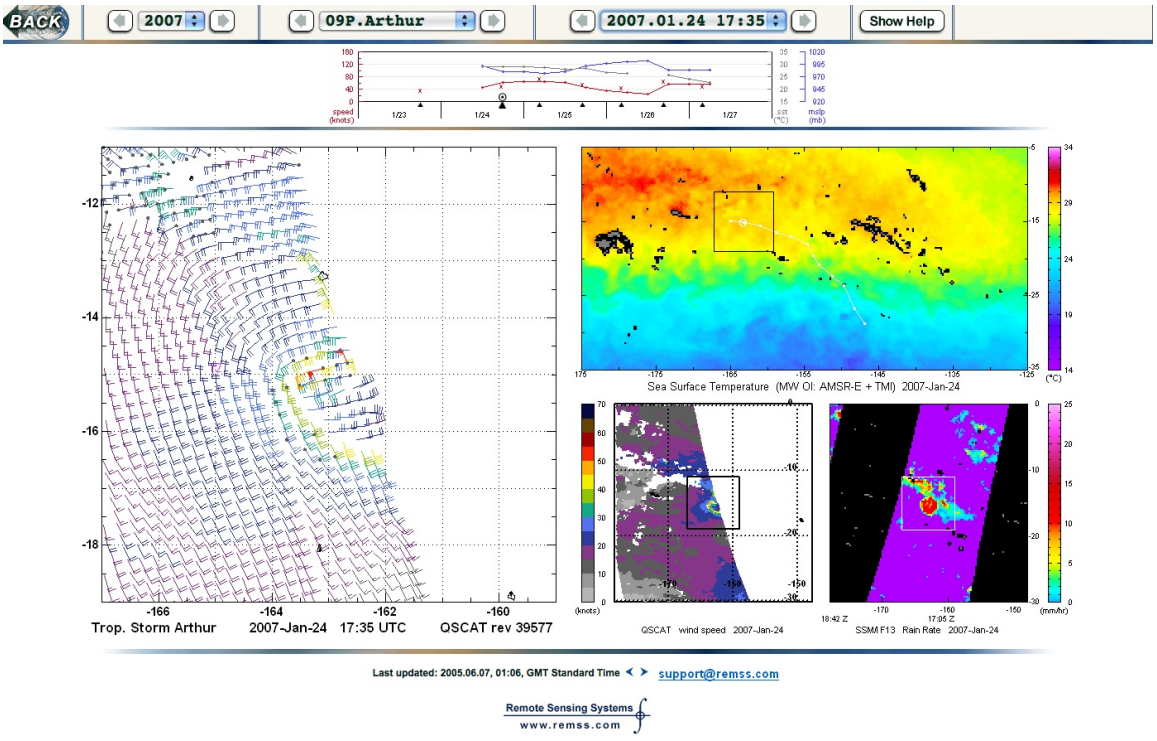

FIGURE 3.16: TC environment for TS Arthur on January 24, 2007 - QSCAT wind, AMSR-E/TMI SST and SSM/I F13 rain rate. SSM/I, TMI, AMSR-E and QuikSCAT data are produced by Remote Sensing Systems and sponsored by the NASA Science MEaSUREs DISCOVER project, AMSR-E Science Team and NASA Ocean Vector Winds Science Team.

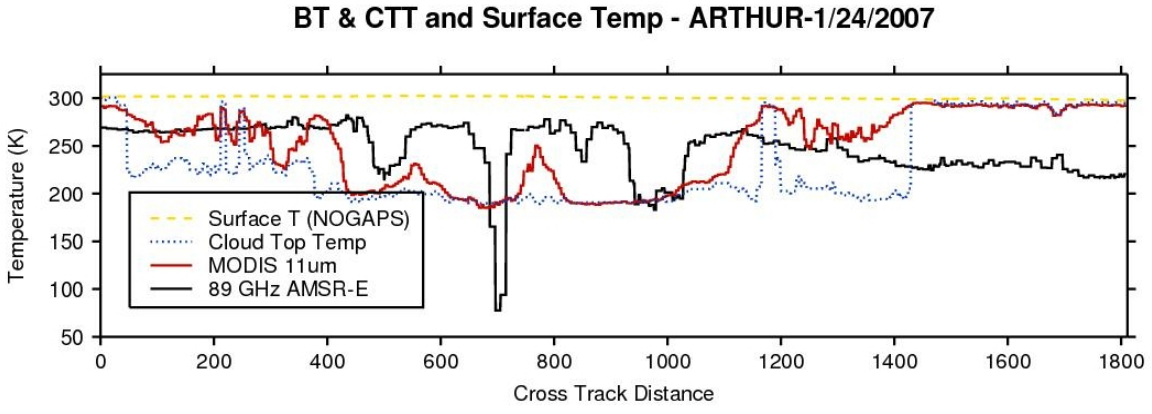

FIGURE 3.17: AMSR-E 89 GHz and MODIS 11μm brightness temperature, cloud top temperature and surface temperature for TS Arthur on Janaury 24, 2007

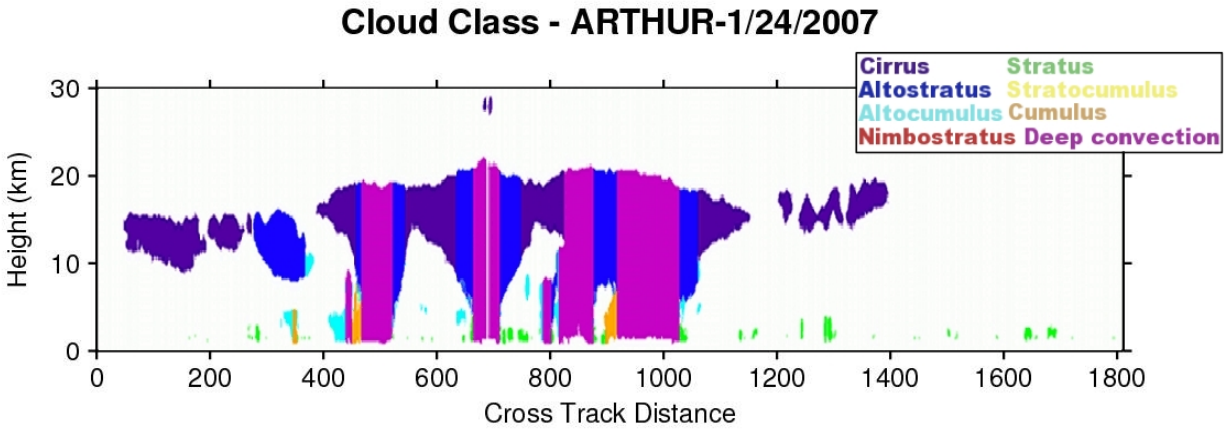

FIGURE 3.18: CloudSat cloud classification for Tropical Storm Arthur on January 24, 2007.

winds are evident from the QuickSCAT wind profile (Fig 3.16) circling around the area of deep convection. AMSR-E 89 GHz BT in the deep convective tower measure around 70 K showing the intense updrafts pushing liquid and ice droplets deep into the atmosphere (Figure 3.17). CS cloud class shows predominant cloud types of deep convective with CI and AS above eight km (Figure 3.18). Arthur started to weaken on January 26th as wind shear increased ($>$ 30 knots) and SST's decreased ($<$ 26°).

3.2.3 Mature Stage

A TC reaches full maturity when maximum wind speed and/or minimum pressure are observed in the system, although not necessarily at the same time. TD Choi-Wan formed in the WPAC on September 12, 2009, 470 miles east of Guam. Favorable upper level dynamics and large ocean heat content (OHC) quickly allowed Choi-Wan to intensify into a typhoon (TYP) on September 13th. CS overpassed the system on September 15th at 0350 UTC (maximum sustained winds of 145 mph). This is one of a few instances where CS has intersected the eye of an intense TYP. The eye of Choi-Wan is clearly visible from the MODIS (Figure 3.19) and AMSR-E (Figure 3.20) imagery. The eye is cloud free with an outward sloping eyewall. The concentric red ring around the eye (the eyewall) contains strong convective plumes and updrafts. Bright red and

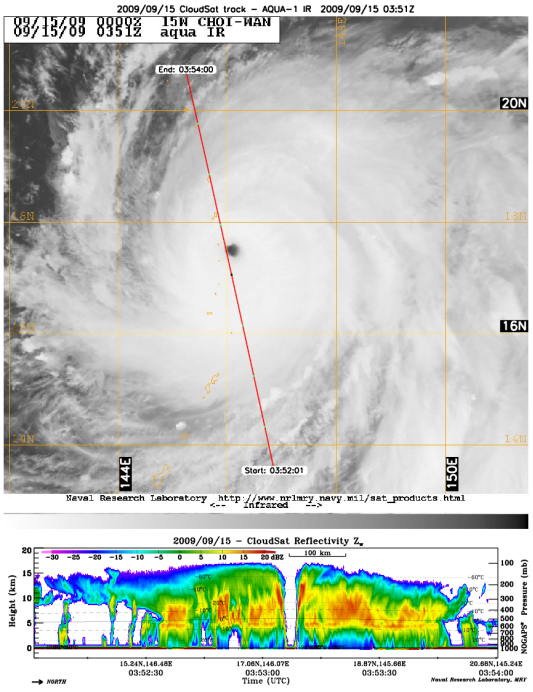

FIGURE 3.19: MODIS imagery with CS overlay for Typhoon Choi-Wan on September 15, 2009.

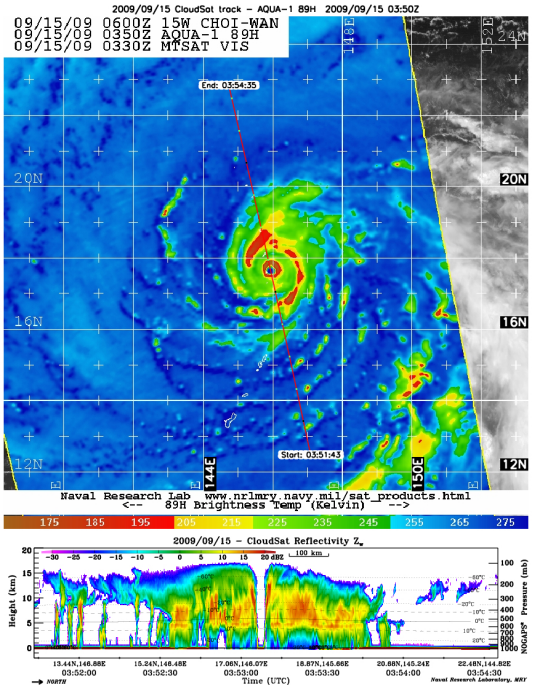

FIGURE 3.20: AMSR-E imagery with CS overlay for Typhoon Choi-Wan on September 15, 2009.

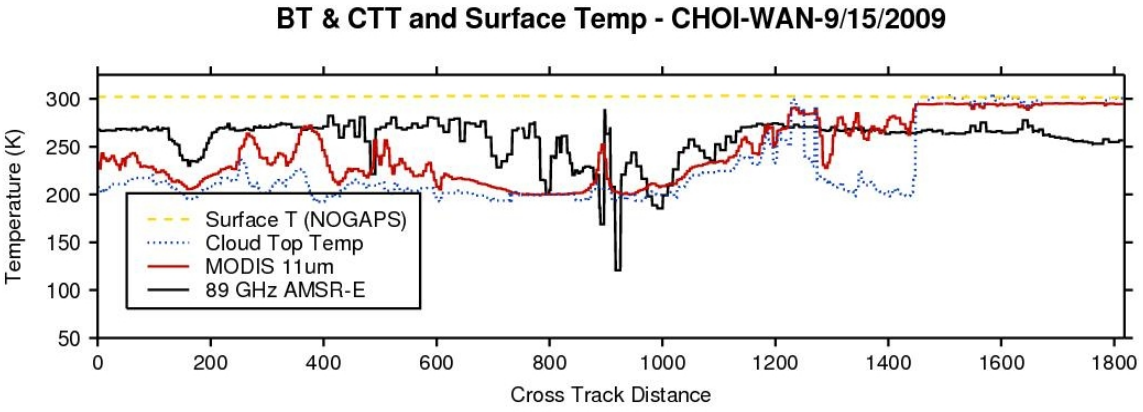

FIGURE 3.21: AMSR-E 89 GHz and MODIS 11μm Brightness Temperature, Cloud Top Temperature and Surface Temperature for Typhoon Choi-Wan on September 15, 2009.

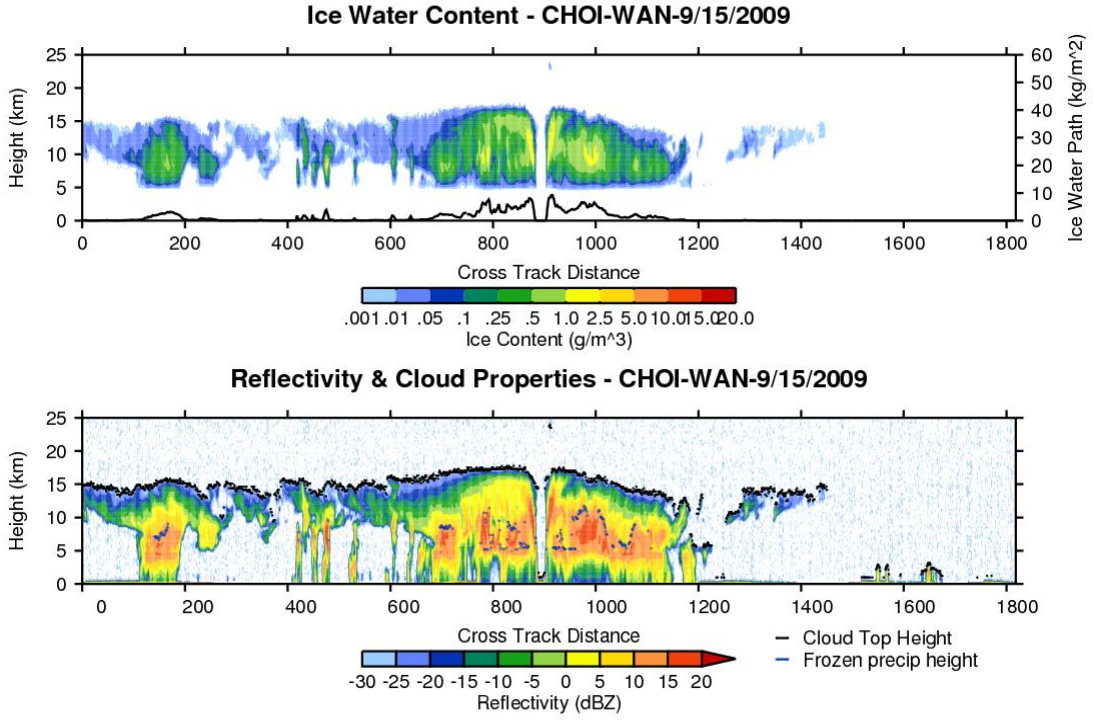

FIGURE 3.22: CloudSat reflectivity and ice content, MODIS cloud top height and frozen precipitation height for Typhoon Choi-Wan on September 15, 2009.

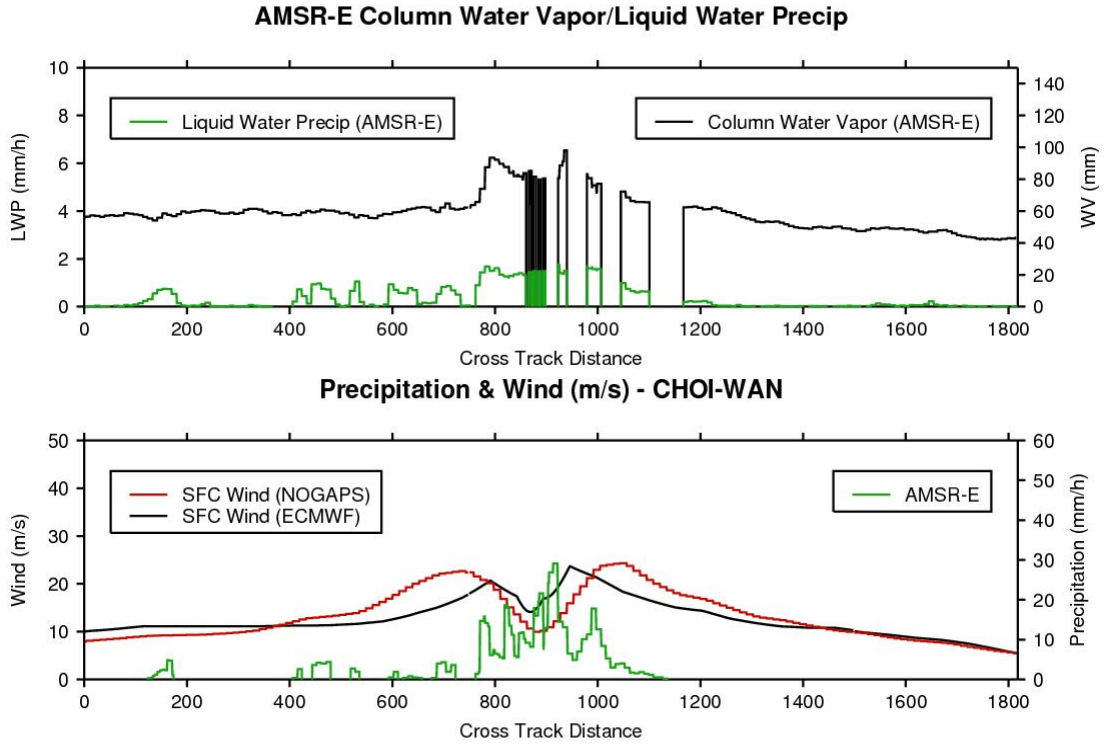

FIGURE 3.23: AMSR-E precipitation, NOGAPS and ECMWF surface winds, AMSR-E column water vapor and liquid water precipitation for Typhoon Choi-Wan on September 15, 2009.

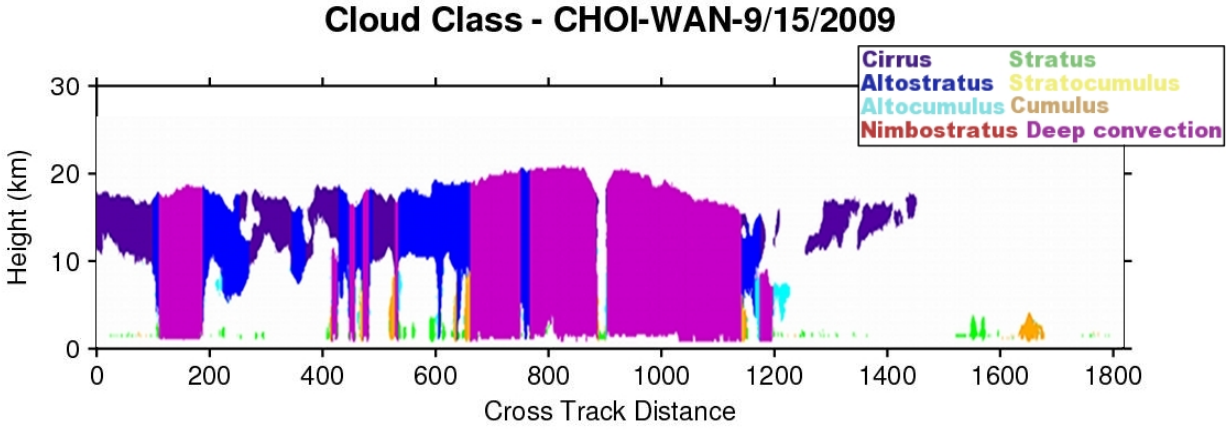

FIGURE 3.24: CloudSat cloud classification for Typhoon Choi-Wan on September 15, 2009.

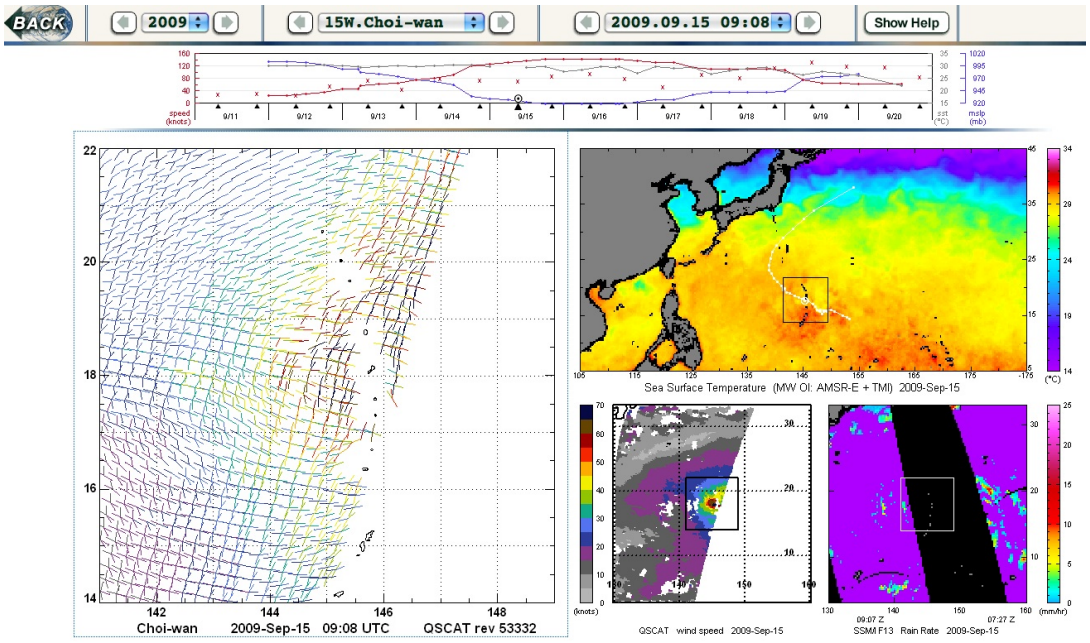

FIGURE 3.25: TC environment for Typhoon Choi-Wan on September 15, 2009 - QSCAT wind, AMSR-E/TMI SST and SSM/I F13 rain rate. SSM/I, TMI, AMSR-E and QuikSCAT data are produced by Remote Sensing Systems and sponsored by the NASA Science MEaSUREs DISCOVER project, AMSR-E Science Team and NASA Ocean Vector Winds Science Team.

yellow reflectivity bands up to almost 15 km in the atmosphere depict the intense convection. This overpass also provides a unique cross section of hot towers on either side of the eye wall. AMSR-E BT of the convective cores (hot towers) on each side of the eye are colder than other areas in the storm (Figure 3.21). The south hot tower appears to be stronger, evident from the colder BT and slightly larger IWP content. Hot towers have been theorized to occur with rapid TC intensification ([Montgomery et al., 2006], [Fierro et al., 2009]) as was the case with Choi-Wan. The undiluted cores rapidly ascend to the top of the storm from vigorous updrafts by deep convection.

CTH's peak in the storm center and gradually decrease with distance. The northern and southern eyewall are concentric on each side of the system. The southern side of the storm contains smaller, individual cells (separated by moats and clear areas in the rainbands) whereas the north side of the system contains a solid area of precipitation. IWC (Figure 3.22) is nearly symmetrical on each side of the storm with higher measurements in the eyewall region. Precipitation estimates by AMSR-E outline the areas of heavy precipitation, nearly 30 mm/hr in the

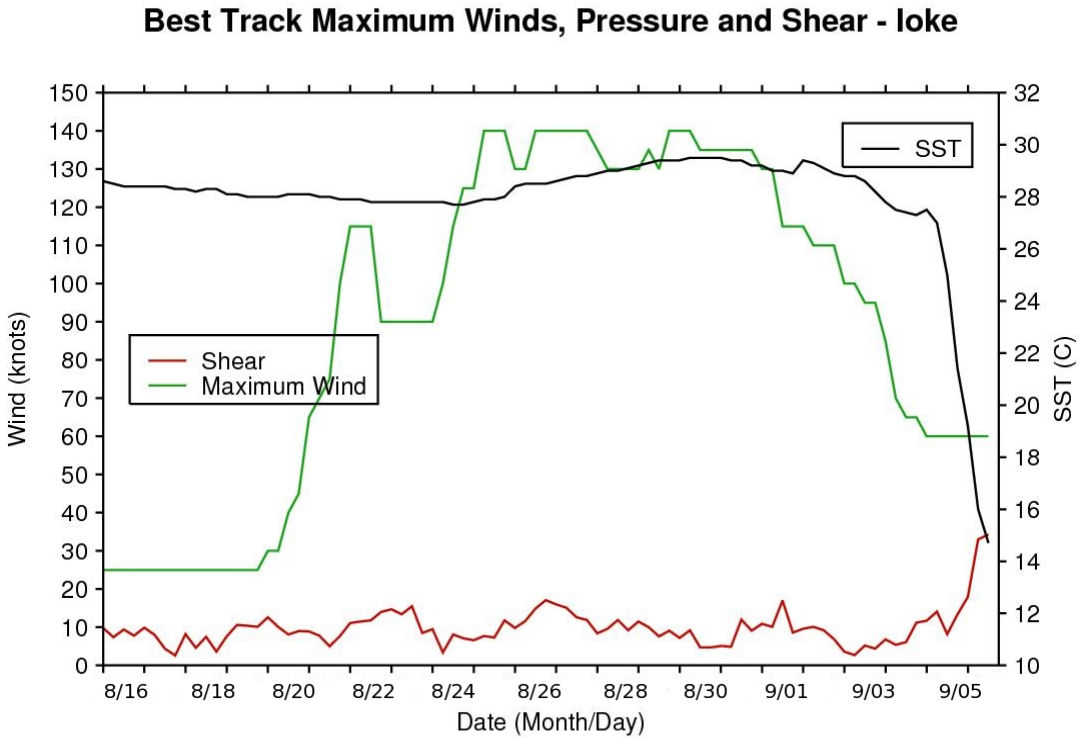

FIGURE 3.26: Best track maximum wind speed, shear (SHIPS) and SST (Reynolds) for Typhoon Ioke.

heavy convective bands (Figure 3.23). CS cloud classification identifies mostly deep convection cloud types with stratus at the base of the eye center and scattered outside the areas of deep convection (Figure 3.24). Choi-Wan was able to sustain at or near super TYP status for the next two days largely due to persistent warm SST's (Figure 3.25) and favorable upper level outflow. The system gradually weaken over the next five days as the storm moved towards the northeast (NE) encountering cooler SST's.

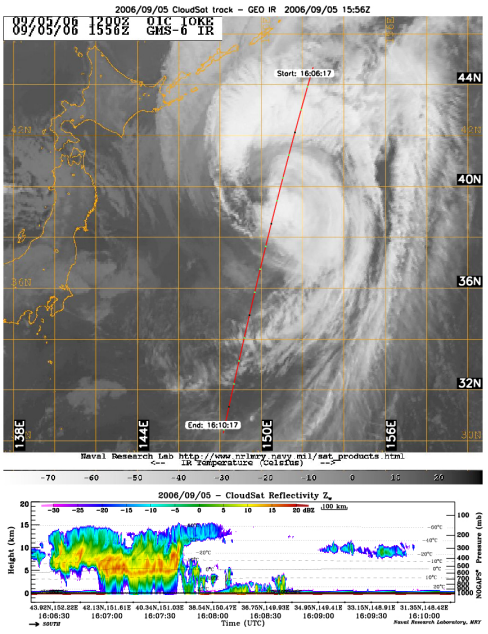

FIGURE 3.27: MODIS imagery with CS overlay for Ioke on September 5, 2006.

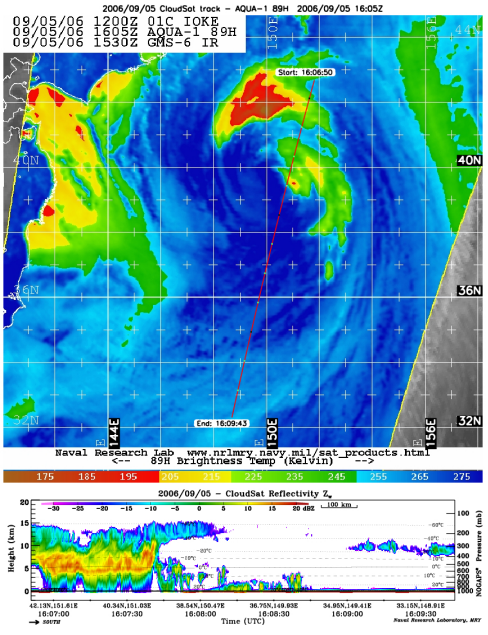

FIGURE 3.28: AMSR-E imagery with CS overlay for Ioke on September 5, 2006.

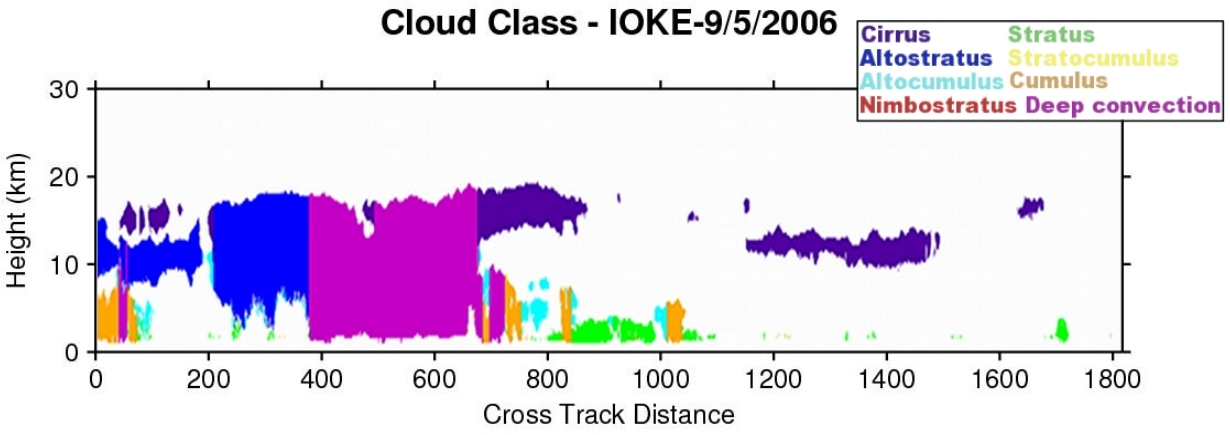

FIGURE 3.29: CloudSat cloud classification for Ioke on September 5, 2006.

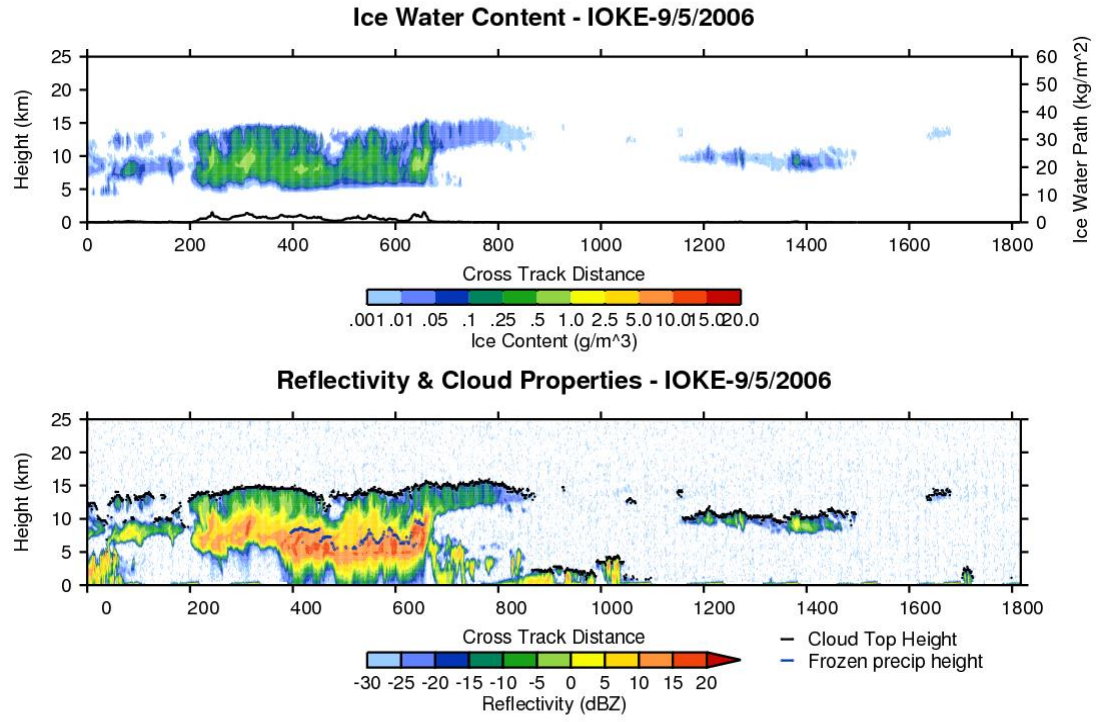

FIGURE 3.30: CloudSat reflectivity and ice content, MODIS cloud top height and frozen precipitation height for Ioke on September 5, 2006.

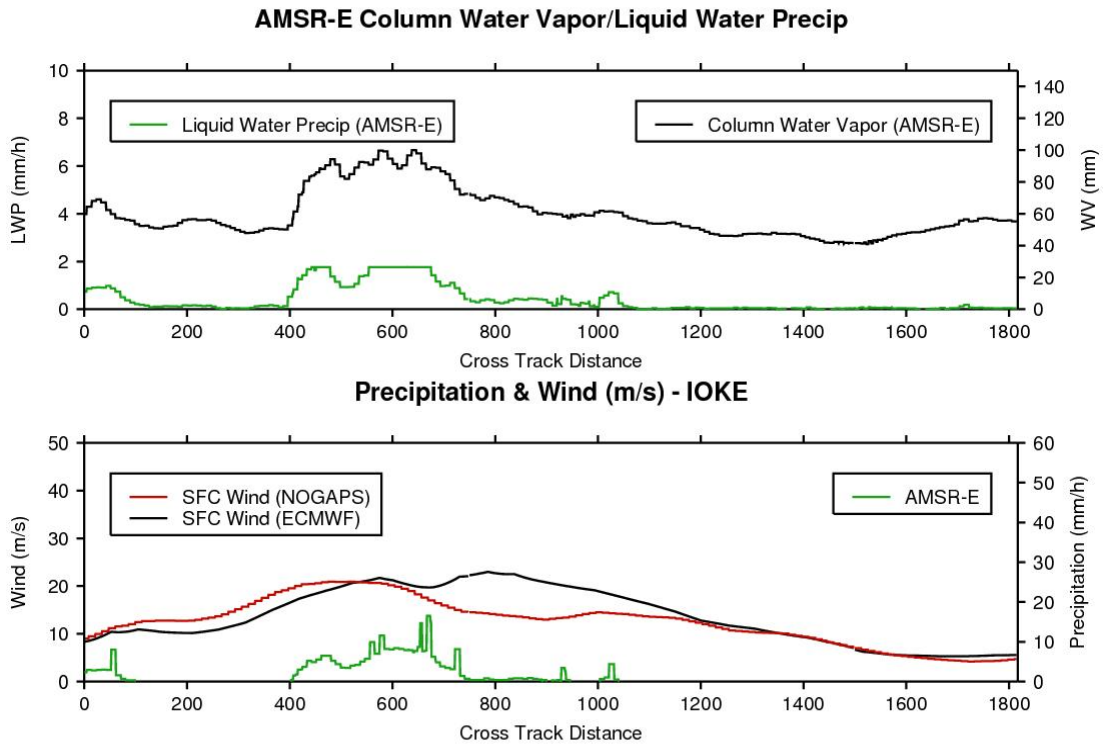

FIGURE 3.31: AMSR-E precipitation, NOGAPS and ECMWF surface winds, AMSR-E column water vapor and liquid water precipitation for Ioke on September 5, 2006

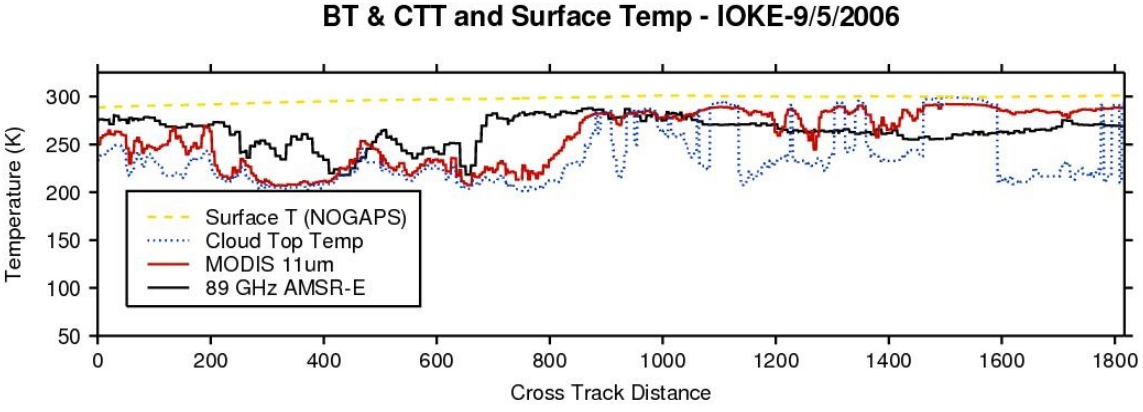

FIGURE 3.32: AMSR-E 89 GHz and MODIS 11μm Brightness Temperature, Cloud Top Temperature and Surface Temperature for Ioke on September 5, 2006.

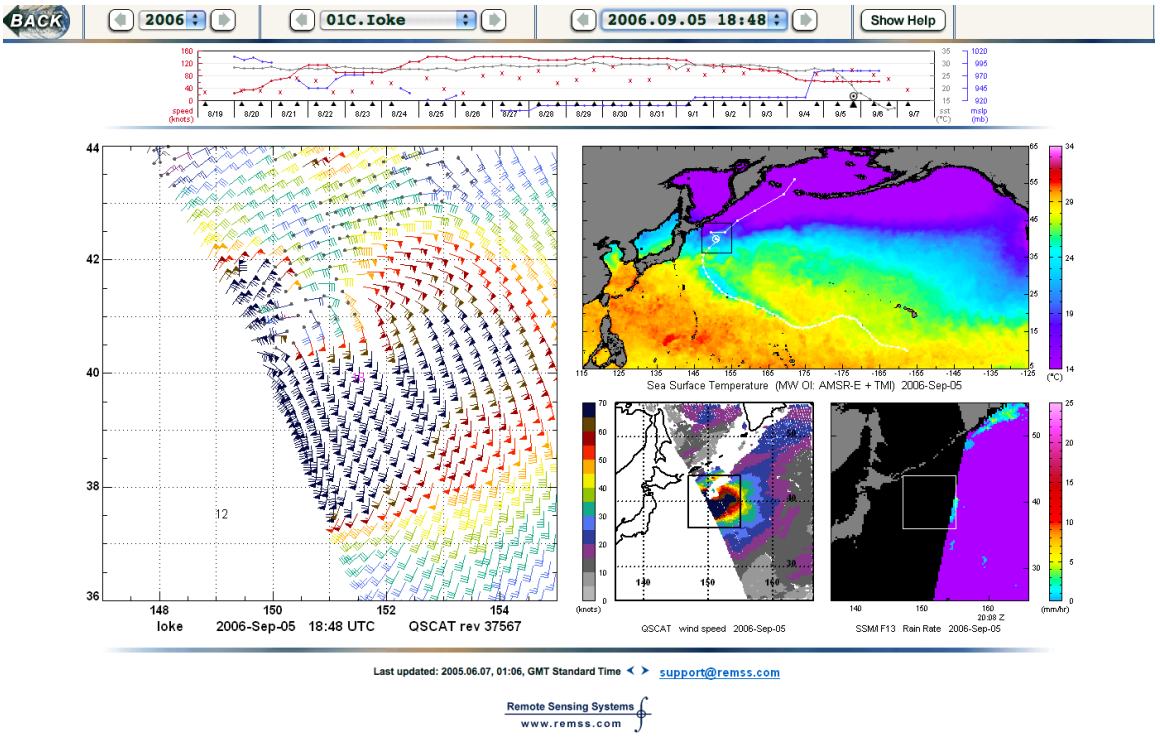

FIGURE 3.33: TC environment for Ioke on September 5, 2006 - QSCAT wind, AMSR-E/TMI SST and SSM/I F13 rain rate. SSM/I, TMI, AMSR-E and QuikSCAT data are produced by Remote Sensing Systems and sponsored by the NASA Science MEaSUREs DISCOVER project, AMSR-E Science Team and NASA Ocean Vector Winds Science Team.

3.2.4 Decay

Hurricane Ioke formed SE of Hawaii on August 20, 2006. With small amounts of wind shear and warm SSTs (28° C) the storm quickly intensified and became a hurricane in less than 24 hours (Figure 3.26). Ioke traveled WNW for the next 16 days across the CPAC and WPAC attaining HTC status the entire period ([Padgett, 2006a]). On September 2, 2006, the storm started to weaken as it moved across cooler waters in the N WPAC. On September 5, 2006, Ioke was officially declared ET (extratropical) by the Japan Meteorological Agency (JMA) coinciding with the CS overpass in Figure 3.27. The main convection is confined to the north side of the storm (Figure 3.27). AMSR-E imagery (Figure 3.28) confirms most of the rain showers and deeper convection are absent from the SE side of the storm.

TABLE 3.2: Average and standard deviation of shear, SST, maximum winds and strength for all CS TC overpasses, standard deviations are represented in parentheses. SHEM storms run from July - June. Statistics are for TC's defined with winds GT 10.3 m/s.

Basin	Year	Latitude	Longitude	SST	Shear	Wind
ATL	2006	25.0 (12.9)	-50.0 (16.6)	25.5 (5.1)	16.9 (9.6)	23.1 (11.4)
ATL	2007	25.0 (11.3)	-65.7 (20.6)	26.1 (5.0)	22.3 (11.9)	19.1 (11.1)
ATL	2008	24.4 (11.3)	-64.8 (21.8)	26.3 (4.8)	19.2 (12.7)	21.8 (10.9)
ATL	2009	23.8 (11.8)	-52.4 (23.3)	NA (NA)	NA (NA)	20.1 (11.1)
WPAC	2006	16.7 (8.3)	134.4 (16.9)	28.8 (1.3)	14.8 (9.0)	20.9 (15.6)
WPAC	2007	18.4 (8.9)	136.3 (23.0)	28.6 (1.8)	16.3 (9.3)	20.3 (15.3)
WPAC	2008	18.4 (8.4)	129.0 (13.1)	28.3 (1.8)	17.3 (10.4)	19.1 (13.7)
WPAC	2009	17.1 (8.2)	137.2 (15.3)	NA (NA)	NA (NA)	20.6 (16.6)
EPAC	2006	16.1 (4.4)	-114.2 (13.1)	27.2 (2.4)	12.5 (8.5)	20.3 (12.9)
EPAC	2007	16.2 (3.0)	-118.6 (16.5)	28.0 (1.4)	11.0 (6.5)	16.7 (8.9)
EPAC	2008	15.0 (4.2)	-111.1 (13.3)	27.1 (1.8)	13.2 (7.7)	18.0 (9.6)
EPAC	2009	17.3 (4.8)	-121.1 (15.1)	NA (NA)	NA (NA)	19.6 (12.1)
SHEM	2006	-10.7 (3.7)	93.7 (70.0)	28.6 (0.7)	17.9 (8.4)	18.8 (13.7)
SHEM	2007	-15.7 (5.2)	61.2 (87.3)	28.5 (1.4)	15.1 (8.7)	19.2 (11.7)
SHEM	2008	-15.5 (5.9)	82.1 (55.8)	27.9 (1.4)	15.9 (9.4)	18.9 (12.1)
SHEM	2009	-17.0 (5.6)	72.7 (83.5)	NA (NA)	NA (NA)	16.6 (11.6)
IO	2006	19.9 (0.4)	74.5 (9.8)	28.3 (1.2)	16.9 (10.7)	15.5 (7.1)
IO	2007	17.1 (5.4)	76.2 (12.7)	29.5 (0.9)	20.0 (9.1)	19.1 (15.9)
IO	2008	11.3 (5.0)	81.6 (12.0)	29.0 (0.7)	14.7 (4.8)	14.4 (9.5)
IO	2009	14.2 (6.3)	82.7 (6.3)	NA (NA)	NA (NA)	16.6 (11.6)

CI, AS and ST type clouds are becoming more predominant throughout the system as deep convection becomes more limited (Figure 3.29). CTH's are below 14 km (Figure 3.30), rainfall rates are less than 15 mm/hr (Figure 3.31) and BT's (Figure 3.32) are above 200 K as the storm loses TC characteristics. The storm's IWC diminished considerably except for very small amounts to the north. The height of deep convection (reflectivity above 5 dBZ) has dropped to around 11 km. As the storm continued moving NW, central pressure continued to increase, maximum winds decreased and the system moved across cooler SSTs (Figure 3.33).

TABLE 3.3: Greatest wind speed overpasses within 50 km of storm center.

Storm Name	Basin	Granule	Date	Min Dist (km)	Winds (m/s)	Press (mb)
DURIAN	WPAC	3165	12/1/06	0.5	41.2	963
NOEL	ATL	8087	11/4/07	1.4	33.4	966
PRAPIROON	WPAC	1396	8/2/06	3.3	33.4	976
ILEANA	EPAC	1711	8/23/06	5.3	54.0	955
FLORENCE	ATL	1993	9/12/06	6.2	36.0	980
FAME	SHEM	9292	1/26/08	6.9	33.4	974
NIDA	WPAC	19081	11/28/09	8.6	66.9	926
CHEBI	WPAC	2859	11/10/06	10.4	59.2	927
BILL	ATL	17655	8/22/09	10.4	41.2	964
BILL	ATL	17611	8/19/09	10.5	59.2	947
KAJIKI	WPAC	7875	10/21/07	10.9	48.9	952
USAGI	WPAC	6659	7/29/07	11.0	33.4	974
HELENE	ATL	2065	9/17/06	12.2	38.6	979
GORDON	ATL	2058	9/16/06	12.7	33.4	987
JOHN	EPAC	1805	8/30/06	13.3	51.4	965
CHOI-WAN	WPAC	17996	9/15/09	15.1	66.9	926
BILLY	SHEM	14153	12/25/08	15.6	54.0	944
UTOR	WPAC	3296	12/10/06	18.6	46.3	954
JANGMI	WPAC	12834	9/25/08	19.8	41.2	963
NAKRI	WPAC	11152	6/2/08	21.3	38.6	967
NIDA	WPAC	19103	11/30/09	23.7	51.4	948
CLOVIS	SHEM	3627	1/2/07	24.6	33.4	976
NEKI	CPAC	18540	10/22/09	24.7	51.4	965
JOKWE	SHEM	9933	3/10/08	24.9	46.3	956
VAMCO	WPAC	17646	8/22/09	25.0	48.9	959
BUD	EPAC	1092	7/12/06	26.6	43.7	974
NARI	WPAC	7366	9/16/07	27.0	38.6	967
EWINIAR	WPAC	973	7/4/06	28.2	56.6	933
MITAG	WPAC	8371	11/24/07	31.2	43.7	959
JOKWE	SHEM	9882	3/6/08	32.0	38.6	967
UTOR	WPAC	3340	12/13/06	34.0	33.4	976
ELIDA	EPAC	11766	7/14/08	36.3	33.4	987
DANIEL	EPAC	1187	7/18/06	36.5	33.4	985
PEIPAH	WPAC	8087	11/4/07	37.4	33.4	974
GULA	SHEM	9335	1/29/08	38.4	41.2	963
NAKRI	WPAC	11123	5/31/08	39.0	36.0	970
BECKY	SHEM	4853	3/27/07	39.3	33.4	976
YAGI	WPAC	2130	9/21/06	39.9	72.0	898
FITOW	WPAC	7198	9/4/07	43.1	38.6	967
KUJIRA	WPAC	16081	5/6/09	45.7	43.7	959

TABLE 3.4: Classification of Global Tropical Cyclones - Atlantic, East, Central and West Pacific. All winds are 10-minutes averages.

Winds (knots)	**Atlantic, East, Central Pacific Classification**	**West Pacific**
≤ 29	Tropical Depression	Tropical Depression
≥ 30 and ≤ 55	Tropical Storm	Tropical Storm
≥ 56 and ≤ 72	Category 1 Hurricane	Typhoon
≥ 73 and ≤ 85	Category 2 Hurricane	Typhoon
≥ 86 and ≤ 99	Category 3 Hurricane	Typhoon
≥ 100 and ≤ 119	Category 4 Major Hurricane	Super Typhoon (winds ≥ 115 knots)
≥ 120	Category 5 Major Hurricane	Super Typhoon

Chapter 4

Results

4.1 Stratifications

Previous studies of CS TC overpass data have introduced new techniques for studying these storms. ([Luo et al., 2008]), for example, used a combination of CTT, CTH and cloud profiling information from CS and MODIS observations to estimate TC intensity. Results for estimating TC intensity compare favorably to best track data with the best results from intense TC eye overpasses ($>$ 51 m/s). [Durden et al., 2009] examined CS TC overpasses within a 100 km of storm center. Quantitative estimates of cloud properties from CS and A-TRAIN data were found to be in general agreement with previous in situ observations. The following analysis will present results from the CS TC database using a combination of average reflectivity stratifications and case studies.

Analysis begins by compositing reflectivity profiles into various atmospheric regimes as a function of distance from the storm center. Previous TC composite studies consisted of NW Pacific (PAC) rawinsonde data [Shea and Gray, 1973] and aircraft reconnaissance data ([Frank, 1977a], [Frank, 1977b], [Frank, 1977c]). The studies focused on variations in the structure and dynamics of the core region in TC's and established an important tool for analysis of TC's. The compositing techniques of Shea, Gray and Frank provided the first depictions of the vertical structure of TC's based on these rawinsonde and aircraft reconnaissance data (Figure 1.1).

A similar technique is adopted here and data are averaged at 125 vertical levels. The CS TC data profiles are gathered with respect to a particular atmospheric regime; wind shear, tropical storm intensity (TD, TS and HTC strength), basin, latitude and SST. Reflectivity and height profiles (as a function of radial distance from the storm center) are averaged up to 1000 km from the TC storm center as a function of the above criteria. For example, to compute the average reflectivity for storms in the ATL, files matched to the specific basin are gathered and reflectivity, heights and radial distances are extracted from each matching CS TC file. The reflectivity profiles (and corresponding heights) are grouped according to radial distance (0-1000 km) in bins of five km width. All reflectivity profile points between 0 and 5 km, 5-10 km, 10-15 km and so forth are grouped together. The array of grouped reflectivity data is inverse base ten log averaged (heights are averaged) to produce a smaller array of average reflectivity array at each bin size as a function of average height. Only TC overpasses over the ocean are analyzed and land overpasses are disregarded. Missing reflectivity data are included in the averages as base ten logging these quantities produces negligible values.

In each of the stratification cases below, a clear line at $\sim$ 4–5 km (melting layer) reveals reflectivity values decreasing with height. In areas of moderate to heavy precipitation (typically found in TC's) the CS CPR signal becomes damped (attenuated) due to the presence of larger sized droplets and the melting of ice particles. Mie scattering occurs when particles of similar size or larger of the incident wavelength (for CS this is 3 mm) are detected by the CPR, making

it difficult to differentiate what is happening in these areas as locally large reflectivity values are damped attenuation. Thus reflectivity measurements alone in areas below the melting layer are not truly representative of what is actually happening and one must resort to the use of attenuation estimates in these regions ([Matrosov et al., 2008]). The analysis here focuses on results above the melting layer whose attenuation and multiple scattering effects are much less in the upper portion of the storm.

4.1.1 Strength

As a TC intensifies, high winds spiral thunderstorms inward toward the storm center. Water vapor condensing into liquid (or ice) droplets releases large amounts of heat and energy. Thunderstorm cloud tops rise into the upper troposphere hitting the tropopause, often overshooting and spreading out to create anvils. Figure 4.1 composites TC reflectivity according to maximum wind speed (intensity): tropical depression (TD)(winds $\geq$ 10.3 and $\leq$ 17.0 m/s), tropical storm (TS) (winds $\geq$ 17.0 and $\leq$ 33.0 m/s) and HTC strength (winds $\geq$ 33 m/s) across all basins. As TC maximum wind speed increases, the structure of the storm becomes more organized. Deeper convection extends further from the center of the storm. The first 250 km from the storm center illustrates a majority of the differences. The red reflectivity echoes (deepest convection, heaviest precipitation $\geq$ 15 dBZ) appear in HTC strength stratifications (not present in the TD/TS stratifications). The size of orange reflectivity echoes ($\geq$ 10 dBZ) increase as the convection becomes deeper and the overall layers of the storm increase in vertical size . A consistent $\sim$ 15 –16 km CTH in the first 100 km of the storm is noted.

4.1.2 Basin

The WPAC is the most active basin with around 33% of the world's TC's originating here (Figure 4.2). The basin extends westward from the international date line and north of the equator across the PAC ocean. TC's can form during any part of the year although most activity occurs

from July through October. Of the 5,277 CS overpasses, 31% of these occurred in the WPAC. Figures 4.2 and 4.3 plot the average TC reflectivity across each basin, (ATL, WPAC, EPAC, IO and SHEM) using data from June 2, 2006 –December 6, 2009 for storms of TD, TS and HTC strength. The WPAC region is more heavily weighted with TYP strength overpasses (32%), the IO basin only contains 11%. Because of the tendency for stronger storms, WPAC has the largest area of deep convection (orange reflectivity) while EPAC has the smallest. ATL overpasses are comprised of almost 50% TD strength storms.

The ATL basin contains the greatest interannual variability of number of storms with only four named storms in 1983 to 28 named storms in 2005. Wind shear conditions, mid-tropospheric relative, humidity, SST and El-Nino Southern Oscillation (ENSO) are a few of the influences on the number and strength of storms in the ATL basin. CS overpasses in the ATL (Figure 4.2 reveal deep convection (orange reflectivity) below 10 km, HTC strength overpasses account for 16% of overpasses. A slight hint of an eye in the first five km's is evident with deep convection stretching 250 km from the storm center.

The EPAC basin typically contains storms of smaller size ([Knaff and Zehr, 2007]). EPAC storms tend to develop at lower latitudes, rarely interact with upper level storm systems and usually do not undergo ET due to the presence of cooler waters north of the region and the limitations imposed by topography. EPAC stratifications confirm the smaller size relative to other basins and the lower percentage of HTC strength overpasses (only 13%). Orange reflectivity ($\sim$5 dBZ) extend around 11 –12 km vertically in the first 50 km of storm center and quickly levels off as radial distance increases. ATL, WPAC and SHEM each contain a consistent orange region of reflectivity's well beyond 250 km of the storm center whereas EPAC storms extend less than 200 km.

The SHEM basin encompasses a large ocean area containing the SW PAC basin, SIO and Australia region with (Figure 1.5) similar overpass numbers of the ATL and WPAC regions. SHEM average reflectivity layer heights are slightly lower than the WPAC region and show a subtle decrease in reflectivity in all layers around 20 km. The orange reflectivity ($\sim$ 5 dBZ) threshold hovers around 10 –11 km and decreases out to 250 km, CTH's are similar in comparison to other basins. SHEM storms tend to form in latitudes of less than 20° S and rarely venture outside this region due to large vertical shear poleward of 20° S ([Gray, 1968]).

CS overpasses in the IO basin are much lower in number, about a fifth of the overpasses compared to the WPAC basin. With the small number of data points caution should be used with the analysis. CTH's were comparable and in some areas slightly higher than regions in the WPAC profile, up to around 16 –17 km and deeper convection further from the center of storm (out to around $\sim$150 km). The IO basin is unique, it contains some of the warmest SST's due to geographical location and the presence of land masses to the north. SST's in the IO basin are around 1° higher than the PAC ocean basin ([Webster et al., 2005]). Mean tropopause temperature profiles in this area are unique as the gradient of the tropopause temperature is of opposite sign compared with other basins ([Kossin and Velden, 2004]). Tropopause temperatures are lowest where the surface temperatures are highest. The area of cold tropopause temperatures stretches NW to SE across the Arabian Sea, Bay of Bengal, South China Sea and WPAC Ocean with very low temperatures around -76°.

Figures 4.4 and 4.5 contain a subset of stratifications for storms of HTC strength (excluding the IO basin). WPAC TC's 5 dBZ convection extends the furthest from the storm center, around 350 km. The EPAC TC's show a greater hint of an eyewall (at 30 km) whereas ATL TC's reveal an eye structure around 10 km in width with deeper convection much farther from the center of the storm. SHEM TC's deep convection profiles are shallower than the other basins. ATL TC's deep convection extends further from the storm center. ATL and EPAC profiles contain less than half the number of overpasses of the WPAC basin.

4.1.3 Latitude

TC development typically occurs in areas poleward of 6° ([Gray, 1968], [Anthes, 1982]). As latitude increases, the coriolis force per unit wind speed increases due to the curvature of the earth requiring less tangential force to the balance the pressure gradient force. Diminishing effects of the coriolis force prevent the generation of vorticity, a key environmental factor in TC formation. In general, TC's typically form in latitudes of 10 –20° (N/S) although the ATL and N WPAC contain more frequent TC's developing 20° poleward ([Gray, 1968]). In higher latitudes (above 20°) TC's typically encounter lower SST's and are subject to interactions with polar jet streams, mid-latitude storm systems or ET. TC's at higher latitudes generally have lower pressure for the same radial wind profile than at lower latitudes ([Knaff and Zehr, 2007]). Lower latitude storms tend to be smaller as the result of the coriolis effect and TC's that do develop at lower latitudes tend to be smaller in size compared to storms that develop in the mid to high latitudes ([Merrill, 1984]).

CS reflectivity profiles are stratified by latitude for storms with winds greater than 10.3 m/s across all basins (Figure 4.6). TC's are divided into three equal cases with latitudes less than 12.1°, 12.1-19.2° and greater than 19.2°. The absolute value of the storms latitude in the SHEM is used for this analysis. The cloud layering structure of storms with latitudes greater than 19.2° reveal lower reflectivity profiles and a dip in reflectivity is noted in the first 10-15 km. Deep convection is more uniform and expands further with radial distance in mid-latitude cases (300 km). The percentage of HTC's increase with latitude as well.

Analyzing only HTC strength storms using three equal number of events (Figure 4.7) reveals higher latitude thresholds (14.6° and 20.2°) and different storm structure. Higher latitude ($\geq$ 20.2°) HTC's reflectivity profiles expand horizontally with deep convection limited below 10 km. Storms with latitude of 14.6° - 20.2° contain the smallest amount of deep convection extending out from the storm center (less than 200 km) and reveals a well defined eye wall at 25 km reaching 15 km vertically in the atmosphere. Storms with latitudes less than 5° reveal a similar structure. SHEM overpasses are all limited to the low shear cases whereas ATL and WPAC storms are prevalent in higher shear.

4.1.4 SST

One of the essential ingredients for TC formation is the presence of warm SST's, typically values above 26° C ([Gray, 1968]). Many studies have examined the relationship between SST and TC intensity ([Webster et al., 2005] and [Kim et al., 2009]), especially the ATL basin ([Goldenberg et al., 2001]). In general, higher SST's provide greater amounts of available latent heat and water vapor, fuel for the system to intensify (although other factors including wind shear, storm environment, available moisture and location also play a substantial role in TC formation and intensification). Likewise, a decrease in SST's can lead to the demise of a system. Seasonal, intraseasonal and multidecadel variations of SST's are influenced by natural climate phenomena such as ENSO, North ATL Oscillation (NAO), Arctic Oscillation (AO), ATL Multidecadel Oscillation (AMO) and the Pacific Decadel Oscillation (PDO). Average reflectivity (stratified by SST) is presented in Figure 4.8 grouped into three equal number of events. In the highest temperature regime (above 28.9° C), the system is well formed, CTH's are greatest towards the storm center, slope downwards with increasing radial distance and the overall profile is smooth. As SST decreases, deep convection becomes more limited vertically, the 5 dBZ threshold in the lowest SST profile ($\leq$ 27.7°) is shallower compared with higher SST's. CTH's are generally higher with increasing SST.

Examining only HTC's strength storms (Figure 4.9) reveals a change in pattern of the vertical structure from stratifications with all storm types. In cases where SST $\geq$ 29.0° C, the 10 dBZ threshold extends to around 10 km in height and higher in the eyewall region. SST's between 27.0 and 29.0° C reveal deep convection is more prevalent with a continuous layer extending out to 200 km. A taller tower (indicative of an eyewall) is detected around 30 km. In cases where SST is below 27.9° C, storm structure remains relatively intact with deep convection occurring out to 300 km from the storm center. In the higher SST regime, WPAC and IO basins are more heavily weighted whereas EPAC and ATL storms are more prevalent in the lowest SST regime. The decrease in CTH and reflectivity in high SST cases could be attributed to higher SST's being found in areas of low latitudes and by TC's forming (weak Category 1 storms) in the area then subsequently moving out of area.

4.1.5 Year

Large scale flow patterns and interannual variability play a role in TC genesis on a year to year basis. ENSO, NAO, PDO, MJO and AO, QBO (Quasi-Biennial Oscillation) can all influence where storms form, how many and how strong they are. Year to year comparisons of reflectivity for each basin are presented in Figures 4.10, 4.11, 4.12 and 4.13. SHEM is only included for 2007 (2006-2007) and 2008 (2007-2008) seasons.

Vertical profiles presented below are dependent upon the number of overpasses for each stratification case. The ATL basin contains the greatest variability in yearly overpass numbers, 337 cases in 2008 to 129 in 2006. WPAC and EPAC storm profiles all contain well over 200 overpasses per year (except EPAC 2007 with 174 cases). The SHEM basin contains a high proportion of storms due to the large geographic area (encompasses SW PAC, South Indian Ocean (SIO) and Australia area). Variability in global TC activity has been strongly linked to ENSO and to a lesser extent NAO ([Frank and Young, 2007]).

The atmospheric and oceanic conditions of 2006 were characterized by a transition from La Nina in the beginning of the year to a strengthening El Nino towards the end of the year ([Klaus, 2010]). Global SST's anomalies were generally above normal ([Arguez, 2007]) as compared to the 1971-2002 climatology. The ATL, SHEM and IO basins all experienced near normal TC activity while WPAC TC activity was slightly above normal. ATL stratifications for 2006 (Figure 4.10) were relatively low in number (129) but weighted more heavily with HTC strength overpasses than other years. Though the season started later in the EPAC basin, an expanded area of low vertical wind shear resulted in a higher than average number of storms for the basin. The SIO basin had an above normal season storm total while the SW PAC and Australia noted below normal activity due to the weak El Nino conditions developing in January 2007. Stratifications for the SHEM (Figure 4.13) in 2007 reveal consistent deep convection out to 250 km with vertical heights less than 11 km and overall CTH lower compared to WPAC and EPAC stratifications for 2006. The SHEM has small proportion of HTC overpasses ($< 20\%$) similar to EPAC numbers.

Conditions changed from a weak El-Nino in the beginning of the year (January 2007) to La Nina in mid-2007 which continued until late 2008 ([Levinson and Lawrimore, 2008] and [Peterson and Baringer, 2009]). Globally, TC activity was below average for all basins except the ATL. Deep convection ($\sim$5 dBZ) was notably lower in the WPAC for 2007 (Figure 4.11) compared to 2006. The median track for CS overpasses (Table 3.2) also shifted NW compared to normal media track (21.3N, 130.6E). EPAC stratifications for 2007 (Figure 4.12) reveal deep convection confined to areas in and near the storm center. The ATL basin stratification (Figure 4.10) is very inconsistent in the first 50 km, most likely due to the low number of HTC overpasses (10%).

During the 2008 season, near normal storm activity was observed globally except for the ATL basin which experienced an above normal season. Weaker trade winds, a more active African Easterly Jet (AEJ) and the continuation of increased SST's contributed to the increased ATL TC activity. CS stratifications for the 2008 ATL season totaled 337, the highest of all four years.

The ATL profile (Figure 4.10) reveals a 10-15 km clear eye center with deep convection extending over 12 km and gradually decreasing with radial distance. In EPAC, TC's were below normal due to the weak La Nina signal. The EPAC CS stratifications had over 234 overpasses but the vertical profile contained very shallow and weak deep convection. CTH's were well below 15 km with a much smaller area of deep convection (orange and red reflectivity) as compared to non-La Nina year (2007). The 2008 WPAC season started out with increased activity and culminated with below normal activity. The number of TYP days was well below average (75.5 compared to a normal of 120.4). The 2008 WPAC stratification is very well defined with very deep convection (red reflectivity) present out to 100 km. The SHEM experienced increased activity in the SIO, near normal activity for Australia and well below activity in the SW PAC with the season finishing much early than usual (January - February). The SHEM 2008 stratifications reveal a smaller number of overpasses (246), deep convection extending out to 200 km and a clear area above 10 km in the eye area.

In 2009, a dissipating La Nina during the first half of the year developed into a strong El Nino episode by years end. SST's were more than 2.0° C above normal in the CPAC and EPAC basin ([Arndt et al., 2010]). The EPAC basin was the only basin with above normal TC activity due to the ENSO phase. Stratifications reveal a clear eye around 20 km in width overlaid with cirrus and deep convection beyond 200 km from storm center though the deep convection is limited below 10 km. The ATL basin experienced fewer, weaker and shorter lived storms compared to other seasons but the stratifications reveal a different story. Deep convection extends over 250 km from storm center with a well defined eye center and tall convective cores just outside of the center. This was mainly due to the two direct eye overpasses of Hurricane Bill (half of the overpasses under 50 km). The WPAC basin experienced overall below normal activity but increased activity was observed towards the end of the season when the El-Nino event strengthened during September, October and November (SON). The stratifications reveal a decrease in deep convection, especially in the first 50 km and overall CTH decreased compared to previous years.

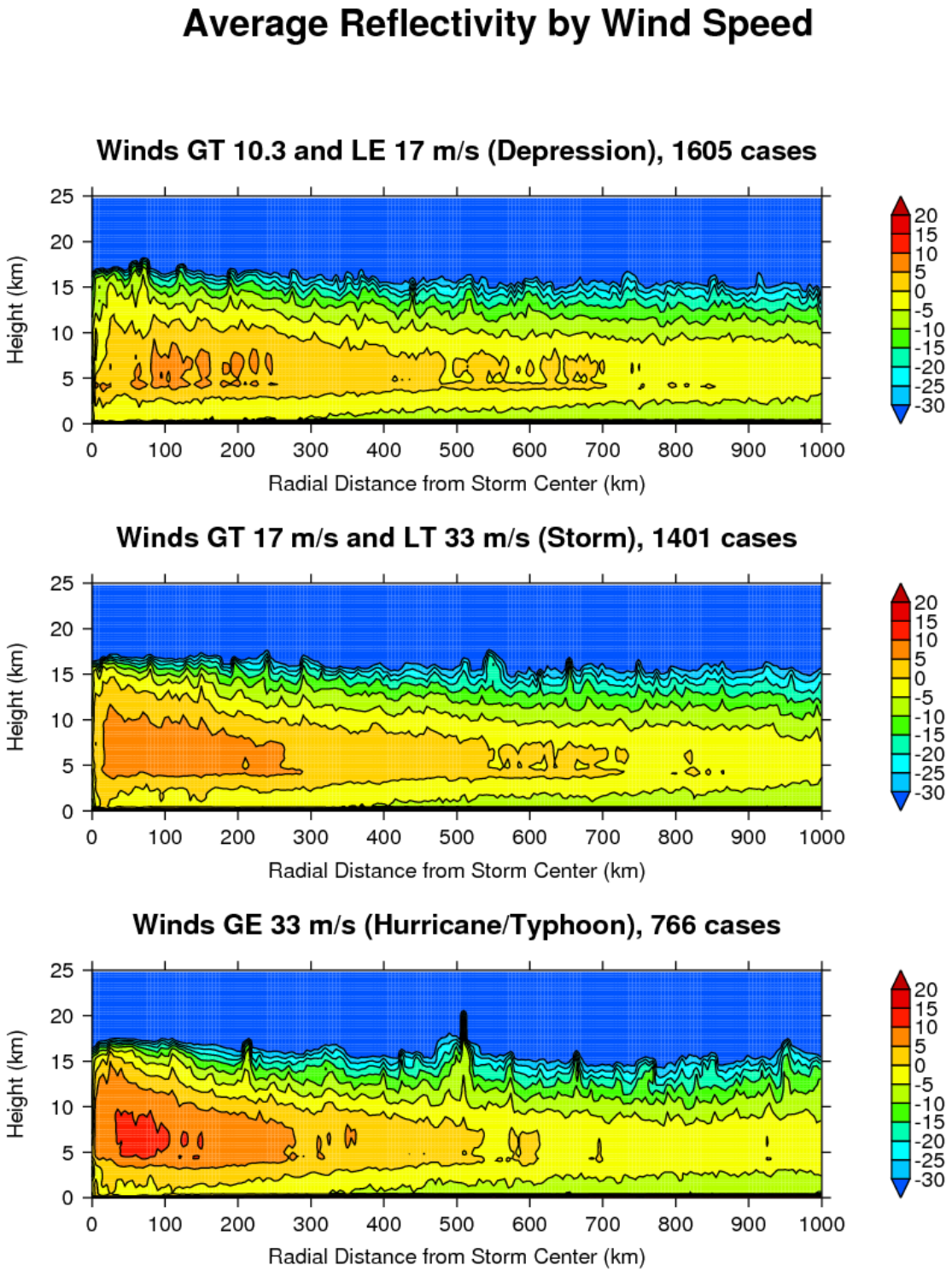

FIGURE 4.1: Average reflectivity by wind speed (storm strength) for all basins. Bottom figure is for HTC strength storms, middle figure is storms of TS strength and top figure is storms of TD strength.

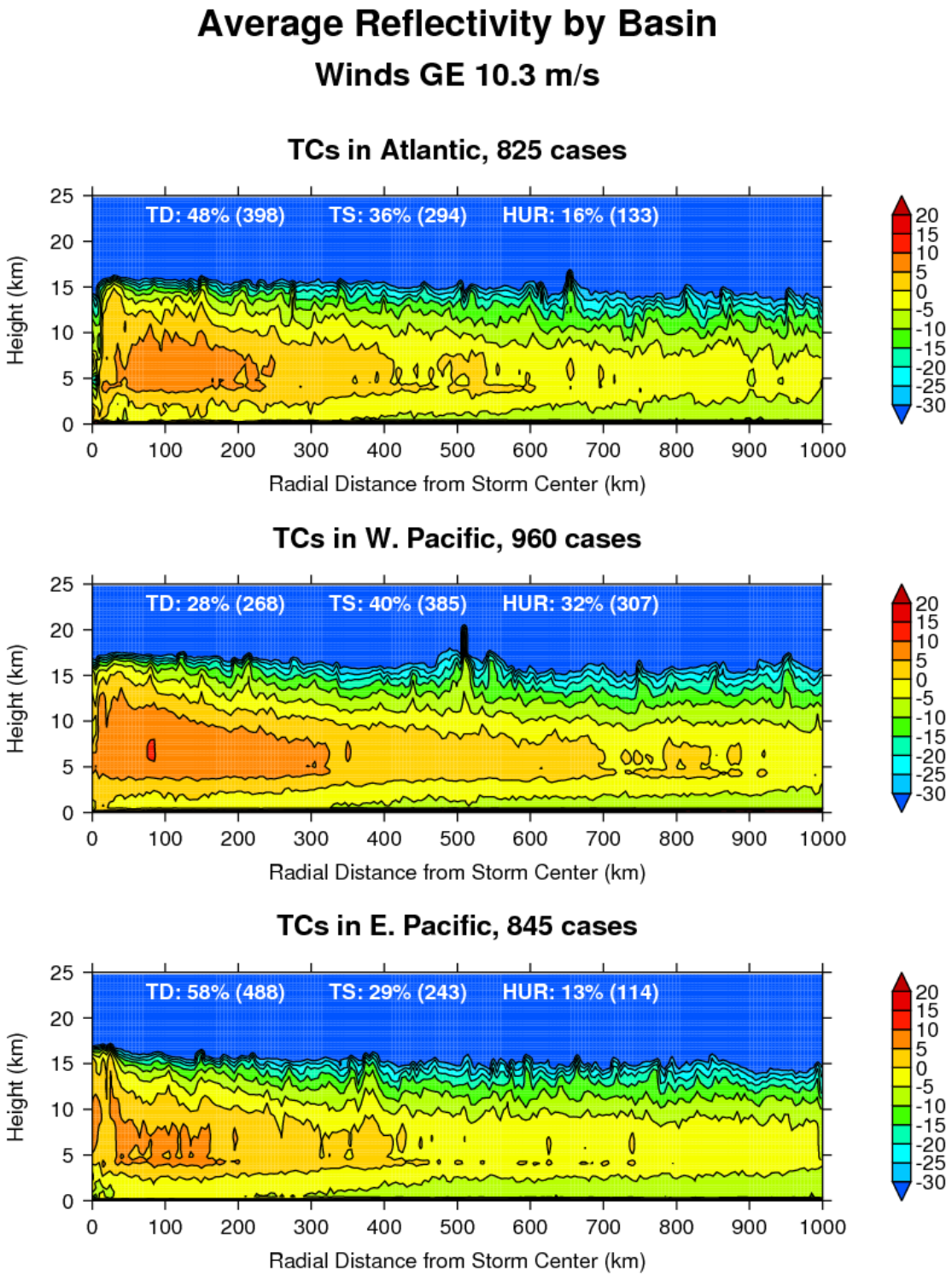

FIGURE 4.2: Average reflectivity by basin (Atlantic, W. Pacific, E. Pacific) for all storm with winds GE 10.3 m/s (23 mph)

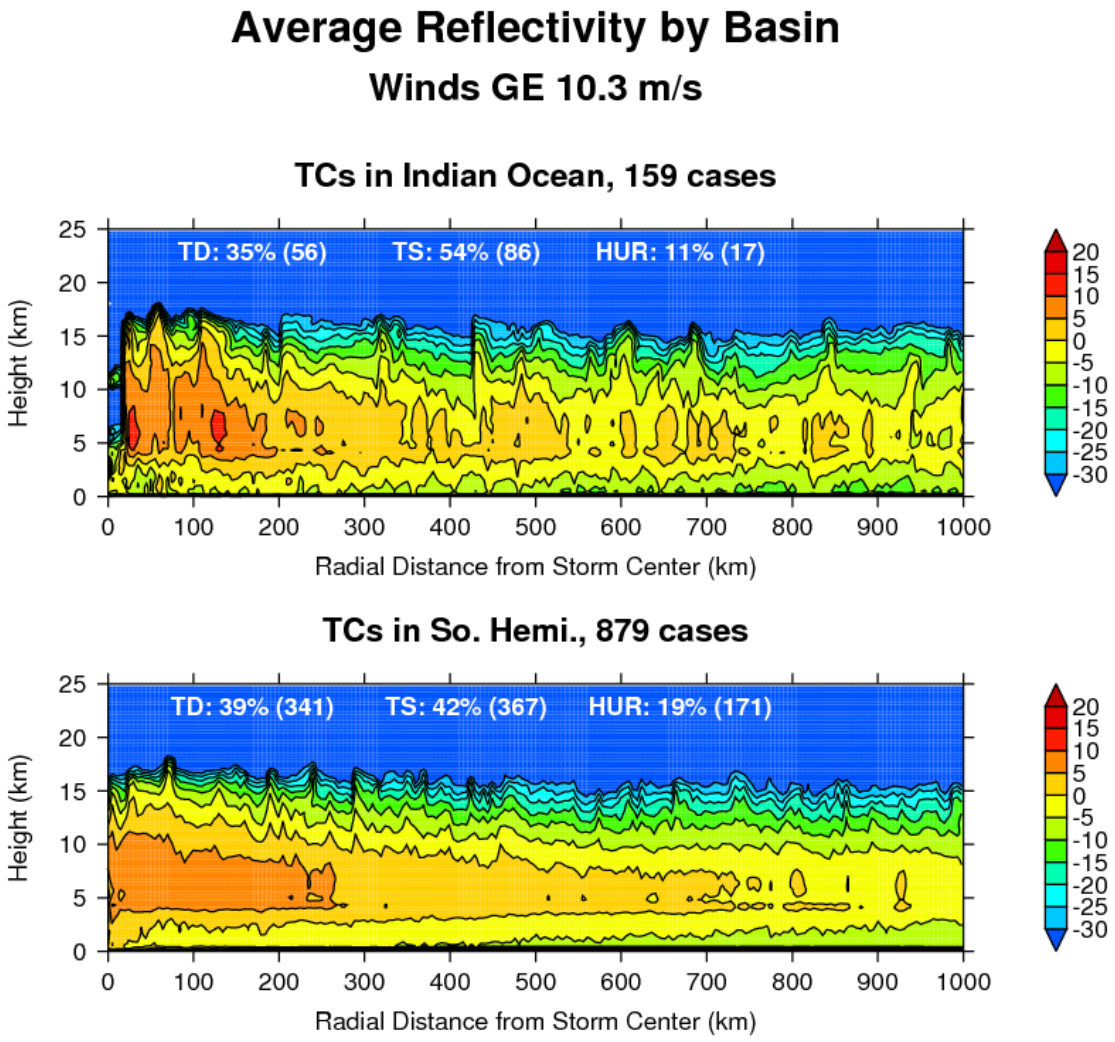

FIGURE 4.3: Average reflectivity by basin (So. Hemisphere and Indian Ocean) for all storm with winds GE 10.3 m/s (23 mph)

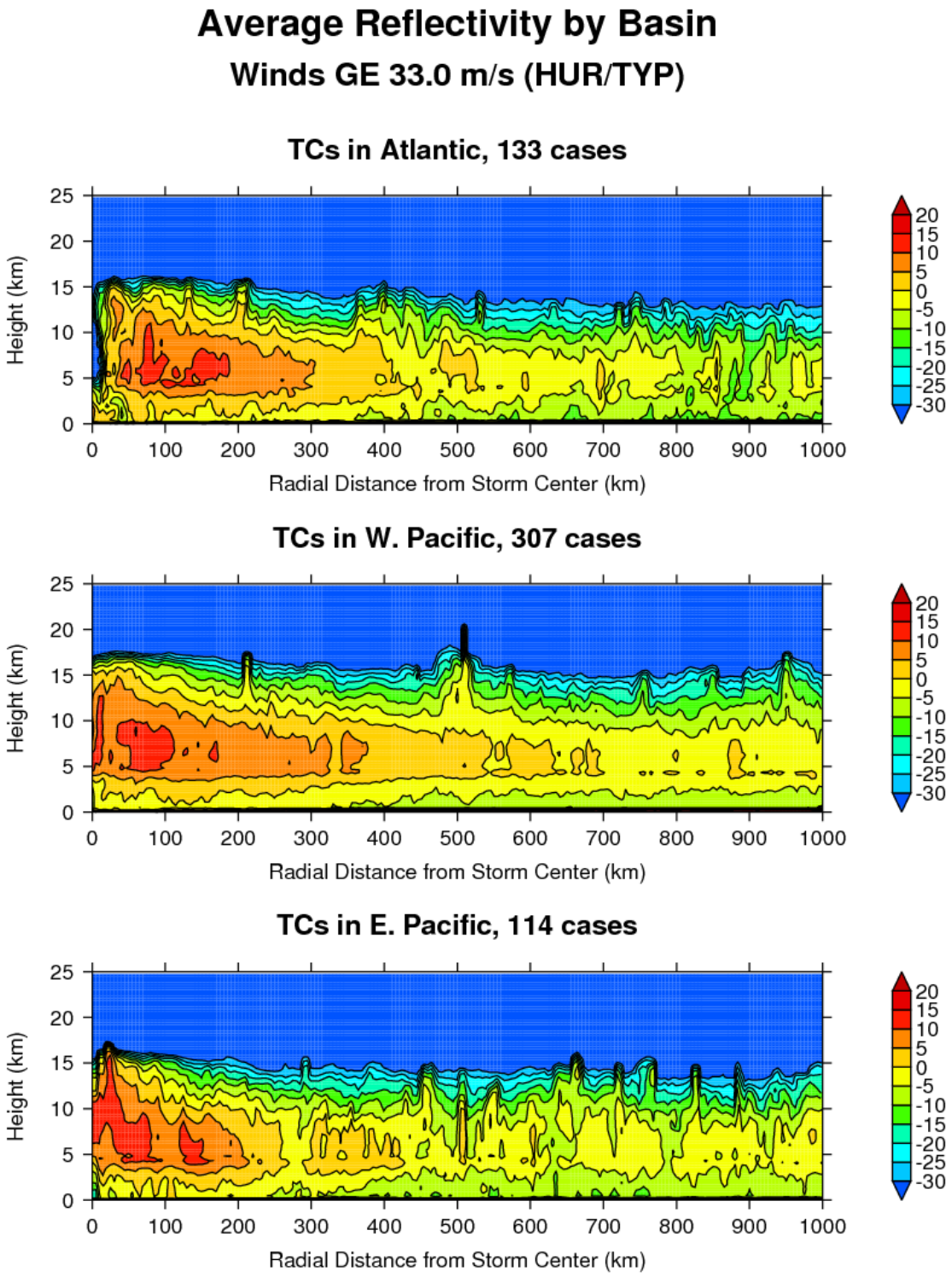

FIGURE 4.4: Average reflectivity by basin (Atlantic, W. Pacific, E. Pacific), winds $\geq$ 33.0 m/s (74 mph)

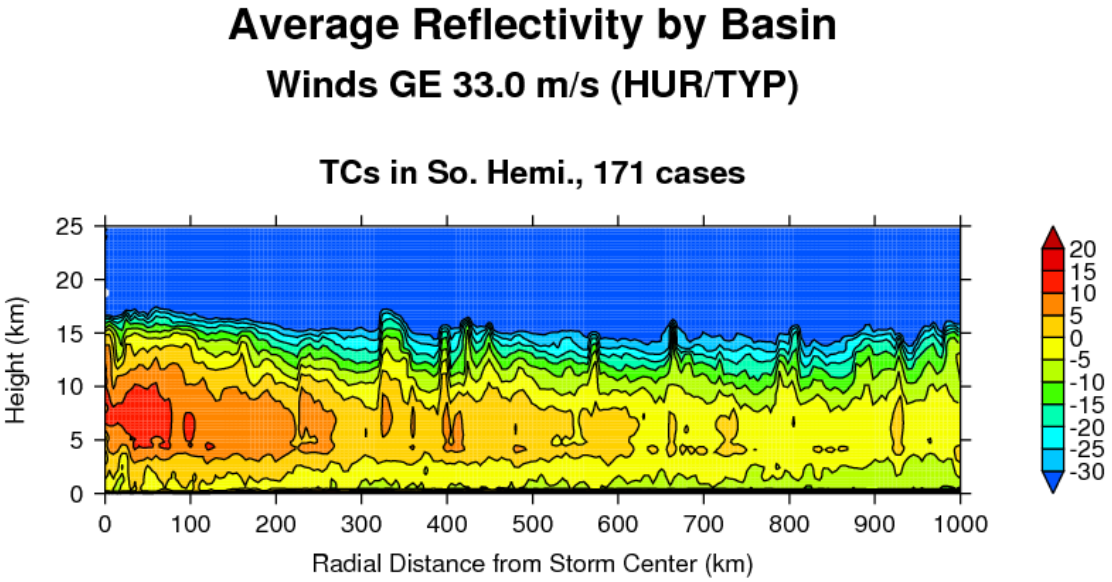

FIGURE 4.5: Average reflectivity by basin (So. Hemisphere and Indian Ocean), winds $\geq$ 33.0 m/s

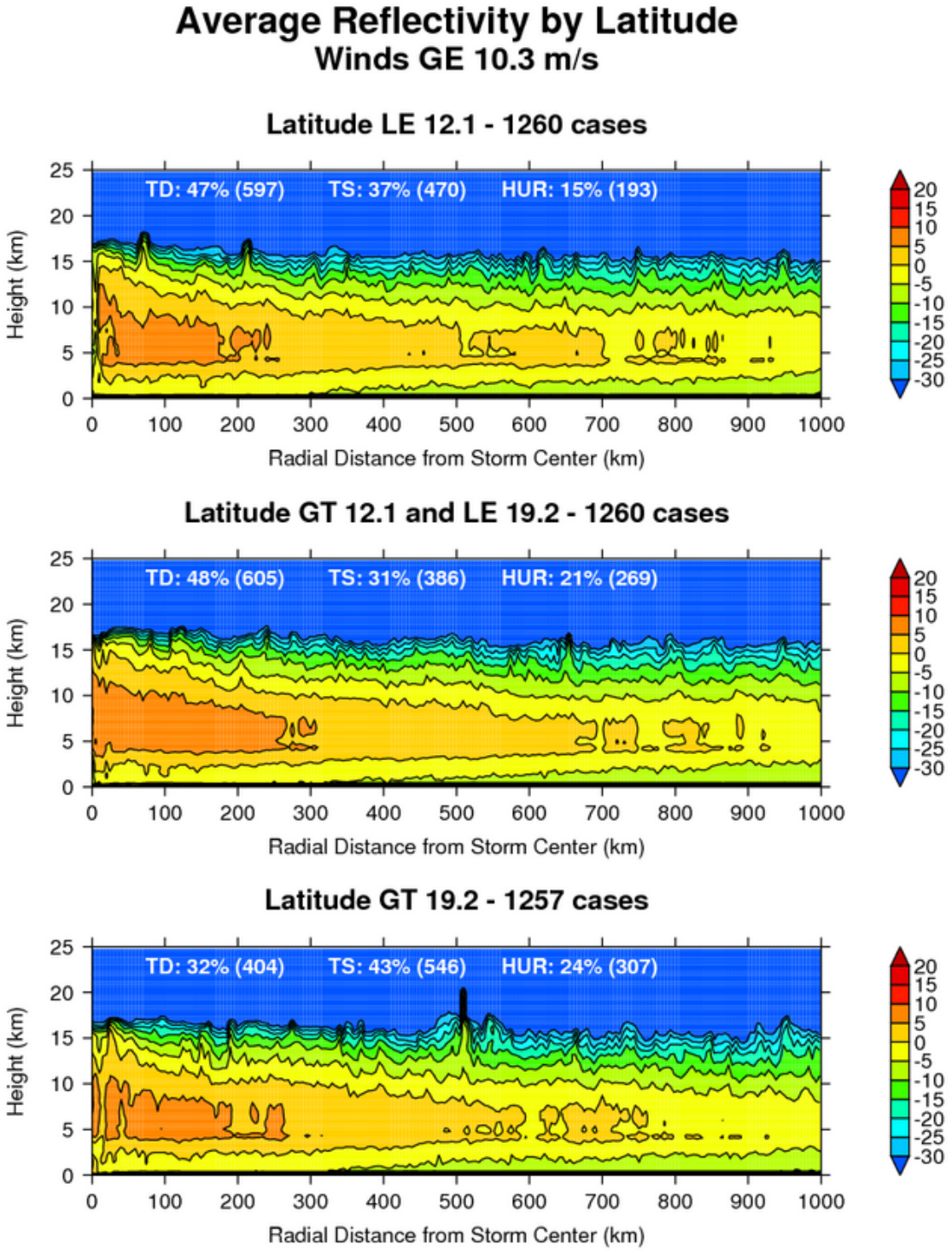

FIGURE 4.6: Average reflectivity by latitude.

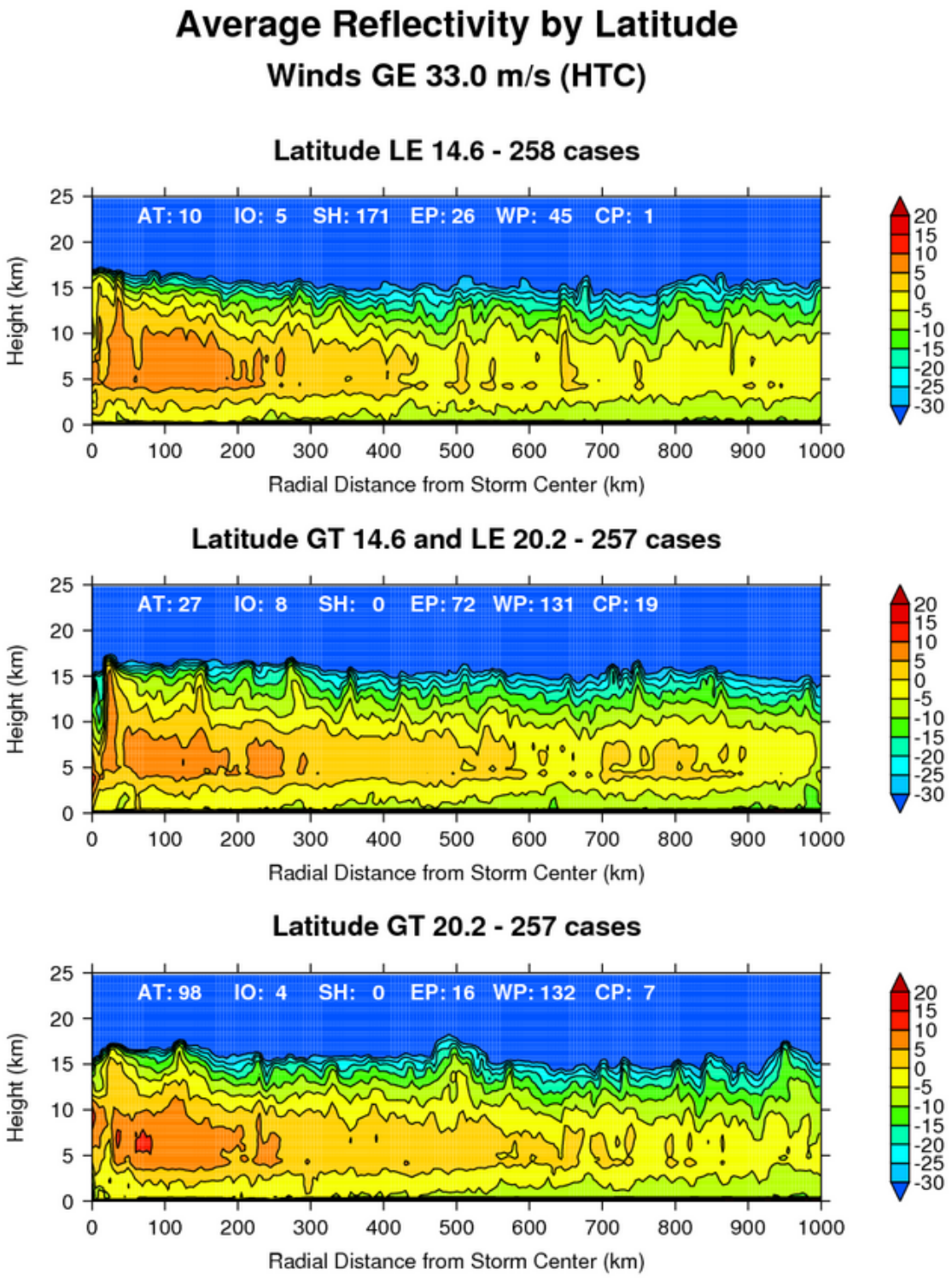

FIGURE 4.7: Average reflectivity by latitude, wind $\geq$ 33.0 m/s

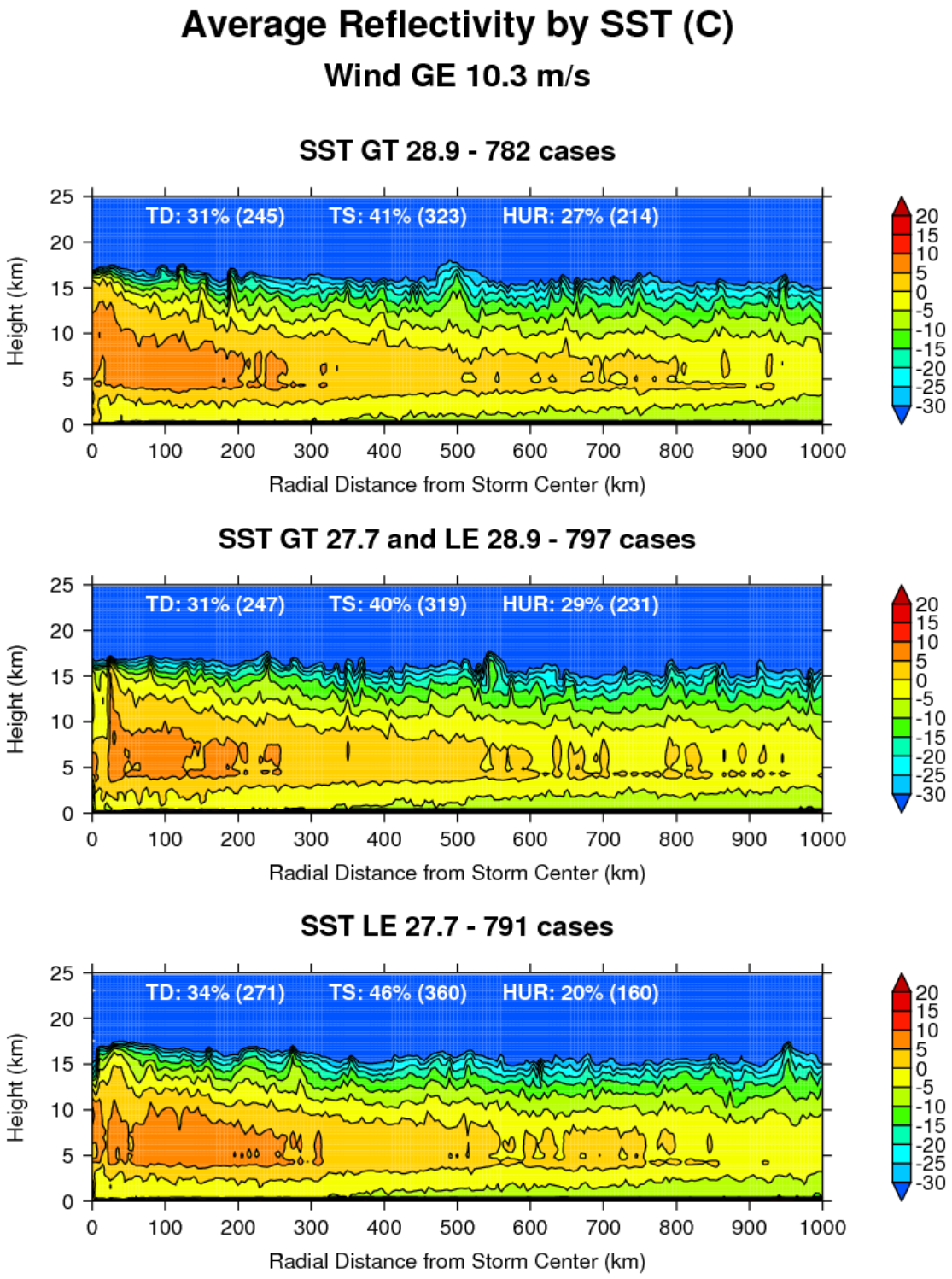

FIGURE 4.8: Average reflectivity by SST - all basins

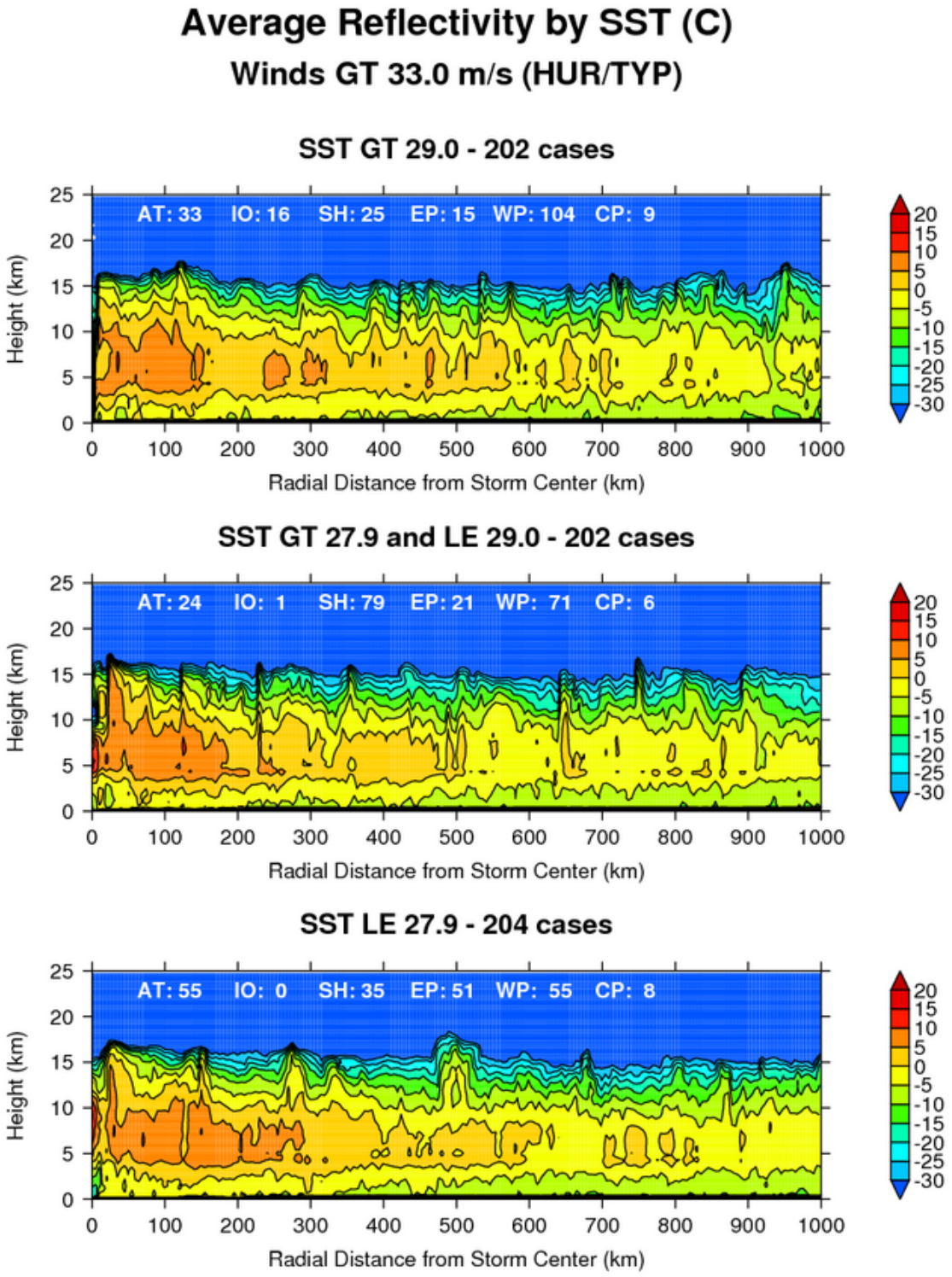

FIGURE 4.9: Average reflectivity by SST - all basins with winds GE 33.0 m/s

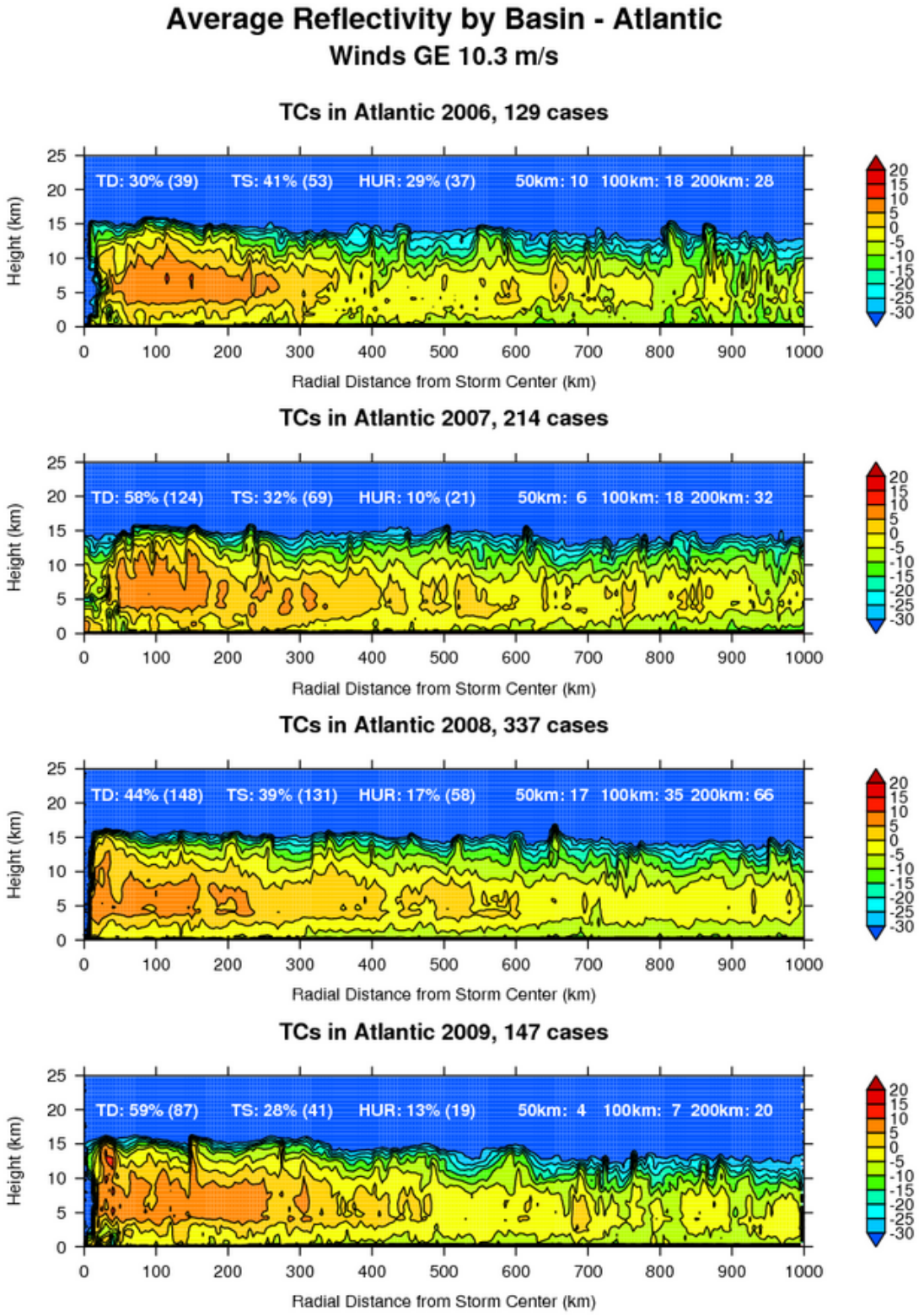

FIGURE 4.10: Average reflectivity by basin and year - Atlantic

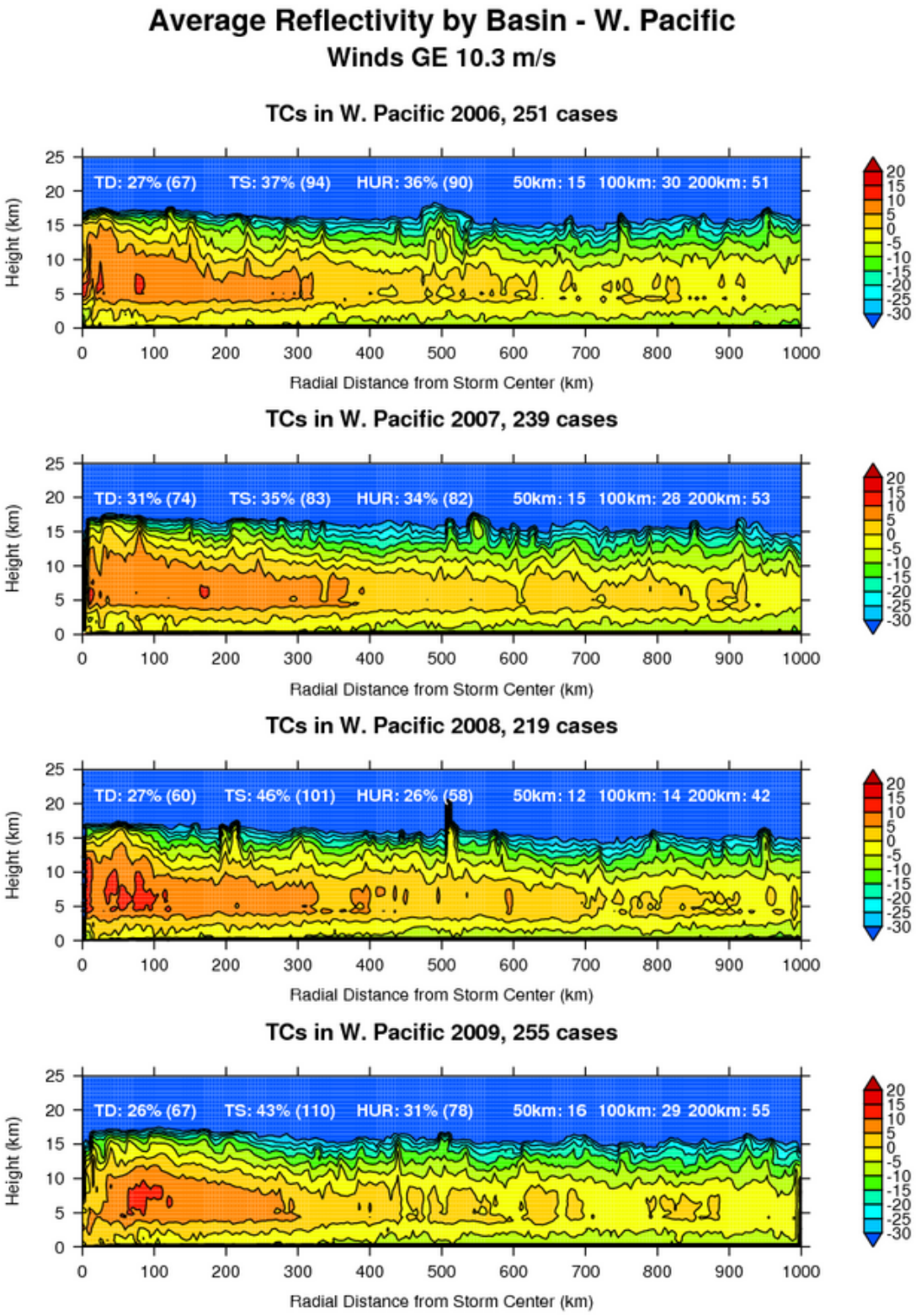

FIGURE 4.11: Average reflectivity by basin and year - W. Pacific

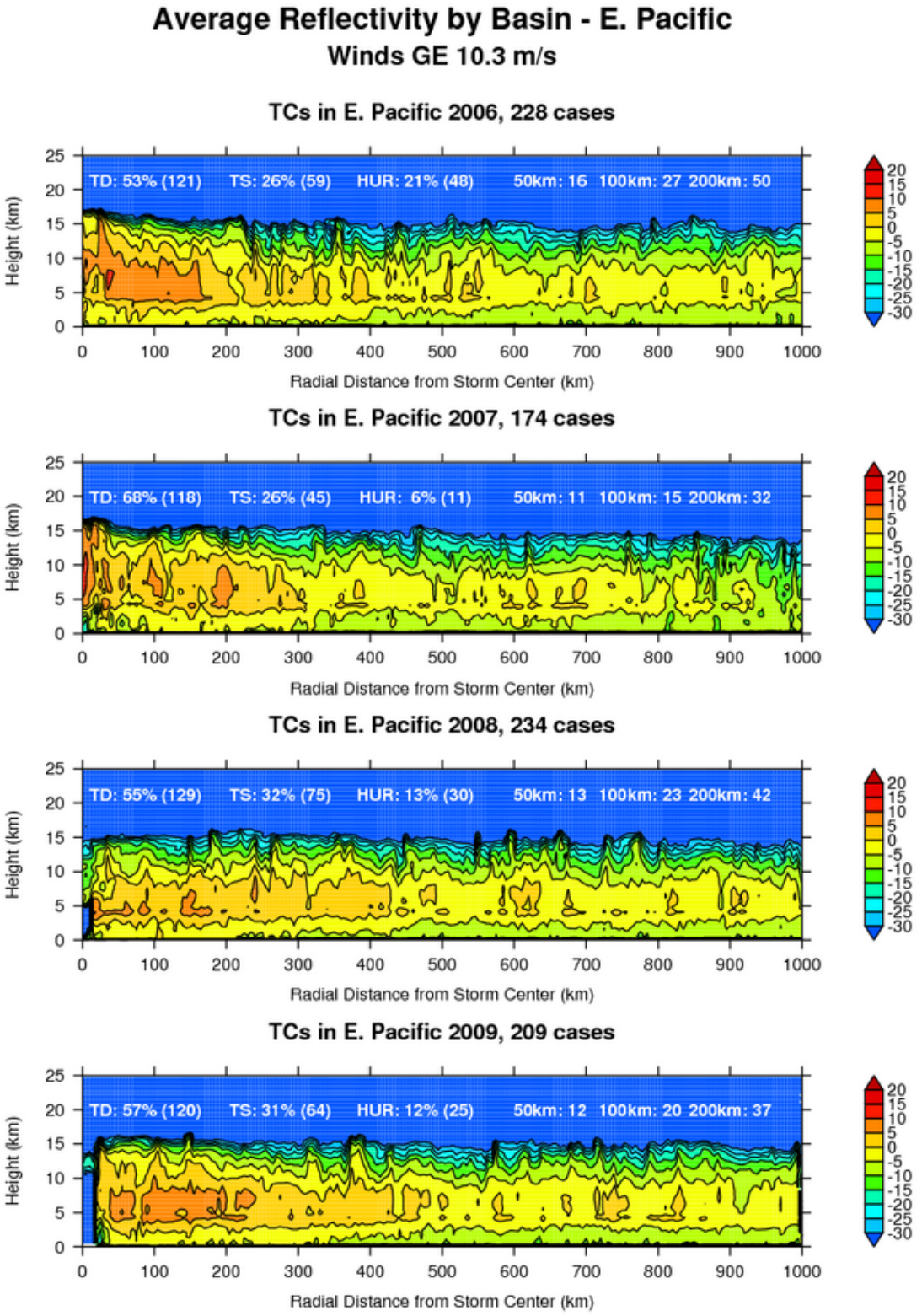

FIGURE 4.12: Average reflectivity by basin and year - E. Pacific

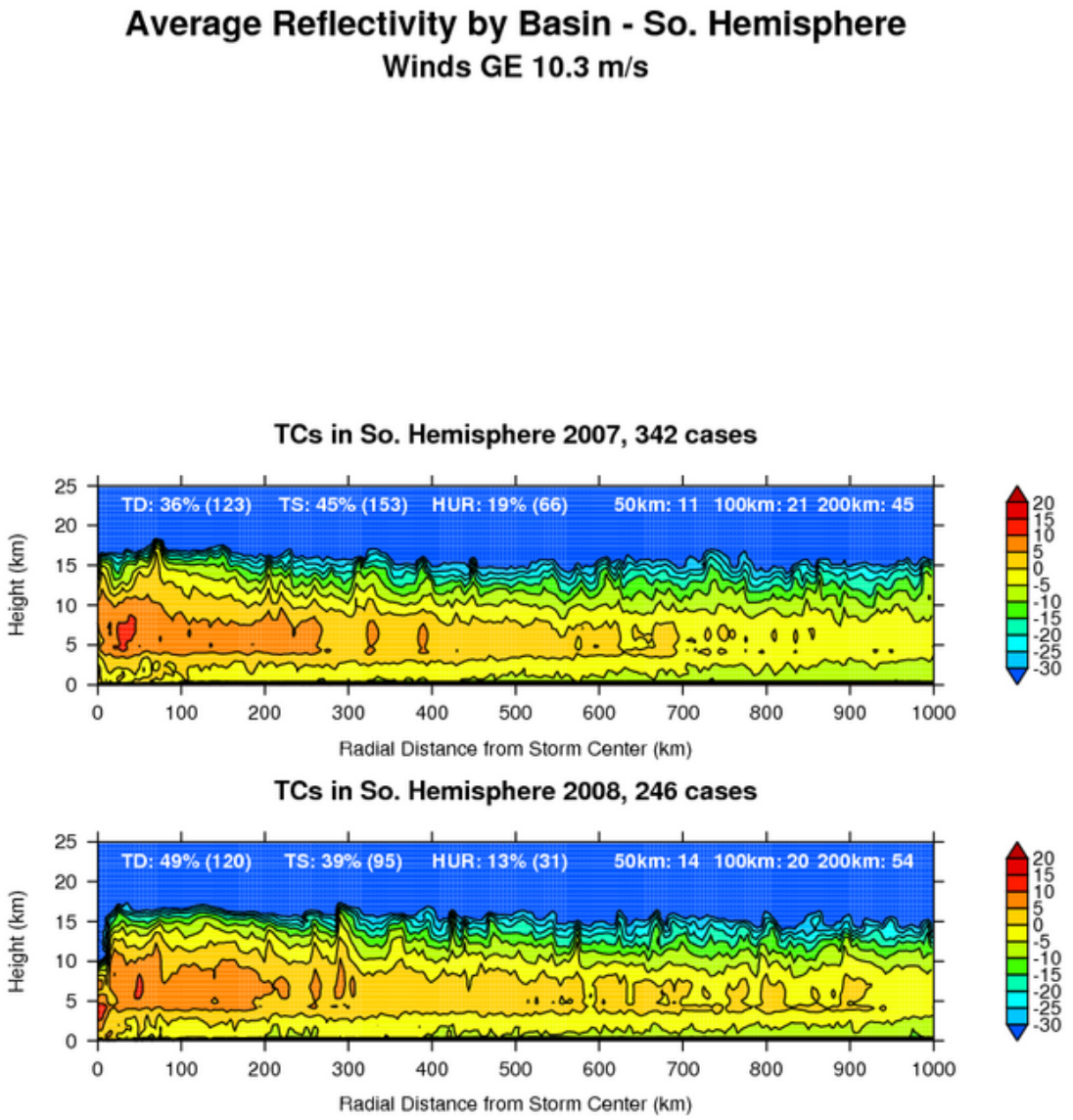

FIGURE 4.13: Average reflectivity by basin and year - So. Hemisphere

4.1.6 Shear

Tropospheric wind shear is defined as the difference of horizontal winds with height (200 mb –850 mb). Wind shear plays a critical role in TC dynamics and formation, large values of wind shear can inhibit cyclone formation by carrying away the heating in the upper troposphere from the lower level circulation thus tearing apart the system and inhibiting further formation ([Gray, 1979]). More recent studies have hypothesized that shear changes the thermal structure of the storm ([DeMaria, 1996]). Variations in the thermal structure (the tilt of the vortex potential vorticity) can affect the convection near the center of storm and change the intensity of the system. When the lower and upper level vortex environments differ, potential vorticity (PV) associated with the system becomes tilted in the vertical. As a result of the tilting PV, the storms midlevel starts to warm which reduces the storms convection activity and further storm development is inhibited. ([Frank and Ritchie, 2001]) used the Mesoscale Model (MM5) to simulate effects of vertical wind shear on TC intensity and evolution. These results show the upper level circulation weakens from the top downward as a consequence of vertical wind shear. [Knaff et al., 2004] used observations from the AMSU to also show vertical wind shear erodes the warm core in the upper levels but details of TC inner core are lacking.

In Figure 4.14, TC's are categorized into three equal number of events of low (< 5.4 m/s), mid (≥ 5.4 m/s and < 9.5 m/s) and high (≥ 9.5 m/s) vertical wind shear. As wind shear increases, CTH's of deeper convection (appearing from the top of the system downwards) decrease. For example in the low shear case, deep convection is found throughout the first 300 km and stretches up to 15 km 30-40 km from storm center. The 0 dBZ contour extends over 15 km in the first 40 km and gradually decreases from storm center. Comparing these contours to the high shear results (> 9.5 m/s), the 5 dBZ hovers below 11 km and only extends outwards 200 km. The highest shear creates a small dip in CTH just inside the storm center but deeper convection becomes limited, especially in mid and high shear results.

In Figure 4.15, shear stratifications are analyzed only for storms of HTC strength for all basins in three equal cases. In low shear regimes ($\leq$ 4.7 m/s) the system remains well intact, a consistent area of 5 dBZ (orange) stretches out to 250 km, an overlaid cirrus eye appears in first 15 km and CTH's gradually decrease with increasing radial distance. As vertical shear increases (mid shear regime) storm structure continues to remain well intact, a larger hint of an eye wall exists but convection appears more broken past 150 km. Further increases in shear ($>$ 8.8 m/s) reveal a substantial decrease in deep convection in the first 50 km with most of it below 10 km in vertical height.

Shear regimes for the ATL, EPAC, WPAC and SHEM basin are presented in Figures 4.16, 4.17, 4.18 and 4.19, respectively. ATL and EPAC basin vertical profile CTH's decrease more rapidly with radial distance than the SHEM or WPAC basin. SHEM systems seem to fare quite well with increasing wind shear as storm structure is optimum with the highest shear values ($>$ 9.8 m/s). WPAC structure is less affected by stronger shear but values between 5.7 and 9.7 m/s produce a more typical mature TC structure.

Generally, increasing shear erodes the top of the deep convective cores, limiting the area available for vertical development. The structure of the eye and eye wall begins to disappear as the system becomes increasingly disorganized. However, shear appears to have a stronger effect on the structure of HTC strength storms.

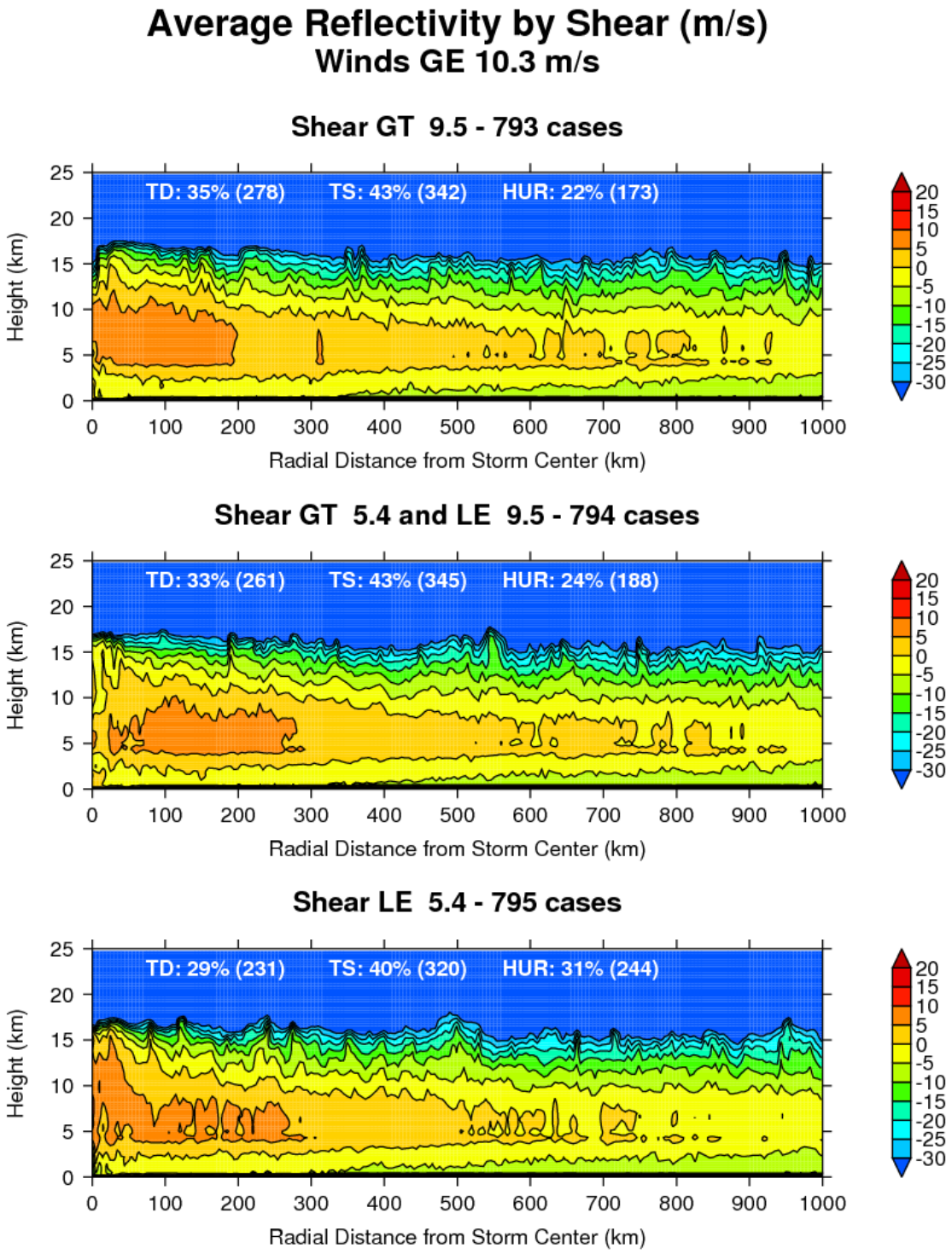

FIGURE 4.14: Average reflectivity by shear (low, mid and high) across all basins with storms of winds GE 10.3 m/s

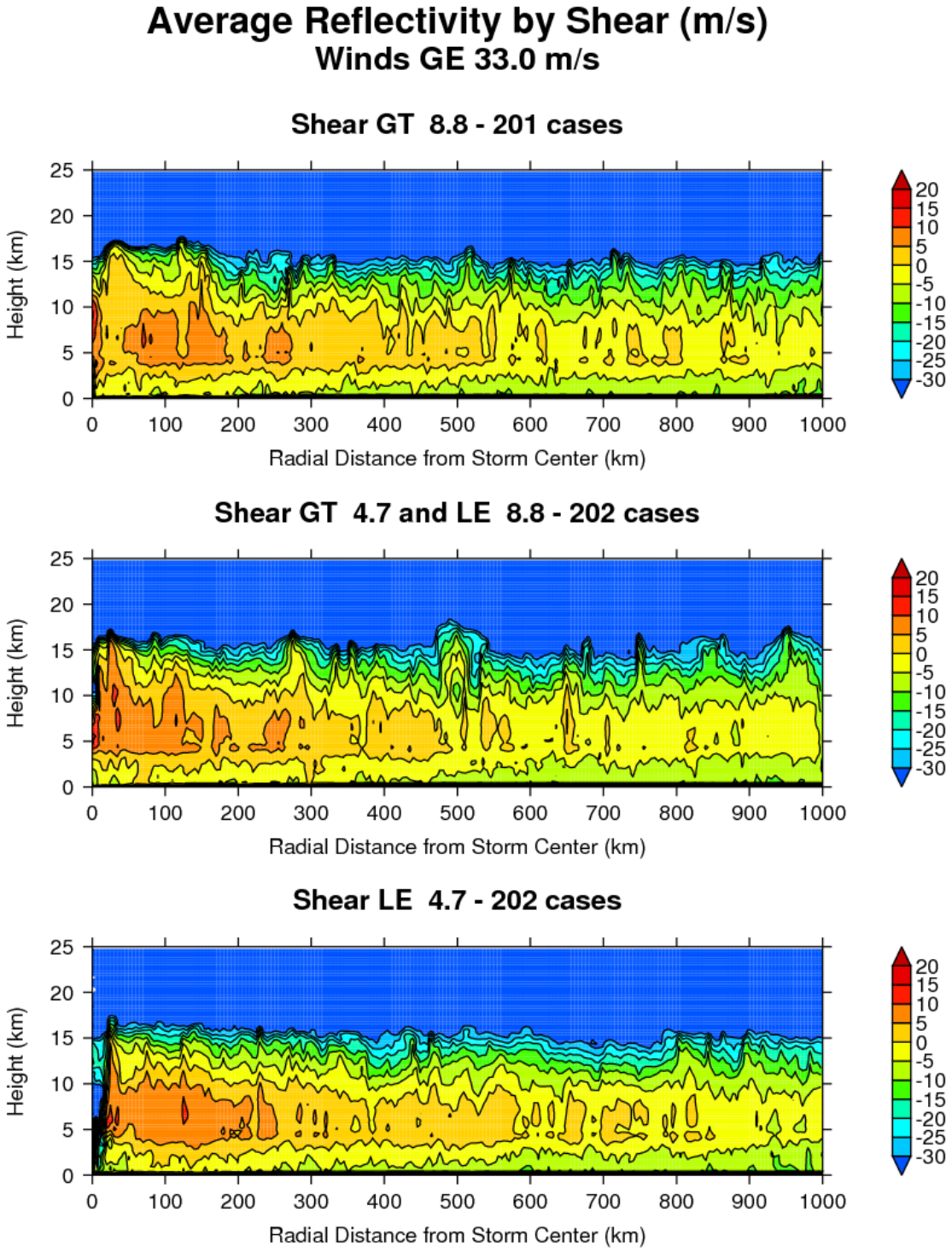

FIGURE 4.15: Average reflectivity of shear by storm strength (HTC).

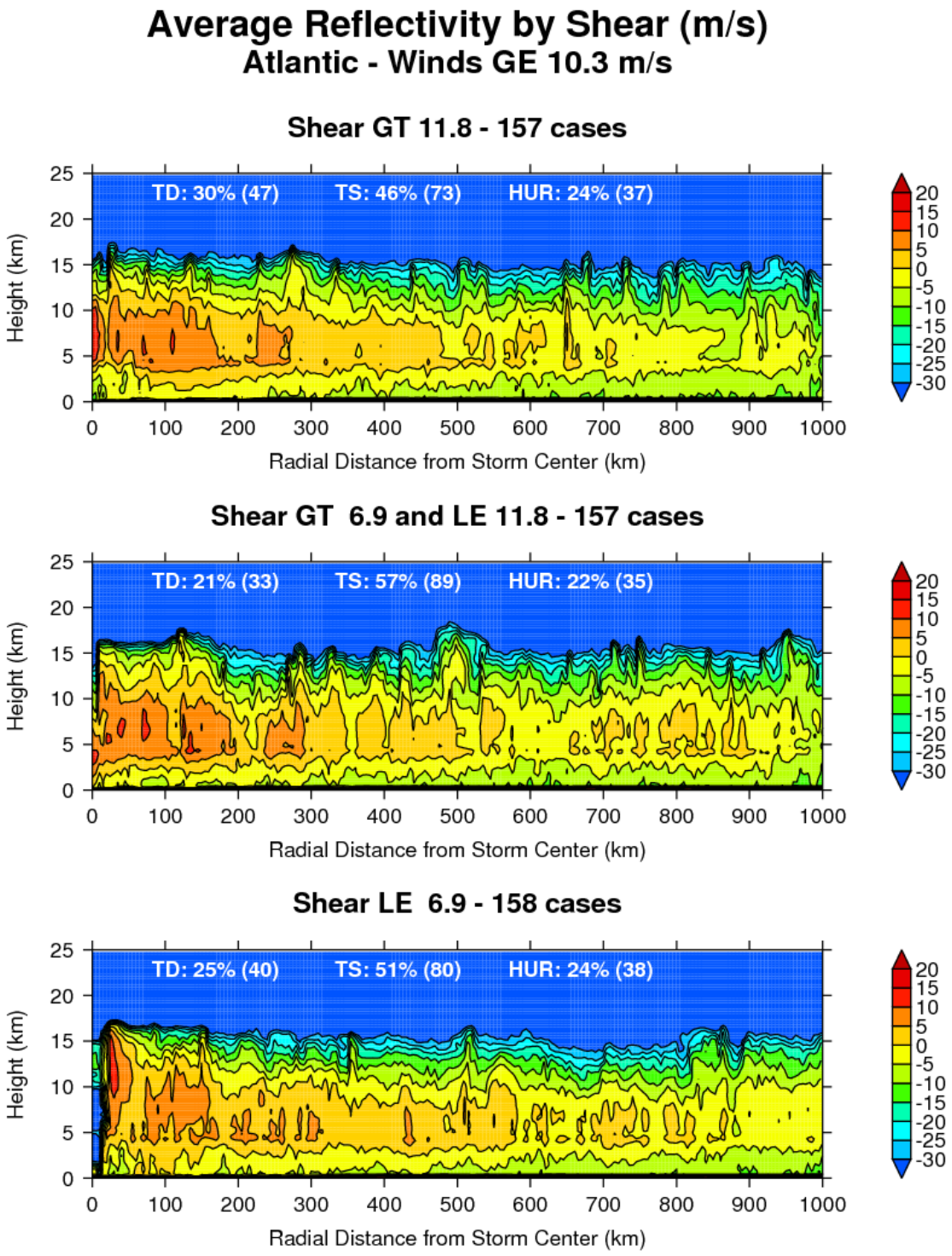

FIGURE 4.16: Average reflectivity of shear by basin - Atlantic

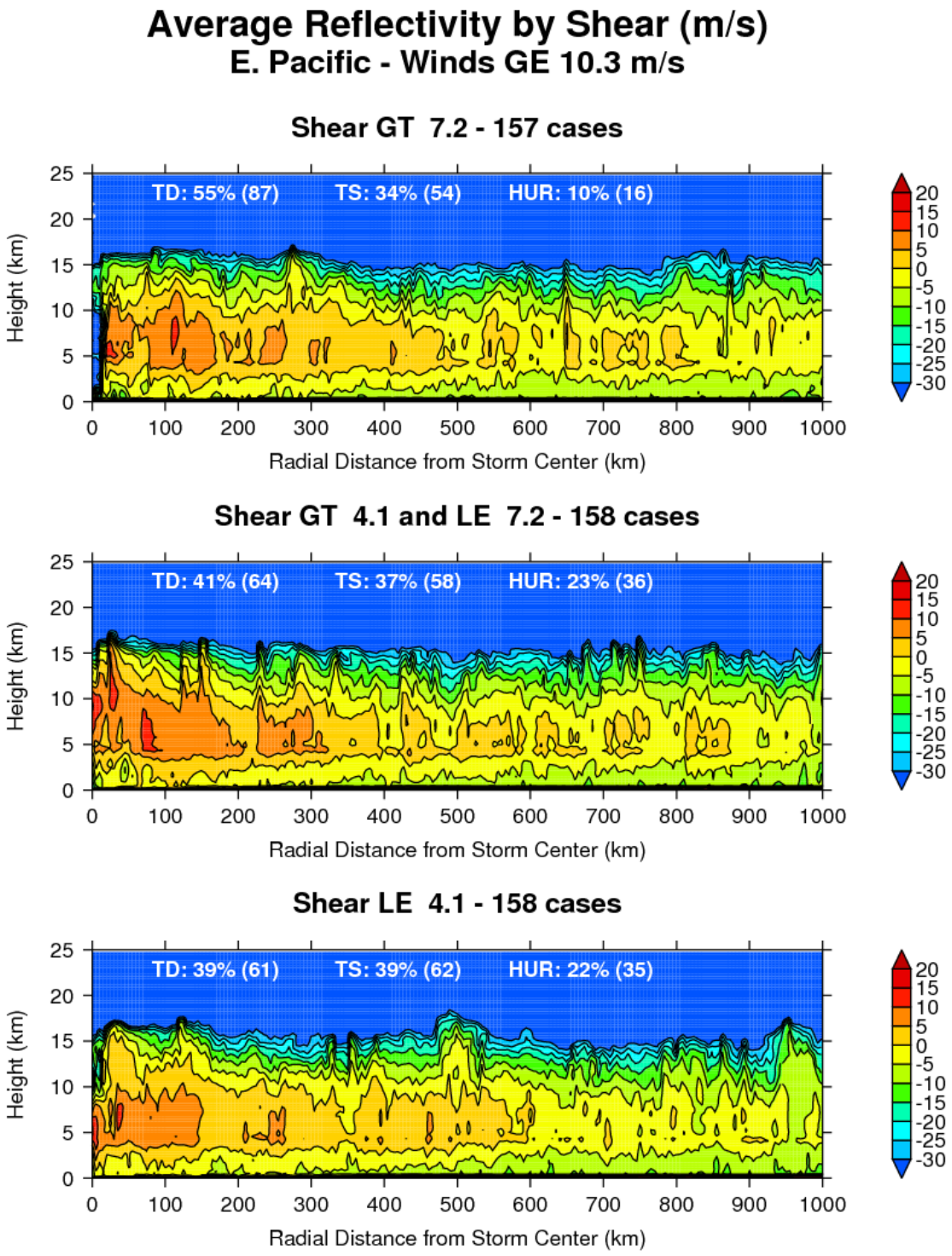

FIGURE 4.17: Average reflectivity of shear by basin - E. Pacific.

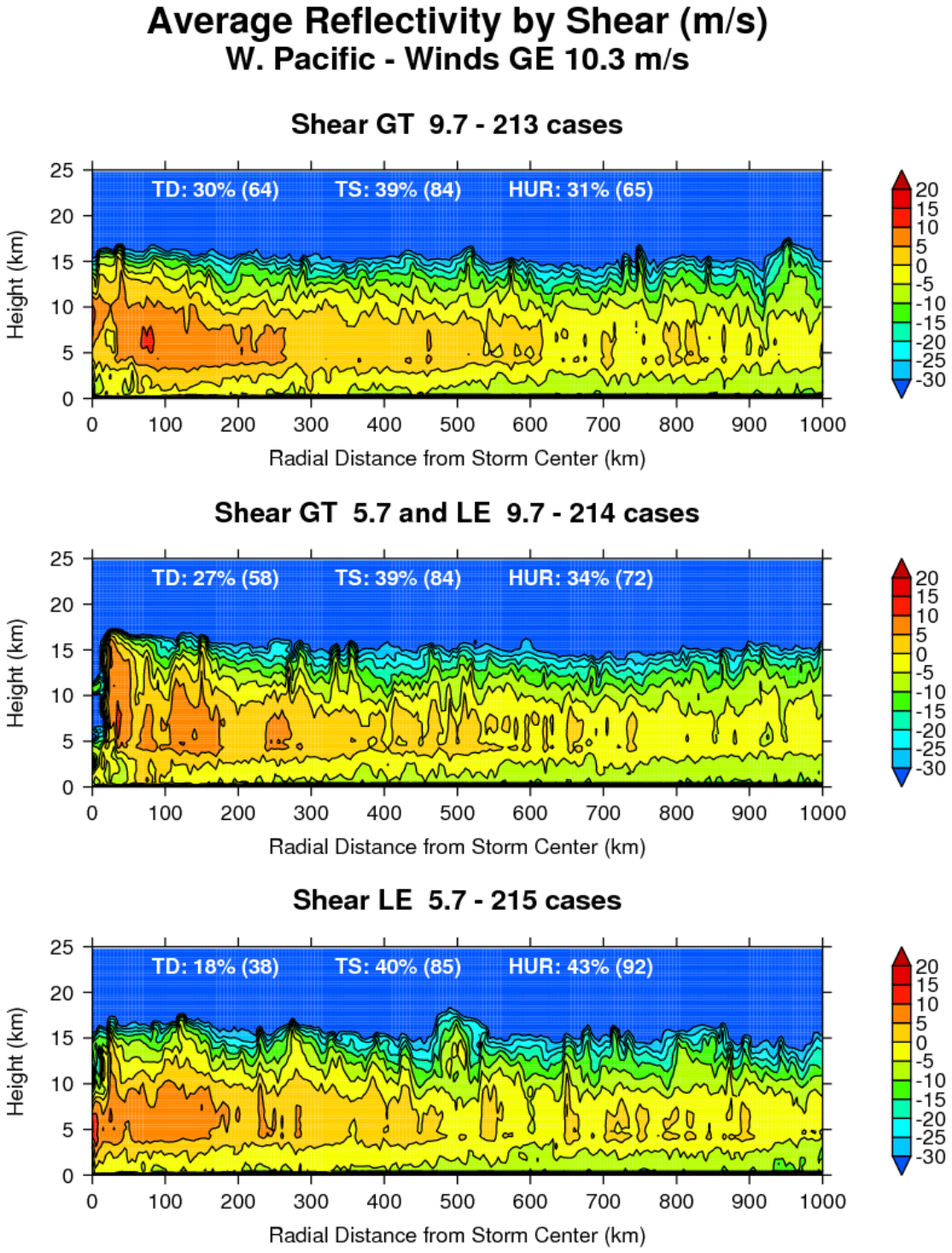

FIGURE 4.18: Average reflectivity of shear by basin - W. Pacific.

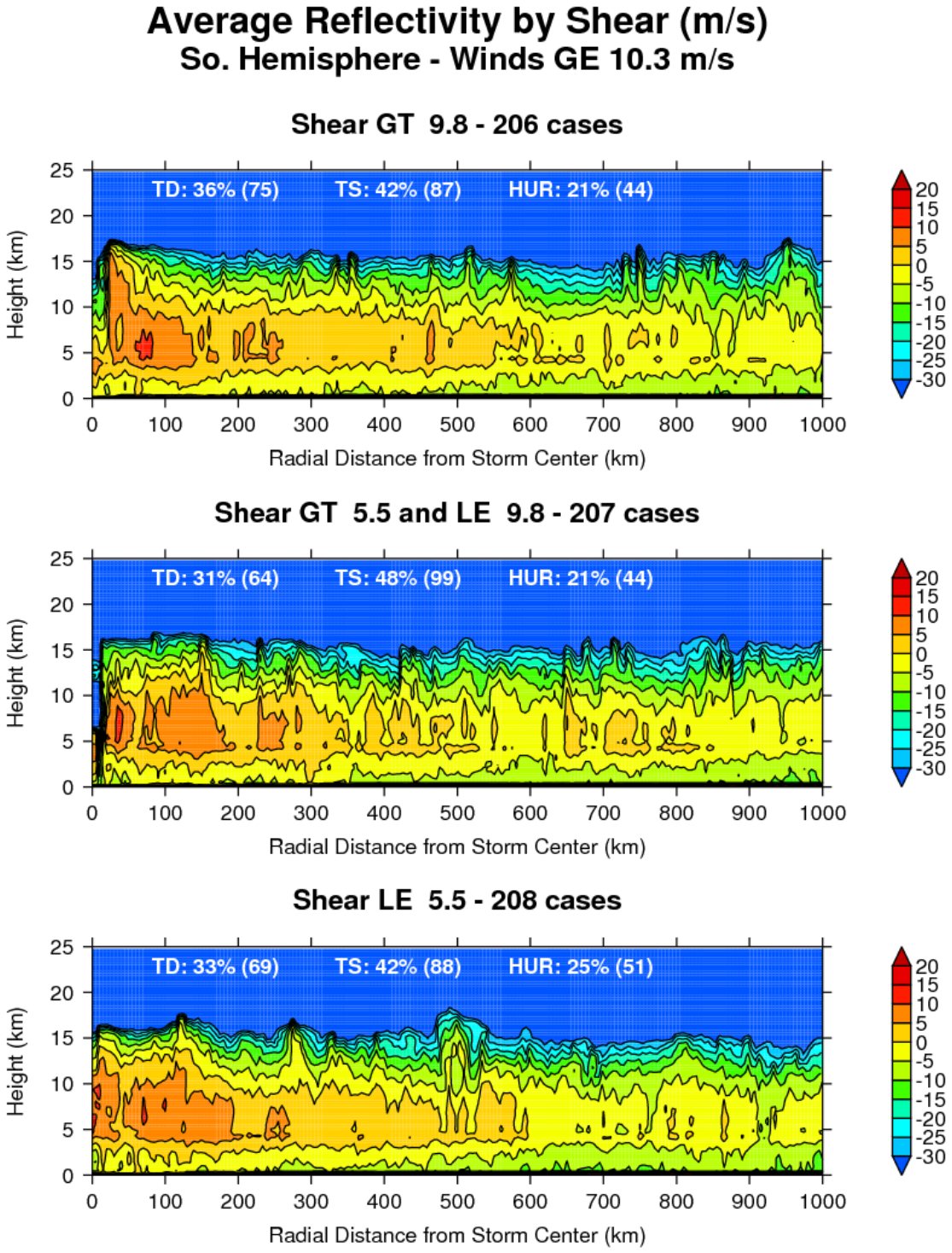

FIGURE 4.19: Average reflectivity of shear by basin - So. Hemisphere.

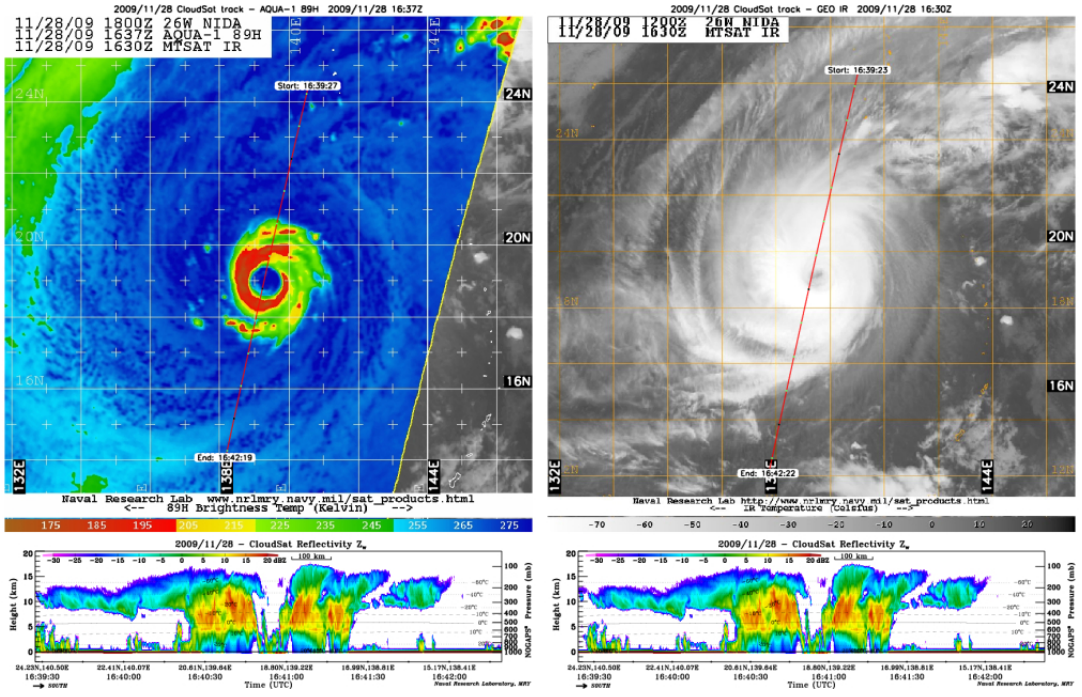

(a) CloudSat overpass of Typhoon Nida - 1640 UTC on November 28, 2009 in the W. Pacific, AMSR-E imagery.

(b) CloudSat overpass of Typhoon Nida - 1640 UTC on November 28, 2009 in the W. Pacific, MODIS imagery.

FIGURE 4.20: CloudSat overpass of Typhoon Nida - 1640 UTC on November 28, 2009 in the W. Pacific.

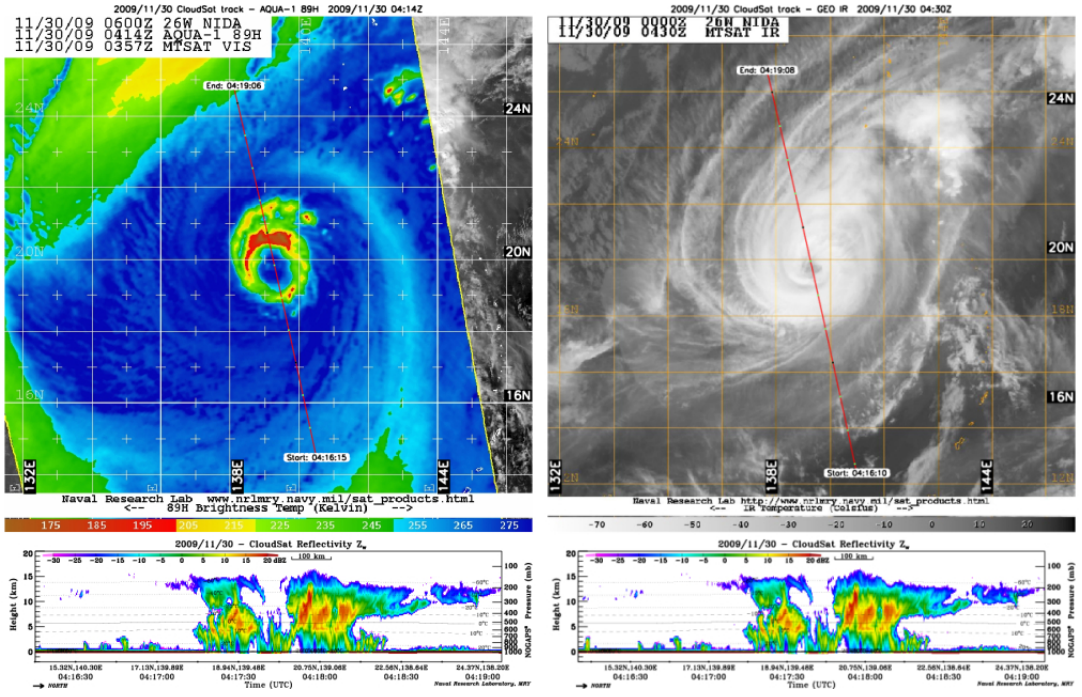

(a) CloudSat overpass of Typhoon Nida - 0420 UTC on November 30, 2009 in the W. Pacific, AMSR-E imagery.

(b) CloudSat overpass of Typhoon Nida - 0420 UTC on November 30, 2009 in the W. Pacific, MODIS imagery.

FIGURE 4.21: CloudSat overpass of Typhoon Nida - 0420 UTC on November 30, 2009 in the W. Pacific.

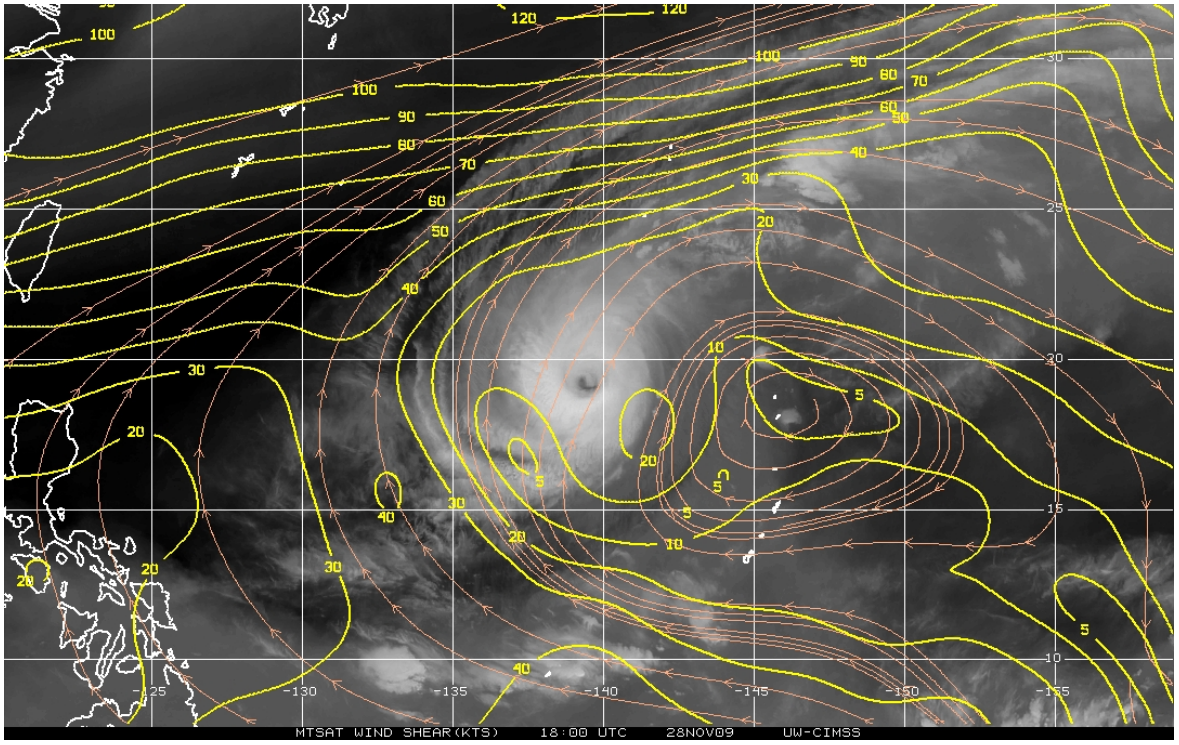

(a) Zoomed in global wind shear (200 - 850 mb) for November 28, 2009. Figure courtesy University of Wisconsin, CIMSS.

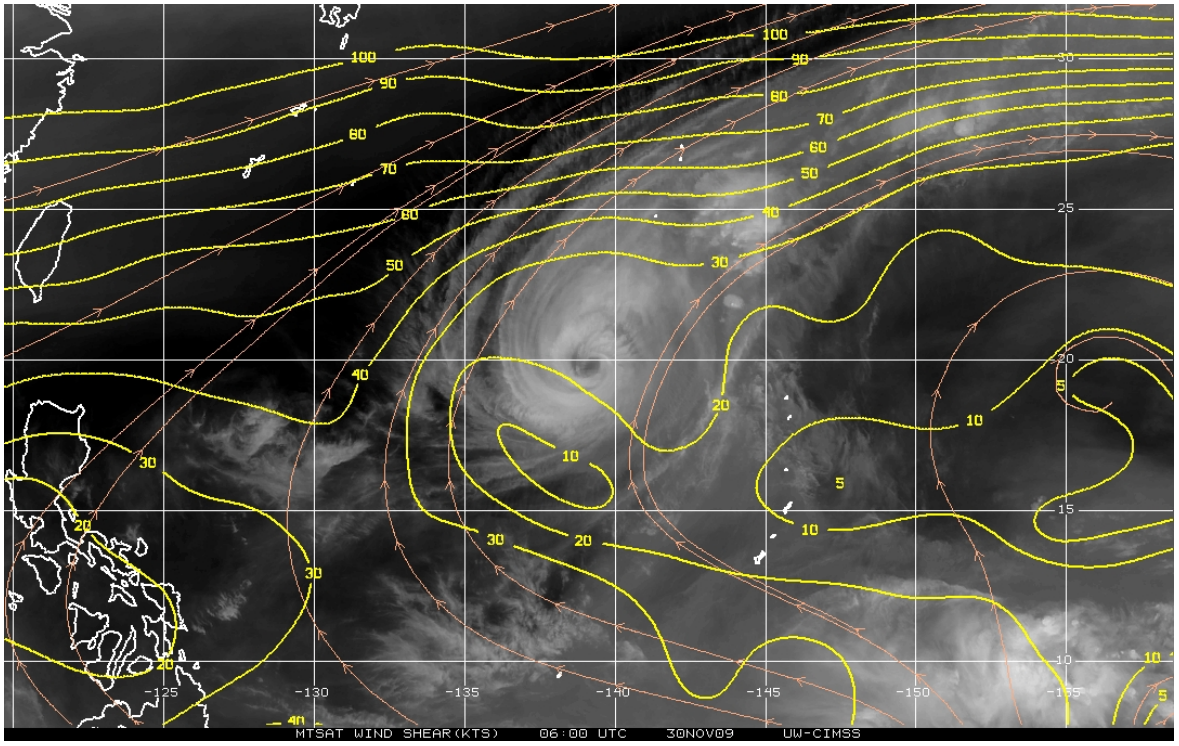

(b) Zoomed in global wind shear (200 - 850 mb) for November 30, 2009. Figure courtesy University of Wisconsin, CIMSS.

FIGURE 4.22: Zoomed in global wind shear (200 - 850 mb) patterns for November 28 and 30, 2009. Figures courtesy University of Wisconsin, CIMSS

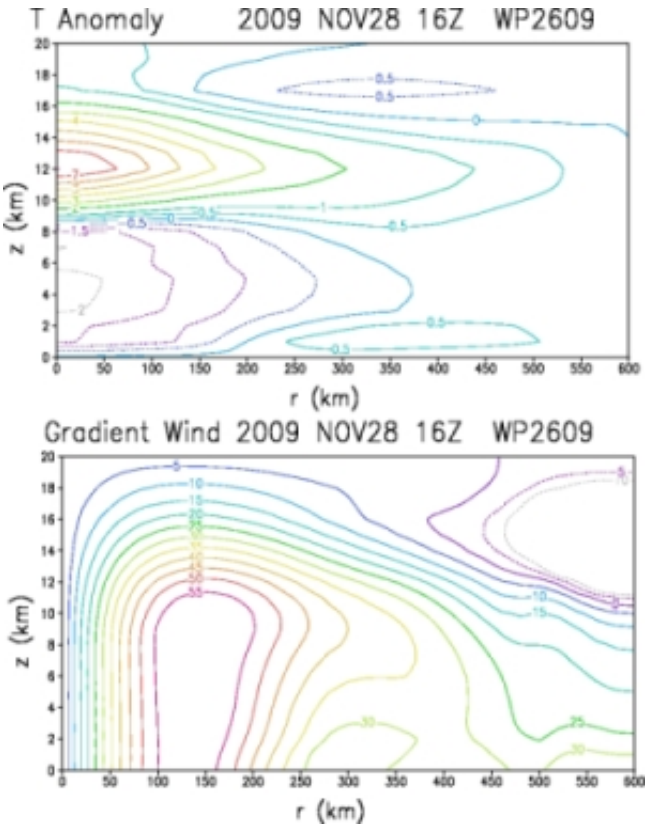

FIGURE 4.23: AMSU plot for Typhoon Nida - 1600 UTC on November 28, 2009 - Temperature anomalies and wind gradient. Figure courtesy of RAMMB.

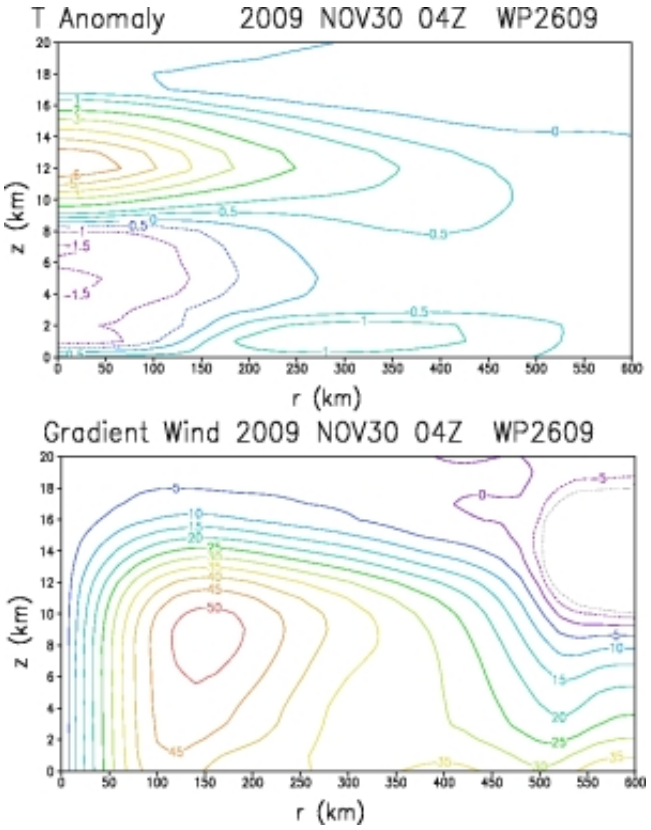

FIGURE 4.24: AMSU plot for Typhoon Nida - 0400 UTC on November 30, 2009 - Temperature anomalies and wind gradient. Figure courtesy of RAMMB

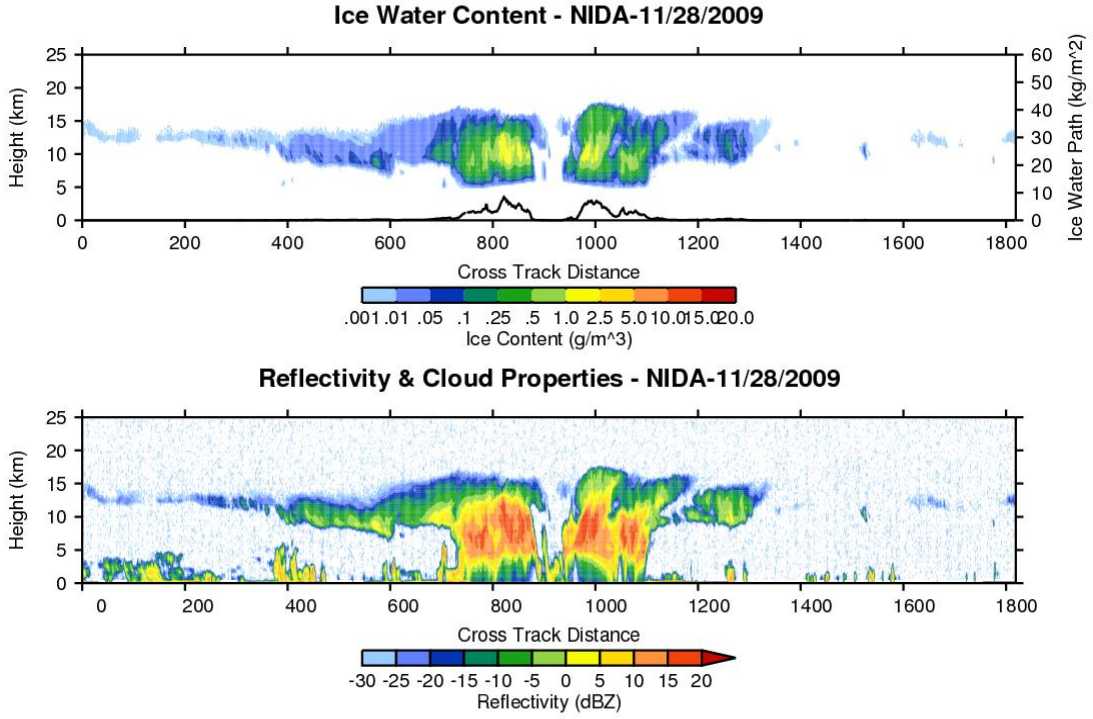

FIGURE 4.25: CS reflectivity and IWC for Typhoon Nida on November 28, 2009.

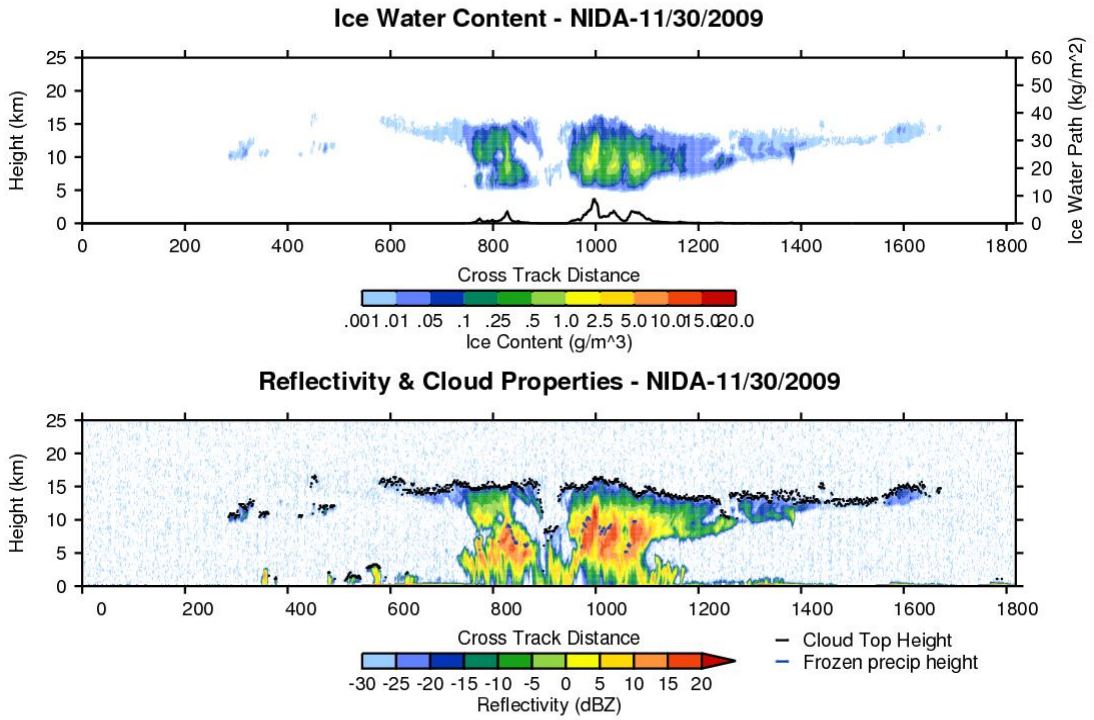

FIGURE 4.26: CS reflectivity and IWC, MODIS CTH and frozen precipitation height for Typhoon Nida on November 30, 2009.

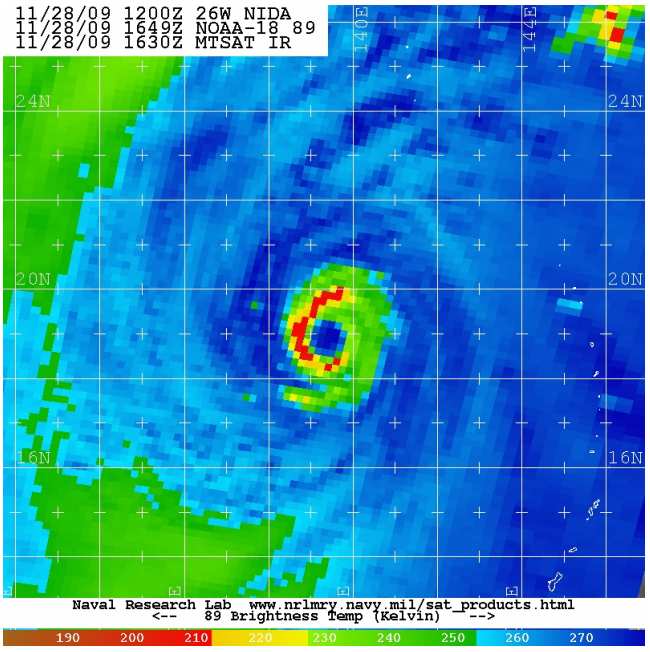

FIGURE 4.27

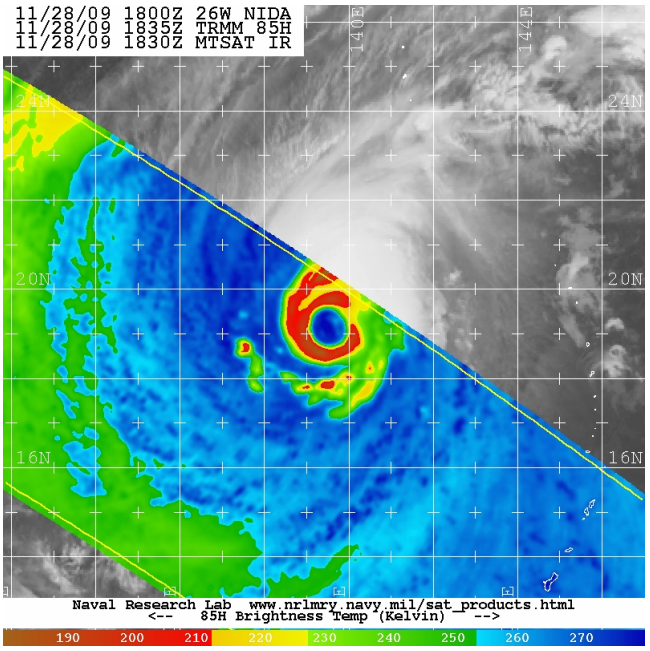

FIGURE 4.28: TRMM TMI 85 GHz overpass

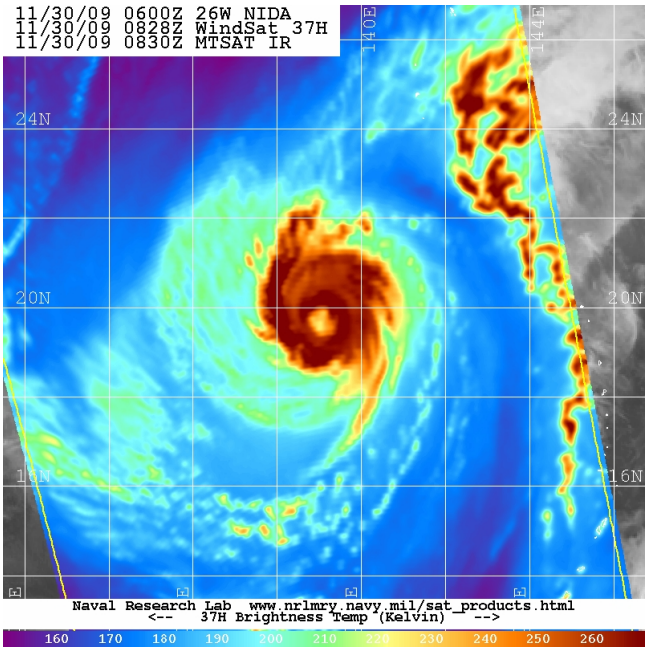

FIGURE 4.29: WindSat 37 GHz overpass of Typhoon Nida on November 30, 2009.

4.2 Shear effect on a mature TC

The following case study examines two CS overpasses over the eye of a mature TC (winds $\geq$ 33.0 m/s) as the storm is starting to weaken. This is one of a few cases where CS completed consecutive eye overpasses of a mature TC within 32 hours of each other. The first overpass of Typhoon Nida on November 28, 2009 at 1640 UTC (66.9 m/s maximum winds) traversed the system from the NE to SW in the WPAC. The system just started to weaken after attaining super-typhoon status (Figure 4.20). The CS overpass reveals the system is symmetric, eyewall extending outwards and away from the storm center and a slight cirrus overlay with stratocumulus near the surface of the eye. The inner eyewall is weakening as the secondary eye wall is moving inwards. AMSR-E (Figure 4.20(a)) imagery clearly shows the partial concentric red circle of the secondary eye wall.

Figure 4.23 shows AMSU radius vs. height cross sections of anomalies for the same time period, warm temperature anomalies are clearly located in the upper troposphere consistent with the structure of a typical mature TC. AMSU average temperature and wind profiles contain smoothed profiles which can result in unrealistically low wind speeds and are typically accurate for storms with maximum winds of less than 90 knots. AMSU profiles are useful for determining the general thermal structure of a TC and measurements inside the eyewall are less accurate as horizontal resolution is low. IWC (Figure 4.25) is slightly higher on the northern side of the storm, the IWP profiles are similar on either sides of the eye wall. The southern side of the storm has higher overall CTH (over 16 km) but the beginning of deeper convection (orange reflectivity) begins below 13 km. Moderate shear is from the south at 13 knots (6.7 m/s). NOAA-18 89 GHz overpasses also reveals the low BT's and secondary eyewall ring (Figure 4.27). TRMM overpassed a portion of the storm a little over two hours later showing the eyewall nearly filled in (Figure 4.28). The storm was moving very slowly to the E-NE entering an area of decreased OHC and SST's. The forecast for Nida called for gradual weakening as the storm moved into unfavorable environmental conditions with steady amounts of shear.

The second eye overpass of the system occurred 32 hours later on November 30, 2009 at 0415 UTC. The storm is considerably weaker (maximum winds 51.4 m/s), the red eye wall ring is confined to the northern section and the system has entered an area of drier air. Moderate shear (between 10-20 knots) continued for the entire time period from the S-SW. The eye is elongated in a slight NW-SE position and is very ragged (Figure 4.21), convective cores on either side of the eye have weakened considerably and decreased in size, especially on the southern edge. AMSU radius-height cross section analysis (Figure 4.24) reveals the erosion of the warm core anomaly, the vortex has become shallower and decreased in size and magnitude. IWC has diminished on southern edge while the northern side IWC still remains although it is broken into three groups matching the convective core areas. Convective cores are nearly non-existent on the southern side (under 10 km). WindSat (Figure 4.29, four hours after the CS overpass) shows portions S and W of the system have diminished in size with deep convection cores almost completely non-existent.

4.3 Zero and Ten dBZ reflectivity heights

The height of the reflectivity of zero and ten dBZ are effective for tracing precipitation sized particles ([Stephens and Wood, 2007]). Deeper convection will loft precipitation particles higher into the atmosphere than lighter convection. To compute the height of each zero dBZ and ten dBZ profile, each CS vertical cross sectional point is analyzed from the top of the atmosphere downwards for storms with winds of at least 10.3 m/s. The height bin containing the corresponding reflectivity value of zero dBZ (or ten dBZ) was then collected. Profiles that did not contain a value meeting these thresholds were excluded from the analysis. IO basin results are not added in the following analyses as the number of overpasses (245) was not enough to provide a quantitative analysis.

FIGURE 4.30: Average zero km dBZ values for all storms with winds $\geq$ 10.3 m/s.

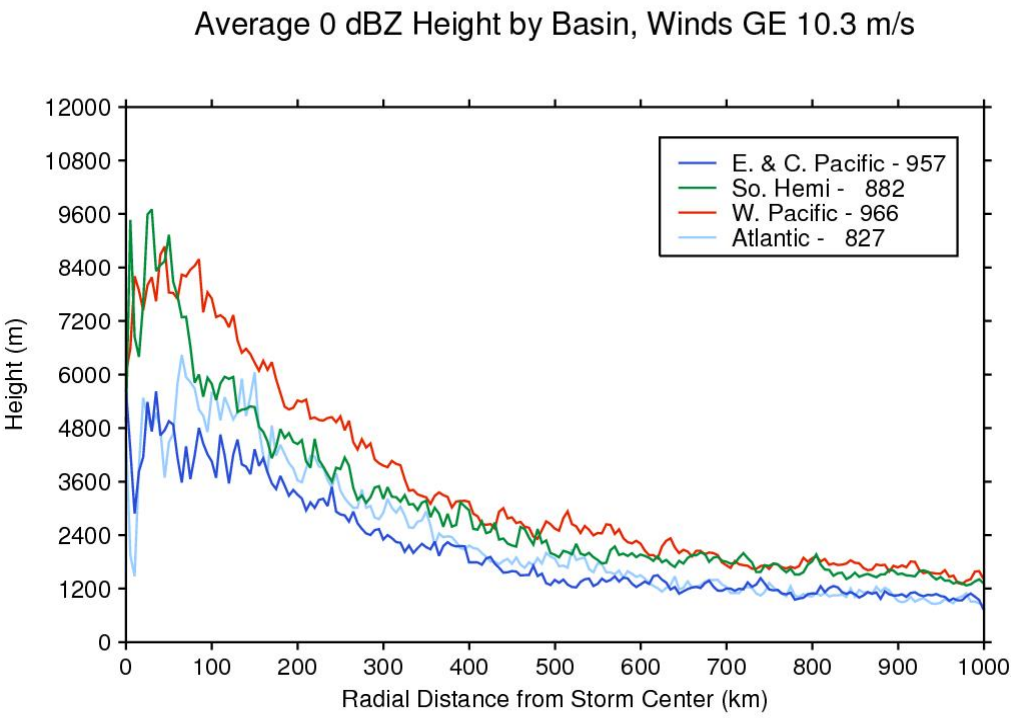

The results reveal WPAC basin areas generally have the greatest zero and ten dBZ heights (Figures 4.30 and 4.31). WPAC storms have the benefit of a much longer season due to the persistent warm pool waters in the area and a higher tropopause as well. Mean annual SST's in the area range from 28° C to 29.5° C. Because of the high SSTs, a large area of heat and water vapor transfer in the form of latent heating is available for storm formation. SHEM basin heights are quite similar to heights in the WPAC. This could be due to the fact of the large basin area (covering everything south of the equator) but it also shows SHEM TC's loft the same sized precipitation particles just as high as WPAC storms. The number of TC overpasses is almost the same (~1200) in each basin. The ATL basin followed with heights less than the WPAC and SHEM storms while the EPAC rounded out the bottom. The EPAC basin generally has the coolest water and smaller storm size as discussed previously. The overall trend of heights for both zero and ten dBZ are similar, both have higher heights near the storm center decreasing with radial distance.

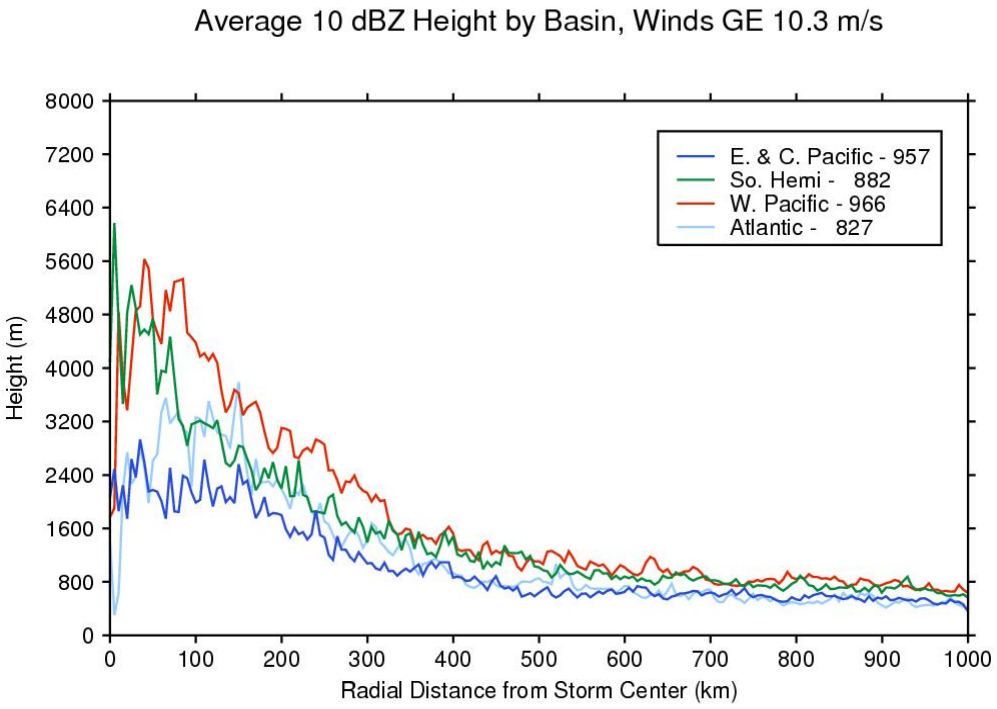

FIGURE 4.31: Average ten km dBZ values for all storms with winds $\geq$ 10.3 m/s.

4.4 Average 10 km Reflectivity

The average reflectivity at a predefined vertical height is shown in Figure 4.32 for storms with winds of 10.3 m/s and for HTC strength storms in Figure 4.33. This analysis is useful in showing the size of particles that are lofted into the atmosphere at ten km across different basins. Larger reflectivity values indicate larger sized particles and the presence of deep convection and stronger updrafts. At the ten km height, the WPAC region has the highest reflectivity followed closely by the SHEM, similar to results of the zero and ten dBZ heights. The ATL and EPAC follow a couple dBZ's behind these basins. For storms with winds over 33.0 m/s, the same trend emerges with WPAC storms the highest.

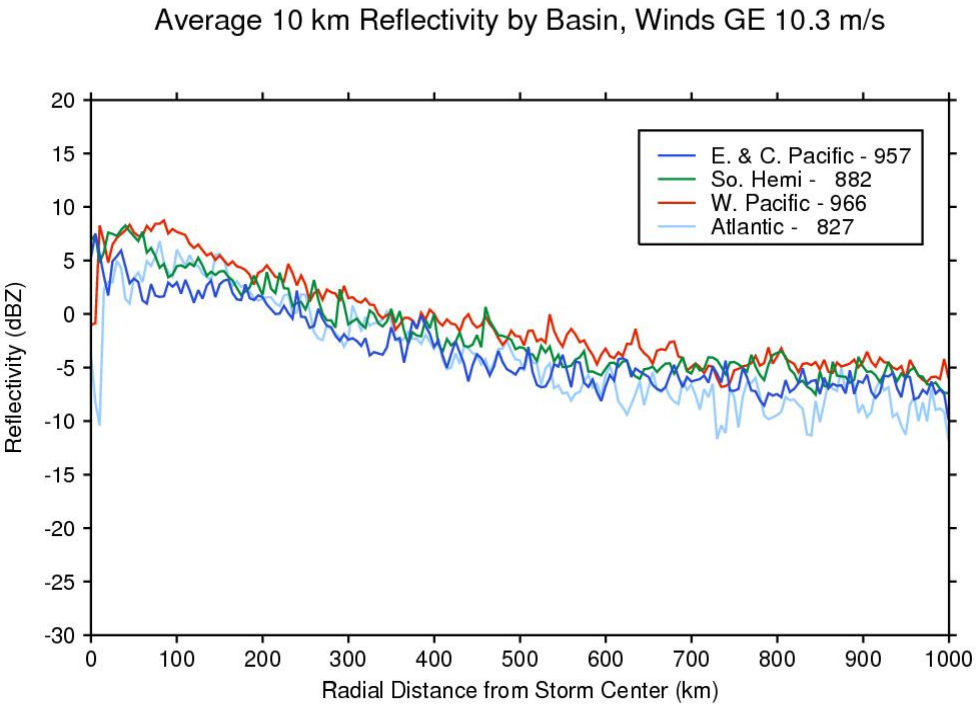

FIGURE 4.32: Average 10 km reflectivity for all storms with winds $\geq$ 10.3 m/s

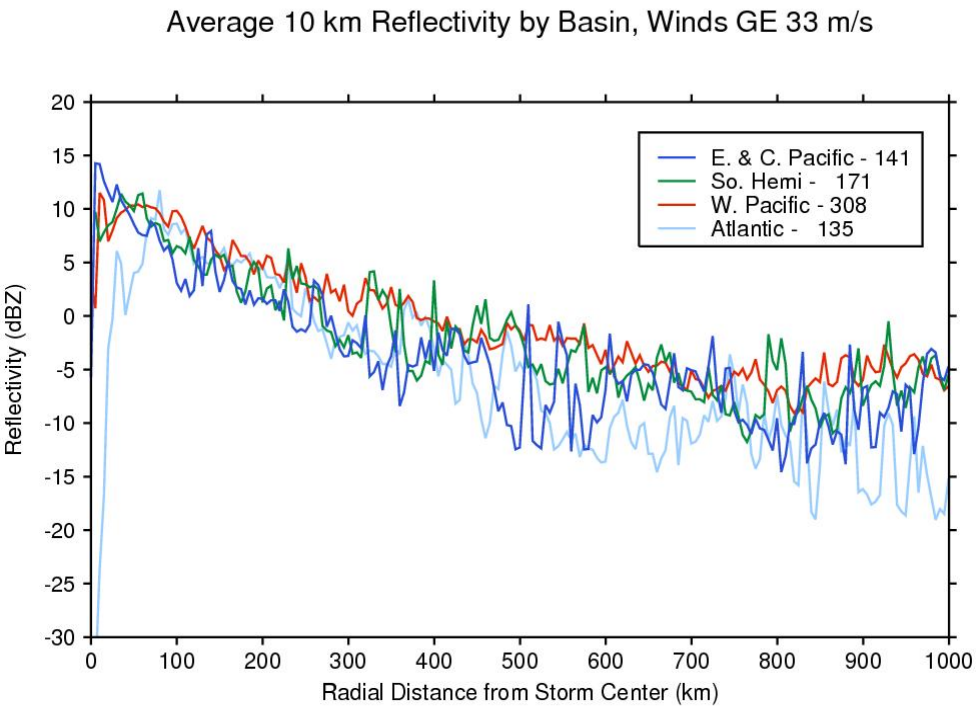

FIGURE 4.33: Average 10 km reflectivity for all storms with $\geq$ 33.0 m/s

Chapter 5

Conclusions and Future Work

5.1 Analysis of Results

The research activity conducted focused on the creation of a unique database for studying the cloud properties and precipitation of TC's. The CS TC database is a first of its kind dataset combining satellite observations and model data of global TC systems. The database provides detailed information on vertical cloud layers, precipitation structure, cloud properties, environmental storm conditions and best track data of global TC's. These observations and measurements provide an additional data source for validation of passive radiometers and numerical models along with first time satellite observations of the inner vertical details of TC's. The CS TC database thus can establish an important new framework for studying TC's where other passive and active sensors are not as sensitive to identification of these details. CS profiles reveal the finer cloud details beneath the cirrus layer. For example, light to heavy precipitation cores, eye structure, hot towers, upper troposphere features, bright band layers, CTH and moat areas are all exposed with CS observations. No other satellite sensor has the capability to produce such fine storm details.

The results of stratifications of reflectivity confirm previously known features about TC's as well as new insights. Compositing reflectivity profiles reveals,

i) increased areas of reflectivity (both horizontally and vertically) occur with increasing SST although overall CTH remains the same. This suggests that the area of active convection also increases with increasing SST. The vertical structure of TC's varies across basin, WPAC storms tend to have larger, deeper convective areas whereas EPAC storms contain smaller areas of deeper convection. Initial results from a small sample of storms from the IO basin reveal vertical structure that is it quite similar to WPAC TC's with some areas containing greater CTH's and reflectivity values with averaging.

ii) Across all basins, CTH remains fairly consistent at 15-16 km. Lower latitude storms contain smaller reflectivity profiles than higher latitude storms. Higher latitude storms contain deep convection further from the storm center.

iii) Wind shear exerts an important influence on the TC structure. Mature HTC strength storms are more susceptible to the influence of stronger vertical wind shear than weaker TD or TS strength storms. Stratifications of TC's in varying shear regimes reveal shear that erodes the overall CTH and limits the number of deep convective cores. In an example case from Typhoon Nida, mid-level shear cuts through the TC breaking apart precipitation cores, decreasing the warm core anomaly and eroding overall CTH.

iv) Year to year variations of reflectivity are dependent upon the number of eye and intense HTC strength overpasses. Annual SST variations influenced mostly by ENSO phase, play a role in average reflectivity across each basin, influencing the CTH and depth of reflectivity from the storm center. Heights of the average zero and ten dBZ threshold confirm WPAC storms loft precipitation-sized particles higher with SHEM storms very similar in height.

5.2 Future Work

Numerous opportunities for future analysis with the CS TC dataset are available. As CS continues to orbit, data will continue to be collected expanding the database and providing more case studies for analysis. Further analysis of vertical wind shear across multiple overpasses of TC's could also increase the understanding on how shear plays a role in the vertical degradation (in some cases intensification) of TC systems. Case studies of IWC in varying shear regimes will also show more clearly how the upper level of the storm system changes with storm strength.

Comparisons of TRMM and CS observations will provide a unique opportunity to analyze heavy and light precipitation in TC's and the combination of these observations can provide a nearly complete view of vertical structure. CS defines the finer cloud structure, heavy precipitation cores and cirrus layers whereas TRMM can reveal details of convective cores, heavier precipitation and rain rates. A special product for TRMM-CS overlap observations is being considered.

Additional variables on storms conditions and environment will be added to each overpass. For example, OHC, before and after observations of pressure, shear, winds for each storm will be expanded. This will help to the outline storm environment before and after the CS overpass and provides an opportunity to diagnose the conditions leading up to and after each overpass. Profiles of strengthening vs. weakening storms can be analyzed using additional storm environment variables. Expanded best track data is also being considered. Other CS products including heating rates (2B-FLXHR), additional model overlay data (2B-ECMWF-AUX) and cloud optical depth (2B-TAU) are also being considered as database additions. Further refinements and enhancements to the CS TC database along with additional measurements by other satellite and model data will offer new qualitative and quantitative views of TC's.

BIBLIOGRAPHY

[Anthes, 1982] Anthes, R. A. (1982). *Tropical Cyclone - Their Evolution, Structure and Effects*, volume 19. American Meteorological Society.

[Arguez, 2007] Arguez, A. (2007). Supplement to state of the climate in 2006. *Bulletin of the American Meteorological Society*, 88(6):s1–s135.

[Arndt et al., 2010] Arndt, D. S., Baringer, M. O., and Johnson, M. R. (2010). State of the climate in 2009. *Bulletin of the American Meteorological Society*, 91(7):s1–s222.

[DeMaria, 1996] DeMaria, M. (1996). The effect of vertical shear on tropical cyclone intensity change. *Journal of the Atmospheric Sciences*, 53(14):2076–2088.

[DeMaria and Kaplan, 1999] DeMaria, M. and Kaplan, J. (1999). An updated statistical hurricane intensity prediction scheme (ships) for the atlantic and eastern north pacific basins. *Weather and Forecasting*, 14(3):326–337.

[Dommenget and Stammer, 2004] Dommenget, D. and Stammer, D. (2004). Assessing enso simulations and predictions using adjoint ocean state estimation. *Journal of Climate*, 17(22):4301–4315.

[Durden et al., 2009] Durden, S. L., Tanelli, S., and Dobrowalski, G. (2009). Cloudsat and a-train observations of tropical cyclones. *The Open Atmospheric Science Journal*, 3:80–92.

[Dvorak, 1975] Dvorak, V. (1975). Tropical cyclone intensity analysis and forecasting from satellite imagery. *Mon. Wea. Rev.*, 103:420–430.

[Dvorak, 1984] Dvorak, V. (1984). Tropical cyclone intensity analysis using satellite data. Technical Report NESDIS 11, NOAA Tech. Rep.

[Emanuel, 1986] Emanuel, K. A. (1986). An air-sea interaction theory for tropical cyclones. part i: Steady-state maintenance. *Journal of the Atmospheric Sciences*, 43(6):585–605.

[Fierro et al., 2009] Fierro, A. O., Simpson, J., LeMone, M. A., Straka, J. M., and Smull, B. F. (2009). On how hot towers fuel the hadley cell: An observational and modeling study of line-organized convection in the equatorial trough from toga coare. *Journal of the Atmospheric Sciences*, 66(9):2730–2746.

[Frank, 1977a] Frank, W. M. (1977a). Convective fluxes in tropical cyclones. *Journal of the Atmospheric Sciences*, 34(10):1554–1568.

[Frank, 1977b] Frank, W. M. (1977b). The structure and energetics of the tropical cyclone i. storm structure. *Monthly Weather Review*, 105(9):1119–1135.

[Frank, 1977c] Frank, W. M. (1977c). The structure and energetics of the tropical cyclone ii. dynamics and energetics. *Monthly Weather Review*, 105(9):1136–1150.

[Frank and Ritchie, 2001] Frank, W. M. and Ritchie, E. A. (2001). Effects of vertical wind shear on the intensity and structure of numerically simulated hurricanes. *Monthly Weather Review*, 129(9):2249–2269.

[Frank and Young, 2007] Frank, W. M. and Young, G. S. (2007). The interannual variability of tropical cyclones. *Monthly Weather Review*, 135(10):3587–3598.

[Gaiser et al., 2004] Gaiser, P., St Germain, K., Twarog, E., Poe, G., Purdy, W., Richardson, D., Grossman, W., Jones, W., Spencer, D., Golba, G., Cleveland, J., Choy, L., Bevilacqua, R., and Chang, P. (2004). The windsat spaceborne polarimetric microwave radiometer: sensor description and early orbit performance. *Geoscience and Remote Sensing, IEEE Transactions on*, 42(11):2347 – 2361.

[Galvin, 2008] Galvin, J. F. P. (2008). The weather and climate of the tropics: Part 7 - tropical revolving storms. *Weather*, 63(11):327–333.

[Goldenberg et al., 2001] Goldenberg, S. B., Landsea, C. W., Mestas-Nunez, A. M., and Gray, W. M. (2001). The recent increase in atlantic hurricane activity: Causes and implications. *Science*, 293(5529):474–479.

[Gray, 1968] Gray, W. M. (1968). A global view of the origin of tropical disturbances and storms. *Mon. Wea. Rev.*, 96:669–700.

[Gray, 1979] Gray, W. M. (1979). Tropical cyclone intensity determination through upper-tropospheric aircraft reconnaissance. *Bulletin of the American Meteorological Society*, 60(9):1069–1074.

[Hawkins et al., 2001] Hawkins, J. D., Lee, T. F., Turk, J., Sampson, C., Kent, J., and Richardson, K. (2001). Real-time internet distribution of satellite products for tropical cyclone reconnaissance. *Bulletin of the American Meteorological Society*, 82(4):567–578.

[Haynes et al., 2009] Haynes, J. M., L'Ecuyer, T. S., Stephens, G. L., Miller, S. D., Mitrescu, C., Wood, N. B., and Tanelli, S. (2009). Rainfall retrieval over the ocean with spaceborne w-band radar. *J. Geophys. Res.*, 114(D8):D00A22–.

[Haynes and Stephens, 2007] Haynes, J. M. and Stephens, G. L. (2007). Tropical oceanic cloudiness and the incidence of precipitation: Early results from cloudsat. *Geophys. Res. Lett.*, 34(9):L09811–.

[Hoffman and Leidner, 2005] Hoffman, R. N. and Leidner, S. M. (2005). An introduction to the near-real-time quikscat data. *Weather and Forecasting*, 20(4):476–493.

[Kawanishi et al., 2003] Kawanishi, T., Sezai, T., Ito, Y., Imaoka, K., Takeshima, T., Ishido, Y., Shibata, A., Miura, M., Inahata, H., and Spencer, R. (2003). The advanced microwave scanning radiometer for the earth observing system (amsr-e), nasda's contribution to the eos for global energy and water cycle studies. *Geoscience and Remote Sensing, IEEE Transactions on*, 41(2):184 – 194.

[Kidder et al., 1978] Kidder, S., Gray, W., and Haar, T. V. (1978). Estimating tropical cyclone central pressure and outer winds from satellite microwave data. *Mon. Wea. Rev.*, 106:1458–1464.

[Kidder et al., 2000] Kidder, S. Q., Goldberg, M. D., Zehr, R. M., DeMaria, M., Purdom, J. F. W., Velden, C. S., Grody, N. C., and Kusselson, S. J. (2000). Satellite analysis of tropical cyclones using the advanced microwave sounding unit (amsu). *Bulletin of the American Meteorological Society*, 81(6):1241–1259.

[Kim et al., 2009] Kim, H.-M., Webster, P. J., and Curry, J. A. (2009). Impact of shifting patterns of pacific ocean warming on north atlantic tropical cyclones. *Science*, 325(5936):77–80.

[Klaus, 2010] Klaus, W. (2010). Multivariate enso index. http://www.esrl.noaa.gov/psd/people/klaus.wolter/MEI/index.html, retrieved June 3, 2010.

[Knaff et al., 2004] Knaff, J. A., Seseske, S. A., DeMaria, M., and Demuth, J. L. (2004). On the influences of vertical wind shear on symmetric tropical cyclone structure derived from amsu. *Monthly Weather Review*, 132(10):2503–2510.

[Knaff and Zehr, 2007] Knaff, J. A. and Zehr, R. M. (2007). Reexamination of tropical cyclone wind-pressure relationships. *Weather and Forecasting*, 22(1):71–88.

[Kossin and Velden, 2004] Kossin, J. P. and Velden, C. S. (2004). A pronounced bias in tropical cyclone minimum sea level pressure estimation based on the dvorak technique. *Monthly Weather Review*, 132(1):165–173.

[Levinson and Lawrimore, 2008] Levinson, D. H. and Lawrimore, J. H. (2008). State of the climate in 2007. *Bulletin of the American Meteorological Society*, 89(7):S1–S179.

[Luo et al., 2008] Luo, Z., Stephens, G., Emanuel, K., Vane, D., Tourville, N., and Haynes, J. (2008). On the use of cloudsat and modis data for estimating hurricane intensity. *Geoscience and Remote Sensing Letters, IEEE DOI - 10.1109/LGRS.2007.905341*, 5(1):13–16.

[Marchand et al., 2008] Marchand, R., Mace, G. G., Ackerman, T., and Stephens, G. (2008). Hydrometeor detection using cloudsat - an earth-orbiting 94-ghz cloud radar. *Journal of Atmospheric and Oceanic Technology*, 25(4):519–533.

[Matrosov et al., 2008] Matrosov, S. Y., Battaglia, A., and Rodriguez, P. (2008). Effects of multiple scattering on attenuation-based retrievals of stratiform rainfall from cloudsat. *Journal of Atmospheric and Oceanic Technology*, 25(12):2199–2208.

[Merrill, 1984] Merrill, R. T. (1984). A comparison of large and small tropical cyclones. *Mon. Wea. Rev.*, 112:1408–1418.

[Miller et al., 1990] Miller, R. J., Schrader, A. J., Sampson, C. R., and Tsui, T. L. (1990). The automated tropical cyclone forecasting system (atcf). *Weather and Forecasting*, 5(4):653–660.

[Mitrescu et al., 2008] Mitrescu, C., Miller, S., Hawkins, J., LEcuyer, T., Turk, J., Partain, P., and Stephens, G. (2008). Near-real-time applications of cloudsat data. *Journal of Applied Meteorology and Climatology*, 47(7):1982–1994.

[Montgomery et al., 2006] Montgomery, M. T., Nicholls, M. E., Cram, T. A., and Saunders, A. B. (2006). A vortical hot tower route to tropical cyclogenesis. *Journal of the Atmospheric Sciences*, 63(1):355–386.

[Padgett, 2006a] Padgett, G. (2006a). Monthly global tropial cyclone summary, september 2006. http://www.australiasevereweather.com/cyclones/2007/summ0609.htm, retrieved May 20, 2009.

[Padgett, 2006b] Padgett, G. (2006b). Monthly global tropical cyclone summary, july 2006. http://www.australiasevereweather.com/cyclones/2007/summ0607.htm, retrieved May 20, 2009.

[Padgett, 2007] Padgett, G. (2007). Monthly global tropical cyclone summary, january 2007. http://www.australiasevereweather.com/cyclones/2007/summ0701.htm, retrieved May 15, 2009.

[Parkinson et al., 2006] Parkinson, C. L., Ward, A., and King, M. (2006). *Earth Science Reference Handbook*.

[Peterson and Baringer, 2009] Peterson, T. C. and Baringer, M. O. (2009). State of the climate in 2008. *Bulletin of the American Meteorological Society*, 90(8):S1–S196.

[Protat et al., 2009] Protat, A., Bouniol, D., Delano, J., OConnor, E., May, P. T., Plana-Fattori, A., Hasson, A., Grsdorf, U., and Heymsfield, A. J. (2009). Assessment of cloudsat reflectivity measurements and ice cloud properties using ground-based and airborne cloud radar observations. *Journal of Atmospheric and Oceanic Technology*, 26(9):1717–1741.

[Qu et al., 2006] Qu, J., Gao, W., Kafatos, M., Murphy, R., and Salomonson, V. (2006). *Earth Science Satellite Remote Sensing Vol.1: Science and Instruments*. Springer ; Tsinghua University Press, Berlin; New York; Beijing, China.

[Rappaport et al., 2009] Rappaport, E. N., Franklin, J. L., Avila, L. A., Baig, S. R., Beven, J. L., Blake, E. S., Burr, C. A., Jiing, J.-G., Juckins, C. A., Knabb, R. D., Landsea, C. W., Mainelli, M., Mayfield, M., McAdie, C. J., Pasch, R. J., Sisko, C., Stewart, S. R., and Tribble, A. N. (2009). Advances and challenges at the national hurricane center. *Weather and Forecasting*, 24(2):395–419.

[Reynolds et al., 2004] Reynolds, R. W., Gentemann, C. L., and Wentz, F. (2004). Impact of trmm ssts on a climate-scale sst analysis. *Journal of Climate*, 17(15):2938–2952.

[Reynolds and Smith, 1995] Reynolds, R. W. and Smith, T. M. (1995). A high-resolution global sea surface temperature climatology. *Journal of Climate*, 8(6):1571–1583.

[Rodgers and Adler, 1981] Rodgers, E. B. and Adler, R. F. (1981). Tropical cyclone rainfall characteristics as determined from a satellite passive microwave radiometer. *Monthly Weather Review*, 109(3):506–521.

[Shea and Gray, 1973] Shea, D. and Gray, W. (1973). The hurricane's inner core region i. symmetric and asymmetric structure. *J. Atmos. Sci.*, 30:1544–1564.

[Stephens et al., 2002] Stephens, G. L., Vane, D. G., Boain, R. J., Mace, G. G., Sassen, K., Wang, Z., Illingworth, A. J., O'Connor, E. J., Rossow, W. B., Durden, S. L., Miller, S. D., Austin, R. T., Benedetti, A., Mitrescu, C., and CloudSat Science Team, T. (2002). The cloudsat mission and the a-train. *Bulletin of the American Meteorological Society*, 83(12):1771–1790.

[Stephens et al., 2008] Stephens, G. L., Vane, D. G., Tanelli, S., Im, E., Durden, S., Rokey, M., Reinke, D., Partain, P., Mace, G. G., Austin, R., L'Ecuyer, T., Haynes, J., Lebsock, M., Suzuki, K., Waliser, D., Wu, D., Kay, J., Gettelman, A., Wang, Z., and Marchand, R. (2008). Cloudsat mission: Performance and early science after the first year of operation. *J. Geophys. Res.*, 113(D8):D00A18–.

[Stephens and Wood, 2007] Stephens, G. L. and Wood, N. B. (2007). Properties of tropical convection observed by millimeter-wave radar systems. *Monthly Weather Review*, 135(3):821–842.

[Velden and Smith, 1983] Velden, C. and Smith, W. (1983). Monitoring tropical cyclone evolution with noaa satellite microwave observations. *J. Appl. Meteor.*, 22:714–724.

[Webster et al., 2005] Webster, P. J., Holland, G. J., Curry, J. A., and Chang, H.-R. (2005). Changes in tropical cyclone number, duration, and intensity in a warming environment. *Science*, 309(5742):1844–1846.

Appendix I

.1 List of Abbreviations

AC	altocumulus
AEJ	african easterly jet
AMSR-E	Advanced Microwave Scanning Radiometer for EOS
AMO	Atlantic Multidecadel Oscillation
AMSU	Advanced Microwave Sounding Unit
AO	Arctic Oscillation
AS	altostratus
ATL	Atlantic
A-TRAIN	afternoon constellation
BT	brightness temperature
CIRA	Cooperative Institute for Research in the Atmosphere
CPAC	Central Pacific
CPR	cloud profiling radar
CS	CloudSat
CSU	Colorado State University
CTH	cloud top height
CTP	cloud top pressure
CTT	cloud top temperature
CU	cumulus
DMSP SSM/I	Defense Meteorological Satellite Program Special Sensor Microwave Imager
DPC	Data Processing Center
ECMWF	European Center for Medium range Weather Forecasting
ENSO	El-Nino Southern Oscillation
EOS	earth observing satellites
EPAC	East Pacific
ESSP	Earth System Science Pathfinder
ET	extratropical transition
HDF	hierarchical data format
HTC	hurricane/typhoon/cyclone
HUR	hurricane
JMA	Japan Meteorological Agency
JTWC	Joint Typhoon Warning Center
IR	infrared
IO	Indian Ocean
IWC	ice water content
IWP	ice water path
MM5	mesoscale model
MJO	Madden Julian Oscillation
MODIS	Moderate Resolution Imaging Spectroradiometer
N	north
NAO	North Atlantic Oscillation
NASA	National Aeronautics and Space Administration
NE	northeast

NHC	National Hurricane Center
NHRL	National Hurricane Research Laboratory
NOAA	National Oceanic and Atmospheric Administration
NOGAPS	Navy Operational Global Atmospheric Prediction System
NRL	Naval Research Laboratory
NS	nimbostratus
NW	northwest
NWP	numerical weather prediction
OHC	ocean heat content
PAC	Pacific
PDO	Pacific Decadel Oscillation
PIA	path-integrated attenuation
PR	precipitation radar
PV	potential vorticity
QBO	quasi-biennial oscillation
QuikSCAT	Quik Scatterometer
S	south
SC	stratocumulus
SE	southeast
SHEM	southern hemisphere
SHIPS	Statistical Hurricane Intensity Prediction Scheme
SIO	Southern Indian Ocean
SON	September October November
SSE	south south east
SSM/I	Special Sensor Microwave Imager
SST	sea surface temperature
ST	stratus
SW	southwest
TC	tropical cyclone
TD	tropical depression
TS	tropical storm
TMI	TRMM Microwave Imager
TRMM	Tropical Rainfall Measuring Mission
TV	television
TYP	typhoon
W	west
WPAC	West Pacific